T30d Theoretical Elementary Particle Physics
TUM School of Natural Sciences
Technical University of Munich

Dark Matter Capture in the Earth

Der Einfang von Dunkler Materie in der Erde

Alexander Hebel

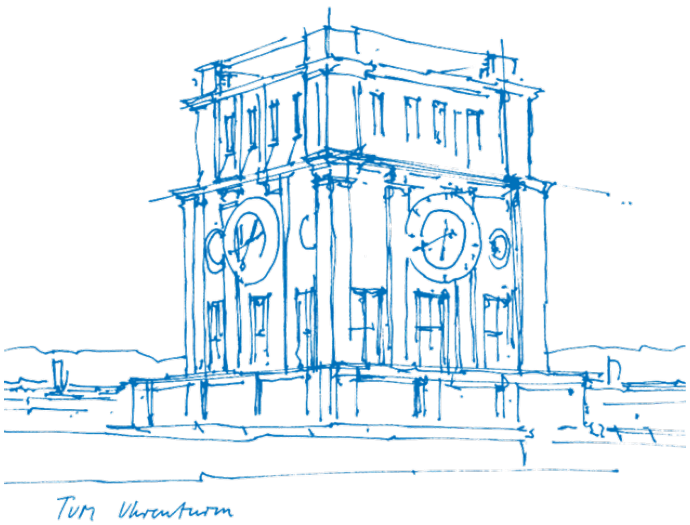

T30d Theoretical Elementary Particle Physics
TUM School of Natural Sciences
Technical University of Munich

Dark Matter Capture in the Earth

Der Einfang von Dunkler Materie in der Erde

Alexander Hebel

Thesis for the attainment of the academic degree

Master of Science (M.Sc.)

at the TUM School of Natural Sciences of the Technical University of Munich.

Supervisor:

Prof. Dr. Alejandro Ibarra

Submitted:

Munich, 16.01.2023

Abstract

In this work the non-observation of an exotic neutrino flux from the Earth's center by the IceCube neutrino observatory, induced by dark matter annihilations, is used to set rigorous model independent upper limits on the coupling strengths of the non-relativistic effective theory of dark matter-nucleon interactions and on the corresponding dark matter-nucleon cross sections for dark matter masses between 10 GeV and 10000 GeV, taking into account interference among operators. The upper limits on several coupling strengths are relaxed by about two orders of magnitude and the upper limits on the dark matter-nucleon cross sections by three to five orders of magnitude, when assuming interference. Hereby an equilibrium between dark matter capture and annihilation in the Earth is not assumed, which leads to upper limits, that are dependent on the chosen dark matter annihilation cross section. Compared to the commonly assumed thermal relic annihilation cross section the upper limits on the coupling strengths can be lowered for increasing annihilation cross sections at most by a factor of about 7 and the upper limits on the dark matter-nucleon cross section at most by a factor of about 44. The results of this work are compared to the results of three other experiments: XENON1T, PICO-60 and an IceCube search in the direction of the Sun. For the spin-independent dark matter-proton cross section and one corresponding coupling strength the upper limits are under interference for one point in parameter space at the same order of magnitude as the upper limits from the most constraining experiment, else they are always weaker. Using the residual internal heat flow of the Earth as a constraint on the heat flow, induced by dark matter annihilations, upper limits on the dark matter-nucleon cross sections can be set in an alternative way. These upper limits are however at least 5 orders of magnitudes weaker than the previous computed ones from IceCube data. As a consequence only a very small fraction of Earth's residual measured heat flow could be based on dark matter annihilations.

Acknowledgements

First of all I want to thank my supervisor Prof. Dr. Alejandro Ibarra for giving me the possibility to work on such a fascinating research topic in my master thesis, where he supported me with his advice and inspiring discussions. I also want to thank Anja Brenner for her time and her motivation to assist me in progressing with my thesis. In addition a special thanks goes to the whole working group for the nice integration and the pleasant working atmosphere. Finally I also want to thank my wife and my family for their support.

Contents

1 Introduction

Already in the early 19th century observations of rotation curves of galaxies [1] led to the conclusion, that there has to be an additional invisible component of matter, called dark matter (DM) [2], whose existence is underpinned by anisotropies in the cosmic microwave background (CMB) [3] [4], gravitational lensing effects [5] [6] and many other observations. Although some key facts about DM are known, like it interacts via gravitation, its lifetime has to be in cosmological timescales and its interactions via other forces is at most weak, the nature of DM remains unclear [7]. There exists a large amount of models, which include a DM candidate. One of the most promising candidates is the weakly interacting massive particle (WIMP) [8]. Its cross section with standard model (SM) particles is of the order of the weak cross section [9]. The cross section between DM and SM particles determines the relic DM abundance via the freeze-out time, which coincides for the WIMP with current measurements. These measurements indicate, that DM's portion of the total energy amount in the universe is roughly 27 %, whereas visible matter makes up about 5 % of it. The remaining 68 % consists of dark energy [4].

In general there are three methods to search for DM. The first one is called direct detection, where interactions of DM with SM particles take place directly in a detector located on the Earth. The recoil energy, which is hereby transferred to the detector material, can be measured, if it exceeds the energy threshold of the detector. The second one is called indirect detection. Here the interactions do not take place in a detector. Instead products of DM interactions, which take place somewhere else in the Universe, like DM annihilation into neutrinos or gamma rays, are measured in the detector. The third one are collider searches, where DM particles are directly produced during collisions in a collider.

Annihilation of DM is the main focus of many indirect DM searches. Ideal targets are regions with high density of DM, as signal strength for annihilation is proportional to density squared. This is also equivalent to a high J-factor, which is the energy spectrum integrated along the line of sight, taking only the term dependent on the distribution of the DM mass density. Typical targets with a high J-factor are the galactic center, dwarf spheroidal galaxies and galaxy clusters. But also closer objects like the Sun or the Earth are expected to have a high DM density. As signal strength is also proportional to the inverse square of the distance to the observed object, they are targets for indirect dark matter searches as well.

While the solar system passes through the galaxy, DM from the galactic halo becomes bound in the gravitational potential of it [10] [11] [12]. Through weak interactions with nuclei of the celestial bodies DM particles loose energy and are captured in the interior of that bodies via subsequent scatterings over time. Through DM self-annihilation a flux of neutrinos is generated, whose spectrum depends on the DM mass and the annihilation channel. DM particles accumulate in the celestial body until an equilibrium between DM capture and DM annihilation is reached. After that point in time the DM number density in the interior of that body remains constant. The specific nature of DM, its local density, the velocity distribution and the composition of the celestial body determine the capture rate of DM and the expected neutrino event rate [13]. DM annihilates also into a lot of other particles, which are all stopped in the matter of the celestial body and thus have an impact on its heat flow [14].

In DM searches an upper limit on the size of the signal, generated by DM, can be set by the non-observation of this signal [15]. Thus, in case of indirect DM searches, an upper limit on the size of the neutrino flux, generated by DM annihilations, can be set by the non-observation of a significant excess of neutrinos in comparison to the atmospheric neutrino background. This upper limit is translated into limits on the spin-independent and spin-dependent DM-nucleon cross section. Thereby the dark matter interaction with the nucleons is regularly set to be isoscalar, which means, that it is identical for protons and for neutrons. In this way interference between isoscalar and isovector contributions is neglected [16]. In the non-relativistic effective field theory the interaction does not only consist of the spin-independent and spin-dependent component, instead it contains several other interaction terms. Also these interactions can interfere with each other, which can lead, together with the interference between the isoscalar and isovector interactions, to more relaxed upper limits on the DM-nucleon cross section.

A method to determine rigorous upper limits on the coupling strengths of the effective theory of dark matter-nucleon interactions, including the effect of interference, has been introduced and applied to IceCube data from observations of the Sun [16]. This recently developed method will be used in this work to constrain the coupling strengths based on a first 327 days of detector livetime search for dark matter annihilations in the Earth's core conducted by IceCube [13]. In contrast to the Sun DM capture and annihilation are not assumed to be in equilibrium in the Earth, so that the upper limits on the coupling strengths are dependent on the assumed annihilation cross section, which will be a new focus of this thesis.

This work is organized as follows: In chapter 2 DM and the WIMP as a DM candidate will be motivated and an introduction to different DM detection methods is given. DM capture and annihilation in the Earth are explained in chapter 3. In chapter 4 the IceCube neutrino observatory is presented in detail, as the data of this work is acquired by this experiment. In chapter 5 the formalism to compute upper limits on the coupling strengths including operator interference is described. Results are presented in chapter 6, first for observations of the Earth on its own and second in comparison to other experiments. In chapter 7 constraints on the DM-nucleon cross sections from Earth's residual internal heat flow are set and compared to the previous obtained results. Conclusions and an outlook are given in chapter 8. Finally in the appendix the used Earth model, response functions and additional figures, not shown in the main text, are presented.

2 Dark matter

In this chapter information about the evidence of DM with a short historical review is given, the WIMP as a DM candidate is explained and different detection methods are presented.

2.1 Evidence for dark matter

In 1932 the Dutch astronomer Jan Oort studied the vertical stellar motion and number density of stars close to the galactic disk of the Milky Way for different distances [17]. From these measurements he determined a mass density of the disc nearby the Sun, which was by far larger than known values. So he concluded, that there has to be additional matter, which was not observed. This is one of the first hints towards DM. Approximately at the same time in 1933 the Swiss physicist and astronomer Fritz Zwicky observed the redshift of galaxy clusters [1]. Using the virial theorem to the Coma Cluster he determined the mass, based on the motion of the galaxies in it, and compared this result to the observable mass of the cluster [2]. The dynamic mass exceeded the luminous mass by a factor of about 400. Based on these results Zwicky obtained evidence of an unseen mass, whose associated mass is necessary to keep the cluster together, and called it "dunkle Materie", which introduced the term dark matter (DM). Although his calculations overestimated DM by more than one order of magnitude, mainly due to an old value of the Hubble constant, his conclusion, that the main part of matter consists of DM, holds until today and was confirmed by many others later on.

Galaxy rotation curves were optically analyzed with spectrographs in the 1960s and 1970s by Vera Rubin, Kent Ford and Ken Freeman [18] [19] with the result, that the mass contribution of DM in the Universe has to be around six times larger than the one of the observable mass. At the same time the radial distribution of interstellar atomic hydrogen was investigated by astronomers, who mapped the 21 cm line in nearby galaxies with radio telescopes, which extended the measurable rotations curves to further distances out from the center of the galaxies [20]. The luminous mass of these observations is mainly located in the center of the galaxy. For this reason the resultant stellar rotational velocity, far away from the center, should follow the relation $v_c \propto r^{-1/2}$, which can be derived by equating the gravitational and centripetal force for the observed mass. A typical rotation curve, based on measurements for the Andromeda galaxy M31, is shown in figure 2.1. Instead of the theoretically expected behaviour, the observed rotational velocity is almost constant in the outer regions of the galaxy, which means, that there has to be an additional unseen mass, which grows proportional to the radius of the galaxy. This can be explained by the presence of DM in the galaxies.

Further evidence for DM is given by the gravitational lensing effect, which itself is one of the consequences of general relativity. A heavy mass between an observer and a distant light source bends the light, as it travels through space. Light, which passes the massive object, the so called gravitational lens, the closest, is bent the most and vice versa. In addition it holds: the more massive the gravitational lens is, the more bending is observed. In strong lensing, e.g. at galaxy groups or clusters, the light source resembles partial arcs, scattered around the gravitational lens. From this distorted geometry the mass and distribution of the gravitational lens, and thus of the cluster or the galaxy group, can be determined. This has been done for many clusters with the result, that there is five times more DM than visible matter, which is also confirmed by radial velocity and X-rays measurements [5]. A very prominent example for the usage of gravitational lensing is the Bullet Cluster (1E-0657- 56), which provides further evidence for the existence of DM [6]. The Bullet Cluster consists of two colliding galaxy clusters. During the

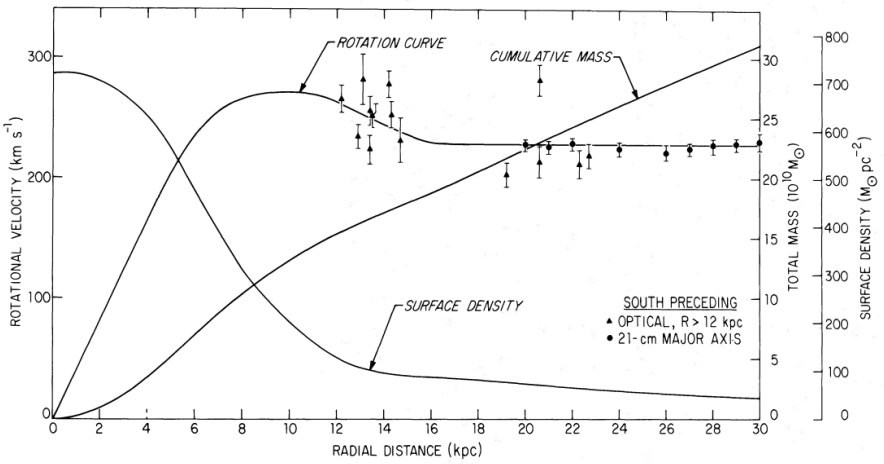

Figure 2.1 Rotation curve and geometry of the Andromeda galaxy M31, as shown in [20]. The observed rotational velocity far away from the center of the galaxy is almost constant. Therefor the mass has to grow linearly with the radius although it is mainly observed in the center of the galaxy.

merge stars, which are detectable in the visible spectrum, are not strongly affected by the collision, besides a remote slowdown due to gravitational interactions, and remain approximately at their original position in both galaxy clusters. Most of the baryonic matter is made up of hot gases of the intracluster medium (ICM), which can be detected by the emitted X-rays. As these gases interact electromagnetically, the ICM slows down much more than the stars during the merge and therefor lags behind the respective stars of the galaxy clusters. Using gravitational lensing, whereby distortion of objects in the background of the Bullet Cluster are examined, the location of the mass can be determined with the result, that the main part of the mass is only remotely decelerated and travels further during the merge than the ICM, which consists of the majority of the baryonic matter. So there has to be an invisible mass, heavier than all the baryonic mass, that remains at the original position in their clusters in a same manner like the stars, leading to a separation of baryonic and invisible matter. This means that the bulk of matter is invisible in the clusters and interacts gravitationally or at most weakly, as it is not significantly decelerated, which can be explained by introducing DM. In figure 2.2 the Bullet Cluster is depicted with galaxies and stars in white and orange, ICM in pink and the bulk of mass in blue.

Another hint towards DM is found in the CMB. In the early Universe baryonic matter was ionized to a plasma and interacted via gravitation and with radiation [22]. Gravitation compressed baryonic matter and lead to overdensities, whereas the photon pressure forced baryonic matter apart. So these two counteracting forces generated oscillations, the so-called baryon acoustic oscillations (BAOs). DM only interacts gravitationally or at most weakly and thus, unaffected by the photon pressure, remained in the density accumulations. With the expansion of the universe the plasma became cooler and at a temperature of about 3000 K recombination of protons and electrons to neutral hydrogen took place, which does not scatter with radiation. Now the photons started to move freely and decoupled from the baryonic matter. These photons have been travelling since the last scattering through space and are now detectable as the CMB. The CMB is very close to a perfect blackbody at about 2.73 K, but contains very small temperature fluctuations due to the above described BAOs. In figure 2.3 these fluctuations are shown in the temperature angular power spectrum of the CMB, characterizing the BAOs as function of angular scale or multipole moment. The temperature angular power spectrum contains interesting physical information [23]. The peaks in the CMB power spectrum are the modes, caught at extrema of their oscillations. They have an almost equal spacing, but different heights. By the help of computer simulations these peaks can be predicted for different cosmological parameters. Matching simulations to measured values leads then to constraints on these cosmological parameters. The first peak is the mode, that compressed once before recombination. Its position depends sensitively on the spatial curvature of

Figure 2.2 Image of the Bullet Cluster showing the collision of two galaxy clusters. The image is a superposition of hot gas detected by Chandra in X-rays (pink), of galaxies from Magellan and the Hubble Space Telescope in the visible spectrum (white and orange) and from a matter distribution calculated from gravitational lensing (blue). The image is taken from [21].

the universe. Constraining this parameter leads to the result, that the universe has a flat or almost flat geometry. The second peak is the mode, that compressed and decompressed once, the third peak is the mode, that compressed, decompressed and then compressed again, and so on. Since the odd numbered peaks are the ones, where the plasma is compressed, they are enhanced by a higher amount of baryonic matter over the even peaks. This means the more baryons exist, the more the second peak is suppressed compared to the third peak. In addition more baryonic mass leads to slower oscillations and therefor to slightly higher multipoles. Matching again data to simulation the baryonic matter density can be determined.

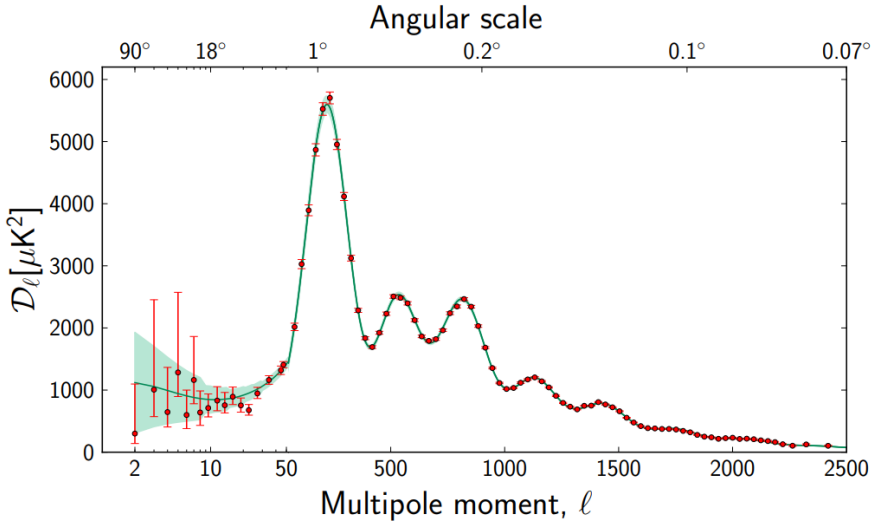

Figure 2.3 Temperature angular power spectrum of the CMB showing temperature fluctuations as function of angular scale or multipole moment. The red dots with error bars show Planck data. The green line shows a best fit by the standard model of cosmology, ΛCDM. The figure is taken from [3].

Higher acoustic peaks, i.e. the small scale modes, are sensitive to the ratio of dark matter to radiation and as the amount of radiation is known, they are directly sensitive to the dark matter density in the universe. In the earliest epochs the universe was radiation dominated, which leads due to changes in the gravitational potential to higher oscillations than in the matter dominated era. For this reason the higher acoustic peaks are raised. So there will be a transition in the height of the peaks, from which the dark matter density can be determined. As the third peak is boosted to a height comparable to the second peak, one can conclude, that the matter density in the plasma before recombination was dark matter dominated. In fact most of the matter has to be dark to be able to reconstruct the CMB power spectrum. Analysis of Planck data leads to the result, that there exists five times more DM than baryonic matter in the universe [4].

2.2 The weakly interacting massive particle (WIMP)

According to the standard ΛCDM model of cosmology, which is supported by the DM evidence, described in section 2.1, the energy density of the universe consists of 4.9 % ordinary matter and energy, 26.8 % DM and 68.3 % dark energy [4]. Although most of matter is thus dark, the nature of DM is still unknown. But the previously described evidence sets up some requirements on a possible DM candidate. These requirements are [7]:

- A DM candidate interacts via gravitation, all other interactions are at most in the range of the weak cross section.
- Its lifetime has to be at least the age of the universe, so that it is stable on cosmological timescales.
- The observed DM density of $\Omega_\chi h^2 \sim 0.1$ [8] can be reproduced.

They are fulfilled by the weakly interacting massive particle (WIMP), whose name already indicates, that it interacts, besides via gravitation, only weakly and which is stable on cosmological timescales. The so called freeze-out of DM plays an important role for the observed DM abundance [9]. In the very early and hot universe temperatures were so high ($T >> m_\chi$, with m_χ the DM mass), that DM was rapidly converting to lighter SM particles and vice versa, as all particles were in thermal equilibrium, which led to reactions like DM + DM ↔ SM + SM. When the universe cooled down to a temperature less than the mass of the DM particle, SM particles did not have enough energy any more to convert to DM and so the abundance of DM dropped exponentially due to the annihilation DM + DM → SM + SM. As the temperature drop of the universe is equivalent to its expansion, the annihilation rate $n_\chi < \sigma_A v >$ becomes smaller and smaller. Hereby n_χ is the number density of DM and $< \sigma_A v >$ the thermal average of the total cross section for annihilation of DM σ_A times the relative velocity v, called annihilation cross section. When $n_\chi < \sigma_A v >$ falls below the Hubble constant H, which is the expansion rate of the universe, DM ceases to annihilate, it freezes out and a relic cosmological DM abundance remains. This time dependent behaviour of n_χ can be described by a Boltzmann equation [9]:

$$\frac{\mathrm{d}n_\chi}{\mathrm{d}t} + 3Hn_\chi = - < \sigma_A v > \left[(n_\chi)^2 - (n_\chi^{\mathrm{eq}})^2\right] , \tag{2.1}$$

where n_χ^{eq} is the thermal equilibrium number density of DM. Applying an analytic approximation to equation 2.1 leads to the result, that the relic DM density is given by:

$$\Omega_\chi h^2 = \frac{m_\chi n_\chi}{\rho_c} \propto \frac{10^{-27}\ \mathrm{cm^3 s^{-1}}}{< \sigma_A v >} , \tag{2.2}$$

where h is the Hubble constant in units of 100 $\frac{\mathrm{km}}{\mathrm{s\ Mpc}}$ and ρ_c the critical density today. Figure 2.4 shows numerical solutions to the Boltzmann equation 2.1, which determines the relic DM abundance. The equilibrium abundance per comoving volume is plotted as solid line and the relic abundances per comoving volume as dashed lines, for different annihilation cross sections, as a function of the dimensional

parameter $x = m/T$, which increases with time. The larger the annihilation cross section, the longer the DM particles remain in thermal equilibrium and the smaller their relic abundance. If one assumes now a particle with weak interactions, like the WIMP, its annihilation cross section $< \sigma_A v >$ will be of order 10^{-26} cm^{3}s^{-1}, leading to a relic DM density in range of the observed one $\Omega_\chi h^2 \sim 0.1$ according to equation 2.2. This coincidence, that a particle with at most weak interactions reproduces the observed DM density, is called the "WIMP-miracle".

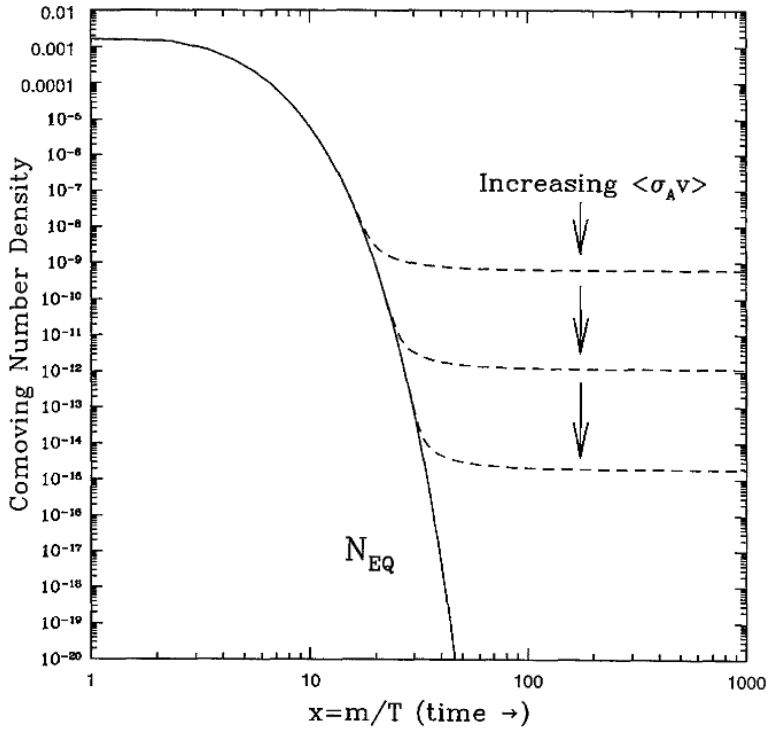

Figure 2.4 Comoving number density of WIMPs in the early Universe, as shown in [8]. The solid curve is the equilibrium abundance and the dashed curves are the relic abundances per comoving volume after freeze-out for different annihilation cross sections of the WIMP.

Depending on their freeze-out time or rather freeze-out temperature one distinguishes between cold, hot and warm DM [24]. If DM particles freeze out at temperatures higher than their own mass, their velocity will be relativistic and they are called hot DM. An example for such a DM candidate is the neutrino. Cold DM freezes out at temperatures below their mass leading to non-relativistic particles like the WIMP. Thus a cold DM particle is heavier than a hot DM particle. Warm DM is, concerning its properties, between hot and cold DM with sterile neutrinos and gravitinos as examples. Simulations about the large-scale structure of the universe favor cold DM [25]. At early times the universe was in a smooth initial state as seen in the CMB. Structure formed hierarchically in a bottom-up scenario, where small objects collapsed and merged in a continuous hierarchy to larger and more massive objects. This leads to the nowadays observed distribution of galaxies and their clusters, which are reproduced in simulations with cold DM. Hot DM instead would form structure in a top-down scenario, where superclusters would form first and fragment into smaller objects, which does not result in the large-scale structure observed today.

Taking all requirements, simulations and observations into account, the WIMP as a massive particle at non-relativistic speeds with weak interactions turns out to be an appropriate DM candidate. Thus the class of dark matter models, described by the WIMP, is well motivated and many experiments and also this work focus on it.

2.3 Dark matter detection

Although there exists evidence for DM, its nature is still a puzzle to be solved. As essential properties, like its mass and its cross section with SM particles, are unknown, many experiments are set up to determine these properties. These experiments can be subdivided in three categories. The first method is called direct detection. While the Solar System travels through space, it passes through the ambient DM of the universe, which leads to a flow of DM through Earth and all build-up experiments. The DM particles interact directly with nuclei of the detector, where a small recoil energy is transferred to the detector nuclei. This induces a detectable signal in form of scintillation light, ionization charges or heat, if the energy is above the detector threshold including the background noise, which is induced by other environmental SM particles [26]. To keep the background small, most of the experiments are operated underground, where interference from cosmic rays is minimized. Examples for direct detection experiments are PICO-60 [27] [28], XENON1T [29], Lux [30], PandaX-II [31] and CRESST II [32].

The second category is indirect detection, where the products of DM interactions, which do not take place in the detector, are measured. Annihilation of DM into gamma rays and neutrinos is the focus of most indirect DM searches, but also annihilation into other SM particles can be measured or a decay of DM, if DM particles are unstable. These interactions can happen somewhere in outer space, especially in regions of high DM density like galaxy clusters, dwarf spheroidal galaxies or the center of our galaxy, which makes them a common target for indirect DM detection experiments. But also very close objects like the Sun or the Earth have a high DM density and are good targets for indirect DM searches, as signal strength is proportional to the inverse square of the distance to the observed object and to the squared DM density. The amount of accumulated DM in the Sun, the Earth and other comparable objects depends on the DM capture and annihilation in these celestial bodies. While the Solar System travels through the galaxy, DM becomes bound in its gravitational potential and looses energy through weak interactions with nuclei of the celestial bodies. Via subsequent scatterings DM particles are then captured in the interior of the Sun and the planets, where they thermalise and annihilate. This leads to an accumulation of DM until an equilibrium between DM capture and annihilation is achieved. Almost all particles, into which DM annihilates, are stopped in the celestial body, but neutrinos, whose spectrum depends on the DM mass and the annihilation channel, can escape and their flux can be measured. The specific nature of DM, its local density, the velocity distribution and the composition of the celestial body determine the capture rate of DM and the expected neutrino event rate. Experiments looking for DM with indirect searches are ANTARES [33], Super-Kamiokande [34], Baikal NT200 [35] and IceCube [13] [36] [37], which will be described in detail in chapter 4.

The third approach is the search for DM with colliders, where DM particles are directly produced during collisions in the experiment. As DM only interacts with SM particles on the weak scale, it may be detected indirectly as missing energy and momentum, when other SM collision products are detected. Experiments are the Large Hadron Collider [38] and the former Large Electron-Positron Collider [39]. The aim of all DM searches is to detect DM and to determine its properties or, in case of a non-observation, to set constraints on them. This work focuses on indirect detection of DM in the Earth. For that reason DM capture and annihilation in the Earth are particularly relevant, in order to be able to set constraints on DM properties, and will be explained in the next chapter.

3 Dark matter capture and annihilation in the Earth

In this chapter the process of DM capture and annihilation in the Earth is presented and the interactions of DM with nuclei are explained, by reviewing the non-relativistic effective theory of DM-nucleon interactions.

3.1 Dark matter, the Solar System and the Earth

In the Solar System the gravitational field is mainly determined by the Sun, which also influences DM capture in the Earth. If the Earth is assumed to be in free space for simplicity of calculations, corrections on the DM capture, compared to the Earth as part of the Solar System, have to be considered. The influence on DM capture in the Earth by the Sun's gravitational field [40], by DM diffusion in the Solar System [41], by solar depletion [42] and by DM weak scattering in the Sun [43] has been thoroughly studied. The relative error on the capture rate for a free space Earth is at most 35 % for specific DM masses. For DM masses, close to masses of chemical elements of the Earth, the relative error is almost zero. [43]. For that reason the Earth is considered to be in free space in this work and the prior described effects of the Sun and the Solar System on the DM capture in the Earth are neglected. For the calculations a model of the Earth has to be used. In this work the preliminary reference Earth model (PREM) [44] is chosen, which is briefly described, together with the chemical element abundances, in appendix A.

The concept of DM capture and annihilation for the Earth, assumed to be in free space, is the following: As the Earth passes through the galaxy, it is constantly pervaded by ambient DM particles of the DM halo. Most of these DM particles simply transverse the Earth, but a few scatter off the nuclei in the Earth, whereby some of them loose so much energy, that their speed gets smaller than the escape velocity at the position of the scattering. Consequently these scattered DM particles become gravitationally bound to the Earth. Subsequent scatterings let the particles loose more energy and finally sink to the Earth's core [12]. The number of DM particles in the Earth is not only determined by this capture process, but also by annihilation and evaporation, which both decrease the number of DM particles in the Earth. The DM particles, captured in the center of the Earth, thermalise, except for very small DM-nucleon cross sections [45]. Below a minimum DM mass scatterings of the thermalised DM particles off ambient nuclei boost the DM particles to speeds above the escape velocity of the Earth, so that they are kicked out of the Earth, they evaporate. Therefor only DM particles with masses above this evaporation mass remain trapped in the Earth, annihilate and have an impact on a potential signal received by a neutrino detector. For the Earth the evaporation mass is determined to be about 12 GeV [11], which has been confirmed in a recent study [45].

The time-dependent number of DM particles in the Earth $N(t)$ follows the differential equation:

$$\frac{\mathrm{d}N}{\mathrm{d}t} = C - C_E N - C_A N^2 \,. \tag{3.1}$$

Here C is the capture rate, C_E the evaporation rate and C_A the annihilation coefficient, which is the probability of DM pair annihilation per time. In this work the focus is on DM masses above the evaporation mass or at most at the edge of it, so that evaporation can be neglected. Thus the term $C_E N$ drops out of the differential equation 3.1, which can then be solved by:

$$N(t) = \sqrt{\frac{C}{C_A}} \tanh\left(\frac{t}{\tau}\right) \tag{3.2}$$

$$\text{with} \qquad \tau = (CC_A)^{-\frac{1}{2}} \ . \tag{3.3}$$

τ is the equilibrium time of the capture and annihilation rate in the Earth. Equations, that govern the annihilation, scattering and capture of DM in the Earth, are described in the following sections.

3.2 Dark matter annihilation in the Earth

The total annihilation rate at the present time is given by:

$$\Gamma_A = \frac{1}{2} C_A N(t_\oplus)^2 = \frac{1}{2} C \tanh^2 \left(\frac{t_\oplus}{\tau} \right) , \tag{3.4}$$

with the age of the Earth $t_\oplus = 4.54 \cdot 10^9$ yr [46]. The second part of the equation is obtained by inserting the expression for $N(t)$ from equation 3.2 into it. As a consequence of DM annihilation inside the Earth a flux of neutrinos is produced, whose differential flux reads:

$$\frac{\mathrm{d}\Phi_\nu}{\mathrm{d}E_\nu} = \frac{\Gamma_A}{4\pi d^2} \sum_f \mathrm{BR}_f \frac{\mathrm{d}N_\nu^f}{\mathrm{d}E_\nu} \ . \tag{3.5}$$

In this equation f runs over the different final states of DM annihilations, the so-called annihilation channels, $\mathrm{d}N_\nu^f / \mathrm{d}E_\nu$ is the energy spectrum of neutrinos, produced in the annihilation channel f with branching ratio BR_f and d is the distance between the neutrino source and the detector, which equals the radius of the Earth $R_\oplus$. The annihilation constant C_A depends on the annihilation cross section $< \sigma_A v >$ and the thermal DM distribution in the Earth $\epsilon(r)$ [47]. By writing the total annihilation rate as [12]:

$$\Gamma_A = \frac{1}{2} \int_0^{R_\oplus} 4\pi r^2 \epsilon(r)^2 < \sigma_A v > \mathrm{d}r \, , \tag{3.6}$$

inserting this relation into equation 3.4 and solving for C_A, one receives:

$$C_A = < \sigma_A v > \frac{V_2}{V_1^2} \tag{3.7}$$

$$\text{with} \qquad V_j = 4\pi \int_0^{R_\oplus} r^2 \frac{\epsilon(r)^j}{\epsilon_0^j} \mathrm{d}r \ . \tag{3.8}$$

Here ϵ_0 is the thermal DM distribution in the center of the Earth and V_j are the effective volumes for the Earth. The expression for V_j can be simplified for a radial thermal DM distribution of

$$\epsilon(r) = \epsilon_0 \mathrm{e}^{-\frac{m_\chi \Phi(r)}{T_c}} \ , \tag{3.9}$$

with $\Phi(r)$ the total gravitational potential of the Earth at r and $T_c \approx 5 \cdot 10^3$ K the temperature of the Earth in the core, to [9] [11]:

$$V_j \approx 2.0 \cdot 10^{25} \left(\frac{j m_\chi}{10\mathrm{GeV}} \right)^{-\frac{3}{2}} \mathrm{cm}^3 \ . \tag{3.10}$$

With this expression for V_j the annihilation coefficient C_A can be approximated to:

$$C_A \approx 5.30 \cdot 10^{-49} \left(\frac{< \sigma_A v >}{3 * 10^{-26} \mathrm{cm}^3 \mathrm{s}^{-1}} \right) \left(\frac{m_\chi}{\mathrm{TeV}} \right)^{\frac{3}{2}} \mathrm{s}^{-1} \ . \tag{3.11}$$

3.3 Scattering of dark matter particles in the Earth

As DM particles are expected to move non-relativistically and the momentum transfer in the DM-nucleus scattering to be small compared to the target mass, the Galilean invariant non-relativistic effective theory of DM-nucleon interactions is applicable and chosen in this work [48] [49]. In this effective theory the Hamiltonian density of DM-nucleon interactions is expressed as a linear combination of quantum mechanical operators, that are Hermitian and Galilean invariant. These operators consist of four building units: the DM spin operator $\widehat{\mathbf{S}}_\chi$, the nucleon spin operator $\widehat{\mathbf{S}}_\mathcal{N}$, the momentum transfer operator $\widehat{\mathbf{q}}$ and the transverse relative velocity operator $\widehat{\mathbf{v}}^\perp = \widehat{\mathbf{w}} + \frac{\widehat{\mathbf{q}}}{2\mu_\mathcal{N}}$, where $\mu_\mathcal{N}$ is the DM-nucleon reduced mass and $\widehat{\mathbf{w}}$ the relative velocity operator. Keeping only terms, that are at most linear in $\widehat{\mathbf{v}}^\perp$, the non-relativistic effective theory of DM-nucleon interactions for DM particles up to spin 1/2 consists of 14 independent operators, that are listed in table 3.1. There exist additional operators for DM particles with a higher spin [50] [51], which are not part of this work, but could be included in the used methodology [16].

$\widehat{O}_1 = \mathbb{1}_\chi \mathbb{1}_\mathcal{N}$	$\widehat{O}_9 = i\widehat{\mathbf{S}}_\chi \cdot \left(\widehat{\mathbf{S}}_\mathcal{N} \times \frac{\widehat{\mathbf{q}}}{m_\mathcal{N}}\right)$
$\widehat{O}_3 = i\widehat{\mathbf{S}}_\mathcal{N} \cdot \left(\frac{\widehat{\mathbf{q}}}{m_\mathcal{N}} \times \widehat{\mathbf{v}}^\perp\right) \mathbb{1}_\chi$	$\widehat{O}_{10} = i\widehat{\mathbf{S}}_\mathcal{N} \cdot \frac{\widehat{\mathbf{q}}}{m_\mathcal{N}} \mathbb{1}_\chi$
$\widehat{O}_4 = \widehat{\mathbf{S}}_\chi \cdot \widehat{\mathbf{S}}_\mathcal{N}$	$\widehat{O}_{11} = i\widehat{\mathbf{S}}_\chi \cdot \frac{\widehat{\mathbf{q}}}{m_\mathcal{N}} \mathbb{1}_\mathcal{N}$
$\widehat{O}_5 = i\widehat{\mathbf{S}}_\chi \cdot \left(\frac{\widehat{\mathbf{q}}}{m_\mathcal{N}} \times \widehat{\mathbf{v}}^\perp\right) \mathbb{1}_\mathcal{N}$	$\widehat{O}_{12} = \widehat{\mathbf{S}}_\chi \cdot \left(\widehat{\mathbf{S}}_\mathcal{N} \times \widehat{\mathbf{v}}^\perp\right)$
$\widehat{O}_6 = \left(\widehat{\mathbf{S}}_\chi \cdot \frac{\widehat{\mathbf{q}}}{m_\mathcal{N}}\right) \left(\widehat{\mathbf{S}}_\mathcal{N} \cdot \frac{\widehat{\mathbf{q}}}{m_\mathcal{N}}\right)$	$\widehat{O}_{13} = i \left(\widehat{\mathbf{S}}_\chi \cdot \widehat{\mathbf{v}}^\perp\right) \left(\widehat{\mathbf{S}}_\mathcal{N} \cdot \frac{\widehat{\mathbf{q}}}{m_\mathcal{N}}\right)$
$\widehat{O}_7 = \widehat{\mathbf{S}}_\mathcal{N} \cdot \widehat{\mathbf{v}}^\perp \mathbb{1}_\chi$	$\widehat{O}_{14} = i \left(\widehat{\mathbf{S}}_\chi \cdot \frac{\widehat{\mathbf{q}}}{m_\mathcal{N}}\right) \left(\widehat{\mathbf{S}}_\mathcal{N} \cdot \widehat{\mathbf{v}}^\perp\right)$
$\widehat{O}_8 = \widehat{\mathbf{S}}_\chi \cdot \widehat{\mathbf{v}}^\perp \mathbb{1}_\mathcal{N}$	$\widehat{O}_{15} = -\left(\widehat{\mathbf{S}}_\chi \cdot \frac{\widehat{\mathbf{q}}}{m_\mathcal{N}}\right) \left[\left(\widehat{\mathbf{S}}_\mathcal{N} \times \widehat{\mathbf{v}}^\perp\right) \cdot \frac{\widehat{\mathbf{q}}}{m_\mathcal{N}}\right]$

Table 3.1 Operators of the non-relativistic effective theory of DM-nucleon interactions. The operator $\widehat{O}_2$ is omitted, as it is quadratic in $\widehat{\mathbf{v}}^\perp$ and therefor doesn't appear in leading order in any interaction.

Using the above introduced operators the Hamiltonian for a DM interaction with a target nucleus $\mathcal{T}$ reads:

$$\widehat{\mathcal{H}}_{\chi\mathcal{T}} = \sum_a \sum_i C_i^a \widehat{O}_i^a \,, \tag{3.12}$$

where i labels the possible interaction type, as seen in table 3.1, and a the nucleons in the target nucleus with a ranging from 1 up to A, the mass number of the nucleus. Thus the operator $\widehat{O}_i^a$ describes the interaction of type i between a DM particle and the a-th nucleon of the target nucleus. The coupling strength of the operator $\widehat{O}_i^a$ is given by C_i^a. It can be expressed as a 2 x 2 matrix, because the nucleon is an isospin doublet. With the identity $\mathbb{1}$ and the third Pauli Matrix τ_3^a in the a^{th} nucleon isospin space C_i^a, consisting of the isoscalar c_i^0 and isovector c_i^1 coupling strengths, is commonly expressed as:

$$C_i^a = c_i^0 \mathbb{1}_{2x2}^a + c_i^1 \tau_3^a \,. \tag{3.13}$$

The isoscalar and isovector coupling strengths are linearly related to the coupling strengths to the neutron and the proton:

$$\begin{aligned} c_i^\mathrm{n} &= \frac{1}{2}(c_i^0 - c_i^1) \\ c_i^\mathrm{p} &= \frac{1}{2}(c_i^0 + c_i^1) \,. \end{aligned} \tag{3.14}$$

With the coupling strengths to the neutron and the proton C_i^a reads:

$$C_i^a = c_i^{\mathrm{n}}(\mathbb{1}_{2x2}^a - \tau_3^a) + c_i^{\mathrm{p}}(\mathbb{1}_{2x2}^a + \tau_3^a) \,. \tag{3.15}$$

From the Hamiltonian density of equation 3.12 the differential cross section for DM-nucleon scattering can be calculated [49][52]:

$$\begin{aligned}\frac{\mathrm{d}\sigma_{\chi\mathcal{T}}(q^2, w^2)}{\mathrm{d}q^2} = \frac{1}{(2J+1)w^2} \sum_{\tau,\tau'} \Bigg[\sum_{k=M,\Sigma',\Sigma''} R_k^{\tau\tau'}\left(v_{\mathcal{T}}^{\perp 2}, \frac{q^2}{m_{\mathcal{N}}^2}\right) W_k^{\tau\tau'}(q^2) \\ + \frac{q^2}{m_{\mathcal{N}}^2} \sum_{k=\Phi'',\Phi''M,\Phi',\Delta,\Delta\Sigma'} R_k^{\tau\tau'}\left(v_{\mathcal{T}}^{\perp 2}, \frac{q^2}{m_{\mathcal{N}}^2}\right) W_k^{\tau\tau'}(q^2) \Bigg] \,.\end{aligned} \tag{3.16}$$

Here q is the momentum transfer, w is the DM-nucleus relative velocity, J is the target nucleus spin, $m_{\mathcal{N}}$ is the nucleon mass and $v_{\mathcal{T}}^{\perp 2} = w^2 - q^2/(4\mu_{\mathcal{T}}^2)$ the transverse velocity squared, with $\mu_{\mathcal{T}}$ the DM-nucleus reduced mass. The eight DM response functions $R_k^{\tau\tau'}$ are listed in appendix B according to [49] [53]. They depend on $q^2/m_{\mathcal{N}}^2$, on $v_{\mathcal{T}}^{\perp 2}$ and on the coupling strengths c_i^{τ}. The eight nuclear response functions $W_k^{\tau\tau'}$ are expressed in terms of reduced matrix elements of nuclear charges and currents and were computed numerically in [12] and [52]. They are listed as analytic expressions for all elements, used in this work, in appendix C.

3.4 Dark matter capture in the Earth

In order to get captured in the Earth, DM particles have to loose so much energy, that they slow down from their initial velocity, given as the DM - nucleus relative velocity w, to a velocity smaller than the local escape velocity $v(r)$ at the distance r from the center of the Earth. By kinematics the fractional DM energy loss in the DM-nucleus scattering $\Delta E/E$, with $E = m_\chi w^2/2$ is in the interval:

$$0 \leq \frac{\Delta E}{E} \leq 4\frac{\mu_{\mathcal{T}^2}}{m_\chi m_{\mathcal{T}}} \,. \tag{3.17}$$

In addition the scattering from velocity w to at least velocity $v(r)$ requires with $w = \sqrt{u^2 + v(r)^2}$ and u the DM velocity at infinity:

$$\frac{\Delta E}{E} \geq \frac{w^2 - v(r)^2}{w^2} = \frac{u^2}{w^2} \,. \tag{3.18}$$

Thus the rate of scattering from a velocity w to a velocity $v(r)$ becomes [11]:

$$\Omega_v^-(w) = \sum_{\mathcal{T}} \eta_{\mathcal{T}} w \Theta\left(4\frac{\mu_{\mathcal{T}^2}}{m_\chi m_{\mathcal{T}}} - \frac{u^2}{w^2}\right) \int_{\frac{u^2}{w^2}E}^{4\frac{\mu_{\mathcal{T}}^2}{m_\chi m_{\mathcal{T}}}E} \frac{\mathrm{d}\sigma_{\chi\mathcal{T}}(E_R, w^2)}{\mathrm{d}E_R} \mathrm{d}E_R \,. \tag{3.19}$$

The sum in this equation includes all elements of the Earth, listed in Appendix A, with radius dependent number density $\eta_{\mathcal{T}}(r)$ and mass $m_{\mathcal{T}}$. The integral is performed over all kinematically allowed recoil energies E_R, whereat the differential cross section $\mathrm{d}\sigma_{\chi\mathcal{T}}(E_R, w^2)/\mathrm{d}E_R$ is computed according to equation 3.16 with the identity $q^2 = 2m_{\mathcal{T}}E_R$.

The differential capture rate per volume is obtained by a velocity integral over the scattering rate from equation 3.19, where $f(u)$ is the DM speed distribution at infinity boosted in the Earth's restframe [11]:

$$\frac{\mathrm{d}C}{\mathrm{d}V} = \int_{u \leq u_{\max}^{\mathrm{Earth}}} \frac{f(u)}{u} w \Omega_v^-(w) \mathrm{d}u \,. \tag{3.20}$$

For the speed distribution a Maxwell-Boltzmann distribution, truncated at the escape velocity 544 km/s from the Milky Way [54] [55], and a local standard of rest velocity of 220 km/s [56] [57] are assumed. Assuming spherical symmetry the DM capture rate can finally be calculated by:

$$C = \int_0^{R_\oplus} 4\pi r^2 \frac{\mathrm{d}C}{\mathrm{d}V} \mathrm{d}r \ . \tag{3.21}$$

Inserting equations 3.20 and 3.19 into equation 3.21 the DM capture rate reads:

$$C = \sum_{\mathcal{T}} \int_0^{R_\oplus} 4\pi r^2 \eta_{\mathcal{T}}(r) \frac{\rho_{loc}}{m_\chi} \mathrm{d}r \int_{u \leq u_{\max}^{\mathrm{Earth}}} \frac{f(u)}{u} w^2 \mathrm{d}u \int_{\frac{m_\chi v^2}{2}}^{2\frac{\mu_{\mathcal{T}}^2 w^2}{m_{\mathcal{T}}}} \frac{\mathrm{d}\sigma_{\chi\mathcal{T}}(E_R, w^2)}{\mathrm{d}E_R} \mathrm{d}E_R \ . \tag{3.22}$$

For the local DM density a value of 0.3 GeV/cm^3 is assumed [58]. This equation is used together with equation 3.16 for the calculations of this work.

In the non-relativistic effective theory of DM-nucleon interactions the particle physics DM model is completely given by the DM mass and the set of the 28 coupling strengths from equation 3.13. They define the types and strengths of interactions arising from a concrete DM model upon matching to the non-relativistic effective theory. By collecting the coupling strengths c_i^0 and c_i^1 for $i = 1, 3, ..., 15$ in a single vector $\mathbf{c}$ with components c_α for $\alpha = 1, ..., 28$ the capture rate can be written as [59] [60]:

$$C(\mathbf{c}) = \mathbf{c}^T \mathbb{C} \mathbf{c} \ . \tag{3.23}$$

Here $\mathbb{C}$ is a real symmetric 28×28 matrix, whose content depends on the Earth model, the local DM density, the DM mass and the DM velocity distribution, but is independent of the underlying particle physics model for a given DM mass.

The annihilation of DM produces SM particles. Most of these particles are stopped in the Earth, but neutrinos can escape the center of the Earth and their flux can be measured. From this measurement the total annihilation rate can be determined and thus equation 3.4 can be evaluated together with equation 3.23. A large experimental setup to measure neutrinos is the IceCube neutrino observatory, which is described in the next chapter. The IceCube collaboration sets upper limits on the total annihilation rate for different DM masses by the non-observation of an exotic neutrino flux [13]. These upper limits are used in this work in order to set upper limits on DM properties, which is described in chapter 5.

4 The IceCube neutrino observatory

Indirect DM searches focus on DM annihilation products, that can be measured here on Earth. A very prominent example for these experiments is IceCube, a neutrino telescope, located in the ice of Antarctica at the geographic South Pole. In this work data is used, collected by IceCube in a first 327 days of detector livetime search for dark matter annihilations in the Earth [13]. For that reason an overview of the IceCube neutrino observatory is given in this chapter with a focus on the observation of an exotic neutrino flux from the center of the Earth.

4.1 The detector

The IceCube telescope is designed to detect Cherenkov radiation, in order to measure neutrinos. Interactions of neutrinos in the ice produce charged leptons, that travel through the detector. As these charged particles pass through the ice at a speed greater than the phase velocity of light in ice, Cherenkov radiation is produced [61]. The energy and direction of the charged leptons can be reconstructed by recording the number of Cherenkov photons and their arrival time. Consequently also the parent neutrinos direction and energy can be determined.

Installation of IceCube started in 2005 and full deployment was achieved in 2011 [62]. It has a size of one cubic kilometer and is installed between 1450 m and 2450 m depth in the ice of the Antarctic [63]. IceCube is instrumented with 5160 digital optical modules (DOMs) in 86 strings. The DOMs are the fundamental detector elements of IceCube. Each DOM consists of a photomultiplier tube (PMT) and an electronic board assembly, which enables the DOMs to digitize and time-stamp the received photonic signals and transmit them via the strings to the IceCube Lab at the surface [64]. 78 strings are ordered in a hexagonal grid with 125 m horizontal spacing between each string. On each string are 60 DOMs, which are vertically 17 m apart from each other, enabling IceCube to measure energies of neutrinos down to $E_\nu \sim 50\ \text{GeV} - 100\ \text{GeV}$ with an optimal response at $E_\nu \geq 1000\ \text{GeV}$ [62]. 8 strings in the center of IceCube are located horizontally closer together (42 m - 72 m) and are each equipped with 50 higher quantum efficiency DOMs, spaced 7 m vertically apart on the strings, which maximises the detection efficiency for low energy neutrinos in the 10 GeV - 100 GeV energy range. This subarray of IceCube at a depth of 2100 m to 2450 m, together with 7 central standard IceCube strings, is called DeepCore [65]. In a depth band between 2000 m and 2100 m exists a high dust concentration leading to an absorbing and scattering ice at that dust layer. This region is not instrumented with DeepCore DOMs. Instead 10 further DOMs are installed as an overhead veto above this dust layer to reduce background noise from the vertical direction, where the cosmic-ray angular distribution is at its maximum. In figure 4.1 the architecture of the IceCube observatory is shown.

4.2 Measurement of neutrinos

High-energy neutrinos interact with matter mainly via inelastic scattering off quarks in target nuclei with an exchange of a Z (neutral current) or W (charged current) boson [66]. Neutral current interactions leave the neutrino state intact, whereas in a charged current interaction a charged lepton, that shares the neutrino flavor, is produced. In this way muons can be produced in charged current interactions of muon neutrinos. The produced muons create Cherenkov emission in the ice, resulting in so-called tracks in the detector.

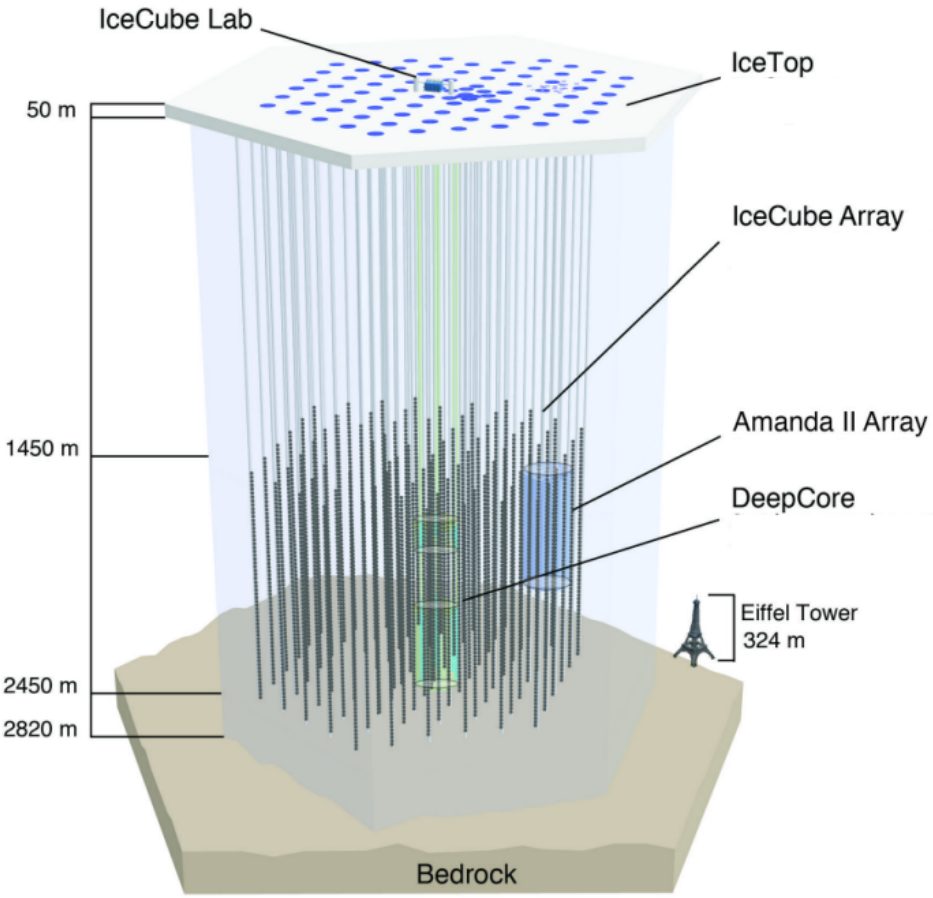

Figure 4.1 Setup of the IceCube observatory, taken from [66].

Hereby the interaction does not have to take place inside the detector as the tracks can be several kilometres long. In contrast energetic electrons and taus, which are produced in charged current interactions of electron neutrinos and tau neutrinos, will not create elongated tracks, as electrons scatter rapidly and taus have a very short lifetime. Most neutrino searches focus on upward going neutrinos passing through the whole Earth as a filter, because there is a large background due to atmospheric muons, produced by cosmic rays in the atmosphere, which can be further reduced by focusing on point-like sources.

When a neutrino scatters off a target nucleus, this struck target will not remain intact and its fragments will produce an hadronic particle shower, which also results in Cherenkov emission and is called cascade. This light pattern is mostly spherical because of the high number of subsequent secondary particles. Due to its shape the angular resolution of cascades is worse than for tracks, but the energy of the initiating neutrino can be estimated with a better resolution, as the cascade can be fully contained in the detector volume, whereas the muons loose energy gradually on their complete track in and outside the detector.

In general the energy of the secondary charged leptons can be estimated from the total number of Cherenkov photons. This energy can be related to the neutrino energy by accounting for kinematic effects and detection efficiency. The direction of the neutrinos is determined by using the timestamps of the DOMs. The signals from all DOMs are collected in the IceCube Lab at the surface and sorted by their known position and triggered timestamp into telltale patterns, that indicate the direction, energy and flavor of the neutrino.

Identification of neutrinos depends strongly on differentiation from background noise, as the background rate due to atmospheric cosmic-rays is around 3000 muons per second at a depth of 1450 m, where the detector of IceCube is located. Muon neutrinos, that interact outside the detector, produce the above described tracks in the detector. These tracks can be pointed back to their sources with an angular resolution smaller than 0.4 °. For these events the Earth is used as a filter to remove background noise. As a consequence only muon neutrinos out of one half of the sky can be measured.

In order to get rid of these limitations, there exists the possibility to only concentrate on high-energy starting events (HESEs), which are the above described cascades, induced by high-energy neutrinos, that interact exclusively inside the detector. By dividing the instrumented volume of ice in an outer veto shield and an inner zone, where the HESEs take place, this method can be implemented. In this way neutrinos of all flavours, out of every direction, independent of charged or neutral current interaction, can be measured. A big advantage of this method is, that the detector functions as a calorimeter absorbing the entire energy of the measured neutrinos with a 10 % – 15 % resolution [65]. In contrast the angular resolution deteriorates, compared to measured tracks, down to 10 ° to 15 °. An example for a HESE, which is completely contained in the detector volume, is shown in figure 4.2 on the left side. On the right side of figure 4.2 an upcoming muon track though the detector is depicted.

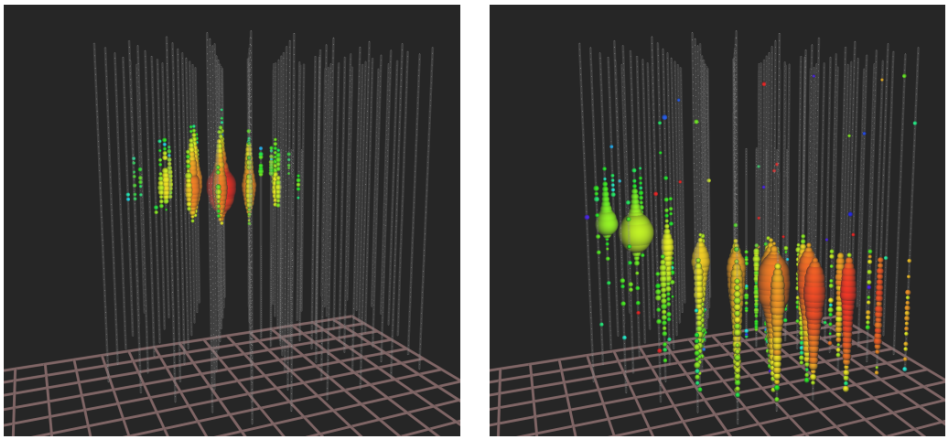

Figure 4.2 Signal patterns measured by IceCube. The color of the dots represents arrival time, starting with red as an early arrival over all rainbow colors to purple as a late arrival. The size of the dots reflects the number of detected photons. On the left side a cascade is depicted, initiated by an electron or tau neutrino, with a minimum energy of $E_\nu \approx 1$ PeV. On the right side an upgoing muon track with a deposited energy of $E_\nu \approx 2.6$ PeV is shown, taken from [66].

4.3 Detection results

IceCube is used for DM searches in dwarf spheroidal galaxies [67], in the galactic center [68], in the halo [69], in the Sun [36] and in the Earth [13]. By measurements of the neutrino flux from objects in the outer space constraints on the DM annihilation cross section as function of DM mass can be set. In this work the focus is on DM searches in the Earth, where limits on the DM-nucleon cross section can be derived. By the non-observation of a significant excess of neutrinos, compared to the background noise, an upper limit on the size of an exotic neutrino flux from the observed object can be set. Using the package WimpSim [70] this upper limit on the exotic flux can be converted into an upper limit on the total DM annihilation rate inside Earth Γ_A, which can be translated into constraints on the DM-nucleon cross section. For the Earth the constraints on the spin-independent DM-nucleon cross section, obtained by IceCube, are shown in figure 4.3, where they are compared with other experiments.

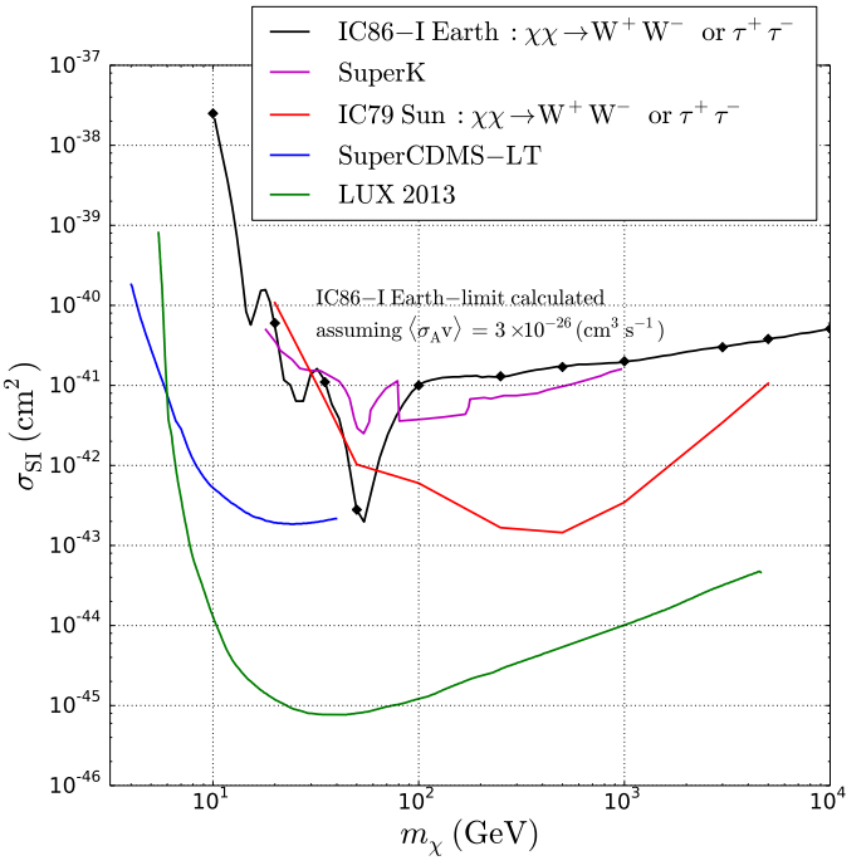

Figure 4.3 Limits on the spin-independent DM-nucleon cross section as function of DM mass, assuming a DM annihilation cross section of $< \sigma_A v >= 3 \cdot 10^{-26}\mathrm{cm}^3\mathrm{s}^{-1}$, are shown in black from IceCube data. Annihilation into W^+W^- is assumed for DM masses above the rest mass of the W boson and annihilation into $\tau^+\tau^-$ for lower DM masses. The result is compared to limits set by SuperCMDSlite [71], LUX [72], Super-Kamiokande [73] and to an IceCube search in the direction of the Sun [74]. The figure is taken from [13].

In order to convert the upper limits on the exotic neutrino flux into constraints on the DM-nucleon cross section, some assumptions have to be made. The total annihilation rate Γ_A is dependent on the DM mass and the annihilation channel. Thus the first assumption has to be made about the annihilation channel, where two hard channels and one soft channel is probed by IceCube for the Earth. In the hard channels DM is assumed to annihilate into W^+W^-, when the DM mass is above the rest mass of the W boson of 80.377 GeV and into $\tau^+\tau^-$ for DM masses below the rest mass of the W boson. Both the W bosons and τ leptons quickly decay and the energy of the produced neutrinos peaks close to the annihilating DM mass. As the neutrinos receive much energy a lot of them will be able to exceed the energy threshold of IceCube. The opposite is the case for the soft channel, where DM annihilates into $b\bar{b}$. The decay of b results in low neutrino energies, so that it is more unlikely, that the energy threshold of IceCube can be exceeded. For this reason limits are expected to be more stringent for the hard channels, which are assumed in figure 4.3. A detailed analysis about the different annihilation channels and their spectra are given in [75].

The annihilation cross section is set to the thermal relic value of $< \sigma_A v >= 3 \cdot 10^{-26}\mathrm{cm}^3\mathrm{s}^{-1}$, which is from here on denoted as $< \sigma_A v >_{\mathrm{th}}$. The annihilation cross section has to be set to a certain value, because the total DM annihilation rate and the DM-nucleon cross section are not directly linked in the Earth, as an equilibrium between DM capture and DM annihilation can not be assumed. Several experiments, including IceCube, set upper limits on the annihilation cross section $< \sigma_A v >$, whereby gamma-ray telescopes

lead to the most constraining limits. The results of a combined analysis of MAGIC and Fermi-LAT observations of dwarf spheroidal galaxies at the 95 % confidence level [76] are shown in figure 4.4. On the left side are the upper limits for a DM annihilation into $\tau^+\tau^-$, which are applicable for DM masses below the rest mass of the W boson according to the assumptions, and on the right side into W^+W^-, which are applicable above the rest mass of the W boson. As seen here for DM masses below 80 GeV the upper limits on $< \sigma_A v >$, for an annihilation into $\tau^+\tau^-$, are below the thermal relic annihilation cross section $< \sigma_A v >_{\text{th}}$. For a DM of 10 GeV the upper limit is about one order of magnitude smaller than $< \sigma_A v >_{\text{th}}$. For higher DM masses the upper limits on $< \sigma_A v >$, for an annihilation into W^+W^-, are equal to or larger than $< \sigma_A v >_{\text{th}}$. For a DM mass of 100 GeV the upper limit on $< \sigma_A v >$ equals approximately $< \sigma_A v >_{\text{th}}$, for a DM mass of 1000 GeV approximately $10 < \sigma_A v >_{\text{th}}$ and for a DM mass of 10000 GeV approximately $100 < \sigma_A v >_{\text{th}}$. The results of a combined dark matter search towards dwarf spheroidal galaxies with Fermi-LAT, HAWC, H.E.S.S., MAGIC, and VERITAS [77] are pending, which will eventually further lower the upper limits on $< \sigma_A v >$.

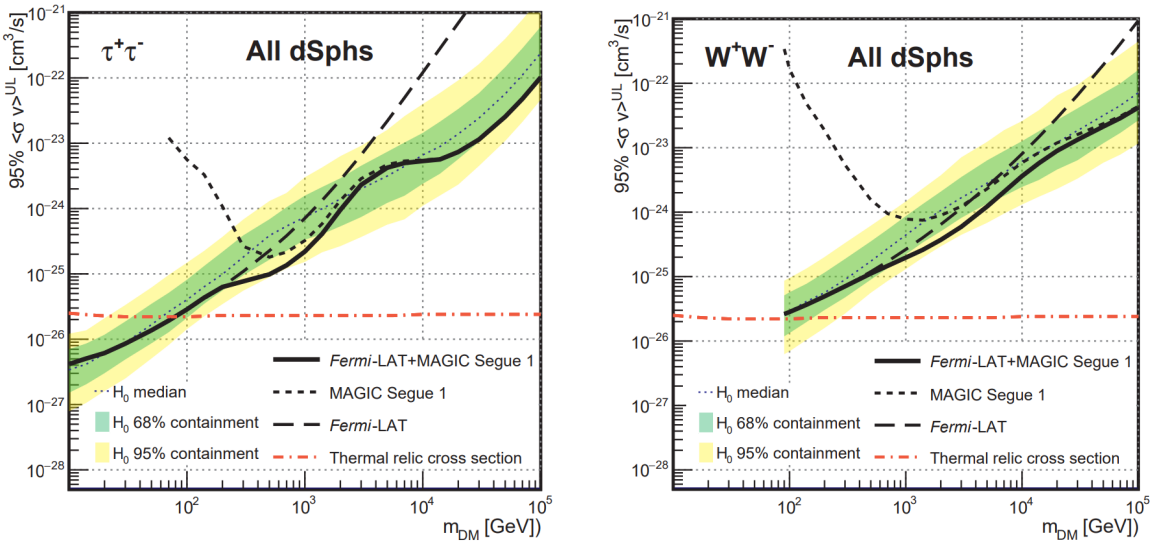

Figure 4.4 Upper limits on the DM annihilation cross section at the 95% confidence level from a combined analysis of MAGIC and Fermi-LAT observations of dwarf spheroidal galaxies (dSphs). Results for DM annihilation into $\tau^+\tau^-$ are shown on the left and into W^+W^- on the right. Thick solid lines show the limits, obtained by combining Fermi-LAT observations of 15 dwarf spheroidal galaxies with MAGIC observations of the dwarf spheroidal galaxy Segue 1. Dashed lines show the observed individual MAGIC (short dashes) and Fermi-LAT (long dashes) limits. The thin-dotted line, green and yellow bands show, respectively, the median and the symmetrical, two-sided 68 % and 95 % containment bands. The red-dashed-dotted line shows the thermal relic cross-section, taken from [77].

In figure 4.5 the upper limits on the spin-independent cross section as function of the annihilation cross section are shown for two DM masses. With increasing annihilation cross section $< \sigma_A v >$ the upper limit on the spin-independent DM-nucleon cross section decreases until it reaches a lower bound, where an equilibrium between DM capture and DM annihilation for the relevant mass is attained. For the results in figure 4.3 the thermal annihilation cross section is chosen, although it is excluded for a DM mass of 50 GeV by the above presented Fermi / MAGIC limits.

Further assumptions have to be made, e.g. about the local DM density, which is set to 0.3 GeV/cm^3 in accordance with current estimates of 0.2 GeV/cm^3 to 0.5 GeV/cm^3 [58]. For the velocity distribution of the DM particles in the halo a Gaussian distribution is assumed, which is based on the Standard Halo Model. According to galaxy formation simulations additional macro structural components, like a dark disc could exist, that effect the velocity distribution and increase it at low velocities [79]. This could raise the DM capture rate in the Earth, as mainly DM with low velocities can be captured in the Earth.

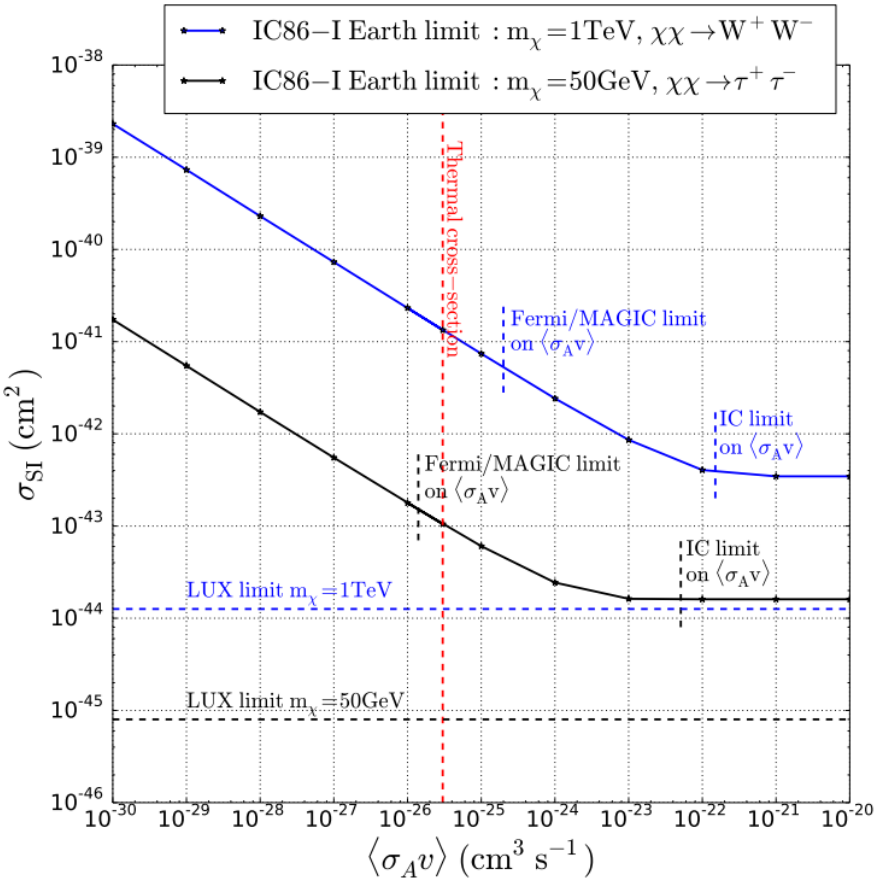

Figure 4.5 Upper limits on the spin-independent DM-nucleon cross section as function of DM annihilation cross section for 50 GeV DM annihilating into $\tau^+\tau^-$ (in black) and for 1 TeV DM annihilating into W^+W^- (in blue). Limits of Lux are shown as a comparison in dashed lines. The thermal relic annihilation cross section is shown as a vertical red dashed line. Upper limits on the annihilation cross-section are also indicated as vertical dashed lines from IceCube [78] and from a combined analysis of Fermi-LAT and MAGIC [76]. The figure is taken from [13].

Finally also the DM capture rate in the Earth has to be determined. It depends on the composition of the Earth, the DM mass, the velocity distribution, that is described above, and the local DM density. For the results, shown in figure 4.3, the DM capture rate is taken from [80] and is shown in figure 4.6. As seen in the figure the DM capture rate increases considerably for the most abundant elements in the Earth. The peaks of the DM capture rate influence directly the upper limits on the DM-nucleon cross section. For a DM mass of about 50 GeV, which refers to the resonant peak of ^{56}Fe, this leads to a lower upper limit on the spin-independent DM-nucleon cross section than the one, obtained from the IceCube DM search in the direction of the Sun.

Upper limits on the DM-nucleon cross-sections are also obtained from DM searches in the direction of the Sun. For the spin-dependent DM-nucleon cross section these upper limits are competitive with those, from direct detection experiments, in the DM mass region above 80 GeV [36], whereas they are weaker than those, obtained from direct detection experiments, for the spin-independent cross-section as seen in figure 4.3. Future analyses, combining several years of data, will improve the limits of several DM searches. The upper limits from the Sun have shortly been improved for low DM masses [81] and for the Earth a new analysis is already pending, which will lower the upper limits on the spin-independent DM-nucleon cross section by about one order of magnitude [82].

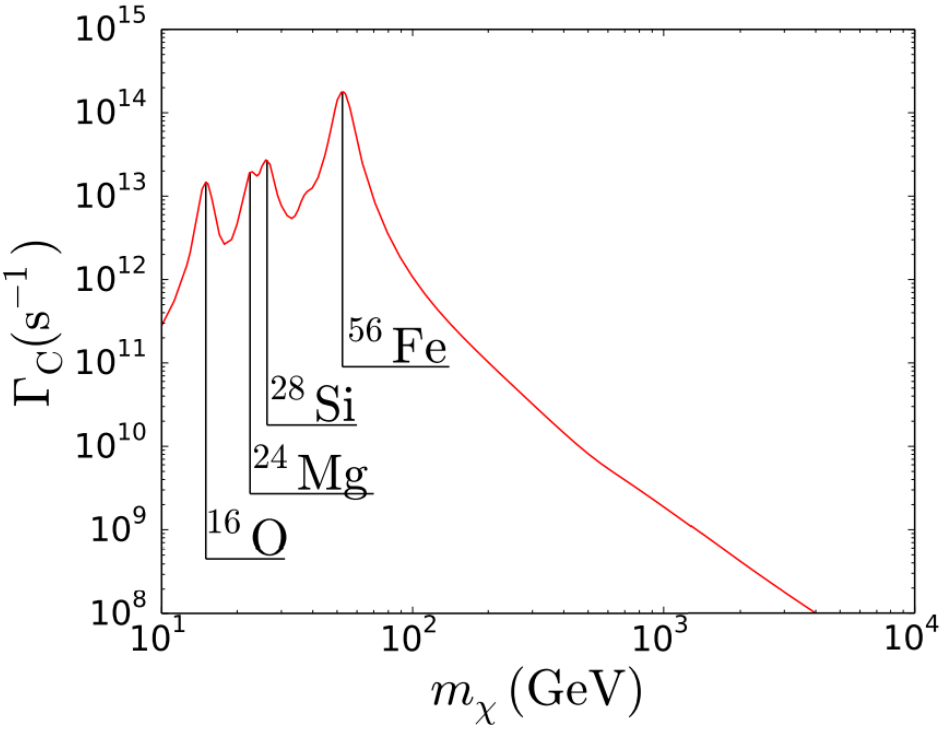

Figure 4.6 DM capture rate in the Earth as function of DM mass for a spin-independent cross section of 10^{-44} cm^2, based on [80]. The peaks indicate the resonant capture of the most abundant elements in the Earth, taken from [13].

As described in this chapter, the IceCube collaboration sets upper limits on the total DM annihilation rate by the non-observation of an exotic neutrino flux and transfers its results to constraints on the DM-nucleon cross section, using the above given assumptions. Details about the procedure to constrain DM properties with IceCube observations with a focus on a formalism to set rigorous upper limits on the coupling strengths of the non-relativistic effective theory of DM-nucleon interactions and the corresponding DM-nucleon cross sections are presented in the next chapter.

5 Constraining dark matter properties with IceCube observations of the Earth's center

In this chapter the theoretical background and method, to obtain constraints on DM properties, namely on the coupling strengths of the non-relativistic effective theory of DM - nucleon interactions including operator interference and on the corresponding DM-nucleon cross-sections, are described. Commonly, as also in the IceCube results [13], the DM interactions with the nucleons are assumed to be identical for protons and neutrons, called an isoscalar interaction, which is very restrictive and not always the case [83] [84]. Instead interference between isoscalar and isovector interactions, where protons and neutrons are treated differently, can be included. This will result in higher upper limits on the cross section for the reported upper limit on the DM annihilation rate [16]. Furthermore not only spin-independent and spin-dependent DM-nucleon interactions can be considered. In the non-relativistic effective theory of DM-nucleon interactions exists a large set of Galilean invariant operators with additional nuclear response functions as seen in section 3.3. These operators have been included in an analysis to infer upper limits on the coupling strengths of the effective theory without incorporation of interference for IceCube observations of the Earth [12]. But as described above, interference between isoscalar and isovector interactions leads to an increase in the upper limits on the cross section. In addition interference between the different interaction types can exist, which leads to even more relaxed upper limits. A method, to include the entire interference, has been introduced and applied on IceCube data for the Sun [16]. The Earth contains additional chemical elements with relevant abundances, compared to the Sun, and in contrast to the Sun equilibrium between DM capture and annihilation can't be considered to be reached. For that reason the method to obtain rigorous constraints on the effective theory of DM-nucleon interactions including operator interference under consideration of the non-equilibrium of DM capture and annihilation is applied on IceCube data for the Earth in this work and described in the following. Hereby the investigation is restricted to DM spin up to 1/2 with 8 interactions in the effective field theory for spin-0 DM and 28 interactions for spin-1/2 DM.

By the non-observation of an excessive neutrino flux, compared to the background, an upper limit on the total DM annihilation rate $\Gamma_A(C) \leq \Gamma_A^{\text{u.l.}}$ is set for a given annihilation channel and DM mass by the IceCube collaboration. This limit can be used via equation 3.4 to put an upper limit on the capture rate for the given DM mass and annihilation channel: $C \leq C^{\text{u.l.}}$. From this requirement upper bounds on the coupling strengths c_i^τ from equation 3.23 can be derived. These upper limits are, as described above, commonly received under the assumption, that all other coupling strengths are zero, which in general is not the case and leads to upper limits on the coupling strengths, that are too much constrained [16]. Instead a larger region in parameter space is allowed by the condition $C \leq C^{\text{u.l.}}$, which includes points violating the commonly derived upper limits. This is demonstrated for 2 coupling strengths, spanning a 2-dimensional **c**-space in figure 5.1, where all points on and inside the ellipse are allowed. In this figure a rigorous upper limit on the coupling strength c_α is given by $\max\{c_\alpha\}$ and not by $\max c_\alpha|_{c_\beta=0}$. This concept can be extended to the whole 28-dimensional **c**-space, spanned by the 28 coupling strengths of the effective theory.

In order to compute the maximum value of the α-th component of the vector **c** under the basic condition $\Gamma_A(C) \leq \Gamma_A^{\text{u.l.}}$ including the whole 28-dimensional **c** space, a Lagrangian is constructed [16]:

$$L = c_\alpha - \lambda \left[\Gamma_A(C) - \Gamma_A^{\text{u.l.}}\right] , \tag{5.1}$$

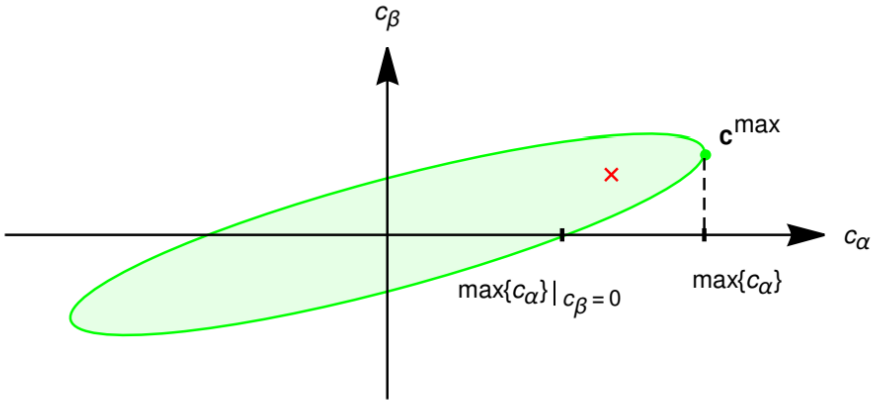

Figure 5.1 In green the allowed region by the condition $C \leq C^{\text{u.l.}}$ in the 2-dimensional parameter space is shown. The point $\max\{c_\alpha\}|_{c_\beta=0}$ is commonly used as upper limit for the coupling strength c_α, although e.g. the point, marked with a red cross, with a higher c_a value is allowed, too. The rigorous maximum value for c_α is reached at the point $\mathbf{c}^{\max}$ with the value $\max\{c_\alpha\}$ for c_α. The figure is taken from [16].

where λ is a Lagrange multiplier. For the total annihilation rate at the present time $\Gamma_A(C)$ as a function of the capture rate equation 3.4 is rewritten as:

$$\Gamma_A(C) = \frac{C}{2} \tanh^2\left(\kappa\sqrt{C}\right) \tag{5.2}$$

$$\text{with} \qquad \kappa = t_\oplus \sqrt{C_A}\ . \tag{5.3}$$

For $\mathbf{c}^{\max}$ as the point, where the maximum value $\max\{c_\alpha\} = c_\alpha^{\max}$ for the coupling strength c_α is obtained, the optimization conditions are:

$$\left.\frac{\partial L}{\partial c_\beta}\right|_{\mathbf{c}=\mathbf{c}^{\max}} = \delta_{\alpha\beta} - 2\lambda \left.\frac{\partial \Gamma_A(C)}{\partial C}\right|_{\mathbf{c}^{\max}} \mathbb{C}_{\beta\zeta} c_\zeta^{\max} = 0 \tag{5.4}$$

$$\left.\frac{\partial L}{\partial \lambda}\right|_{\mathbf{c}=\mathbf{c}^{\max}} = \Gamma_A[C(\mathbf{c}^{\max})] - \Gamma_A^{\text{u.l.}} = 0\ . \tag{5.5}$$

It follows from the first condition 5.4 with $\xi = (2\lambda \partial\Gamma_A(C)/\partial C\big|_{\mathbf{c}^{\max}})^{-1}$:

$$c_\beta^{\max} = \xi(\mathbb{C}^{-1})_{\alpha\beta}\ . \tag{5.6}$$

$c_\beta^{\max}$ can be used to express the capture rate of equation 3.23. Substituting the result together with equation 5.2 into the second condition 5.5; one obtains:

$$\frac{1}{2}\xi^2(\mathbb{C}^{-1})_{\alpha\alpha} \tanh^2\left(\kappa\xi\sqrt{(\mathbb{C}^{-1})_{\alpha\alpha}}\right) = \Gamma_A^{\text{u.l.}}\ . \tag{5.7}$$

By calculating the root ξ_0 of ξ^2 numerically, the maximum value of the coupling strength c_α can be determined via:

$$c_\alpha^{\max} = \xi_0(\mathbb{C}^{-1})_{\alpha\alpha}\ . \tag{5.8}$$

The last two steps can be combined to one equation, by substituting ξ_0 from equation 5.8 into the square root of equation 5.7:

$$c_\alpha^{\max} \tanh\left(\frac{\kappa}{\sqrt{(\mathbb{C}^{-1})_{\alpha\alpha}}} c_\alpha^{\max}\right) = \sqrt{2(\mathbb{C}^{-1})_{\alpha\alpha}\Gamma_A^{\text{u.l.}}} \,. \tag{5.9}$$

This equation is used in this work to determine numerically the upper limits $c_\alpha^{\max}$ on the coupling strengths c_α and therefor also the maximum values $\max\{c_i^\tau\}$ of the coupling strengths c_i^τ, corresponding to them. The equation 5.9 can also be used for any subspace of the 28-dimensional $\mathbf{c}$ space, for example when only a subset of the operators of the effective theory is used in a certain model. The results in chapter 6 are shown for the case of no interference, where $(\mathbb{C}^{-1})_{\alpha\alpha} = (\mathbb{C}_{\alpha\alpha})^{-1}$, for interference between the isoscalar and isovector interaction for each operator and for interference between all interactions for each operator. Hereby the most stringent upper limits are received without interference according to equation 5.8, as it holds for the $\mathbb{C}$ matrix: without interference $(\mathbb{C}^{-1})_{\alpha\alpha} = (\mathbb{C}_{\alpha\alpha})^{-1} \leq (\mathbb{C}^{-1})_{\alpha\alpha}$ with interference.

In equation 5.9 the results for $c_\alpha^{\max}$ depend on the upper limits on the total DM annihilation rate $\Gamma_A^{\text{u.l.}}$, the matrix $\mathbb{C}$ and via κ from equation 5.3 on the annihilation constant C_A, which in turn depends on the annihilation cross section $< \sigma_A v >$ through equation 3.11. The equilibrium time τ depends according to equation 3.3 also via C_A on $< \sigma_A v >$. For that reason the upper limits $c_\alpha^{\max}$ change according to the assumed annihilation cross section, which also implies a changing equilibrium time τ. In the results, presented in chapter 6, the upper limits are shown once for the thermal relic annihilation cross section of $< \sigma_A v >_{\text{th}} = 3 \cdot 10^{-26} \text{cm}^3\text{s}^{-1}$ and once for different annihilation cross sections, that are chosen to be multiples of $< \sigma_A v >_{\text{th}}$. In addition the results are shown in comparison to other DM detection experiments. This comparison is possible, as similar expressions, in order to obtain upper limits on the coupling strengths, hold for direct detection experiments. Hereby the nuclear recoil event rate is given by $R(\mathbf{c}) = \mathbf{c}^T \mathbb{R} \mathbf{c}$ and is bounded by $R \leq R^{\text{u.l.}}$. But it is important to note, that the upper limits $c_\alpha^{\max}$ from direct detection experiments are independent of DM annihilation and the corresponding annihilation cross section and thus also of the equilibrium time of DM capture and annihilation. Thus the formulae change as in the case, if equilibrium was already attained [16]. The Lagrangian to compute the upper limit on the α^{th} component of the 28-dimensional vector $\mathbf{c}$ under the constraint $C \leq C^{\text{u.l.}}$, when DM capture-DM annihilation equilibrium is reached, reads:

$$L = c_\alpha - \lambda \left[\mathbb{C}(\mathbf{c}) - C^{\text{u.l.}}\right] \,, \tag{5.10}$$

with λ as a Lagrange multiplier. The optimization conditions are:

$$\left.\frac{\partial L}{\partial c_\beta}\right|_{\mathbf{c}=\mathbf{c}^{\max}} = \delta_{\alpha\beta} - 2\lambda \mathbb{C}_{\beta\zeta} c_\zeta^{\max} = 0 \tag{5.11}$$

$$\left.\frac{\partial L}{\partial \lambda}\right|_{\mathbf{c}=\mathbf{c}^{\max}} = \mathbb{C}(\mathbf{c}^{\max}) - \mathbb{C}^{\text{u.l.}} = 0 \,. \tag{5.12}$$

$\mathbf{c}^{\max}$ is the point on the ellipse where the maximum value $\max\{c_\alpha\} = c_\alpha^{\max}$ for c_α is attained. From the condition 5.11 the β^{th} component of $\mathbf{c}^{\max}$ can be obtained:

$$c_\beta^{\max} = \frac{1}{2\lambda}(\mathbb{C}^{-1})_{\alpha\beta} \,. \tag{5.13}$$

$c_\beta^{\max}$ can again be used to express the capture rate of equation 3.23. Substituting the result into the second condition 5.12, one obtains for the Lagrange multiplier: $\lambda = \frac{1}{2}\sqrt{(\mathbb{C}^{-1})_{\alpha\alpha}/\mathbb{C}^{\text{u.l.}}}$. With this expression for λ the maximum value of the coupling strength c_α can be determined:

$$c_\alpha^{\max} = \sqrt{(\mathbb{C}^{-1})_{\alpha\alpha}\mathbb{C}^{\text{u.l.}}} \,. \tag{5.14}$$

This formula for $c_\alpha^{\max}$ can be used for indirect detection, where DM capture and annihilation equilibrium has already been attained like in the Sun [16], and for direct detection in an analogous form. Details about the derivation of upper limits on the coupling strengths from the non-observation of a significant excess in the number of nuclear recoil events in direct detection experiments are given in [15].

In order to compare results and depending on the application, a change of basis may be feasible, like from the isoscalar-isovector basis to the neutron-proton basis. In an alternative basis the upper limits on the coupling strengths from equation 5.8 and 5.14 respectively read:

$$\tilde{c}_\alpha^{\max} = \xi_0(\tilde{\mathbb{C}}^{-1})_{\alpha\alpha} \tag{5.15}$$

$$\tilde{c}_\alpha^{\max} = \sqrt{(\tilde{\mathbb{C}}^{-1})_{\alpha\alpha}\mathbb{C}^{\text{u.l.}}}\ . \tag{5.16}$$

The matrix $\tilde{\mathbb{C}}$ in the new basis can be calculated ab initio or more conveniently by a basis transformation of the results in the old basis. The basis transformation of the coupling strengths $\mathbf{c}$-vector is obtained by:

$$\tilde{\mathbf{c}} = \mathbb{T}\mathbf{c}\ . \tag{5.17}$$

With the condition, that the capture rate is independent of the chosen basis one obtains:

$$C(\mathbf{c}) = \mathbf{c}^T\mathbb{C}\mathbf{c} = \tilde{\mathbf{c}}^T\tilde{\mathbb{C}}\tilde{\mathbf{c}}\ . \tag{5.18}$$

With equation 5.17 for the basis transformation of the $\mathbf{c}$-vector of the coupling strengths the matrix $\tilde{\mathbb{C}}$ in the new basis thus reads:

$$\tilde{\mathbb{C}} = (\mathbb{T}^T)^{-1}\mathbb{C}\mathbb{T}^{-1}\ . \tag{5.19}$$

According to equation 3.14 the $\mathbb{T}$-Matrix for the transformation from the isoscalar-isovector basis $\mathbf{c} = \{c_i^0, c_i^1\}$ to the neutron-proton basis $\mathbf{c} = \{c_i^{\text{n}}, c_i^{\text{p}}\}$ reads for a single operator O_i:

$$\mathbb{T}_{2x2} = \frac{1}{2}\begin{pmatrix} 1 & -1 \\ 1 & 1 \end{pmatrix} \tag{5.20}$$

For the whole 28-dimensional $\mathbf{c}$-space the $\mathbb{T}$-matrix for all 14 operators is a 28x28 block diagonal matrix, consisting of the 2x2-matrices $\mathbb{T}_{2x2}$ on the diagonal:

$$\mathbb{T}_{28x28} = \begin{pmatrix} \mathbb{T}_{2x2} & 0 & \cdots & 0 \\ 0 & \ddots & \ddots & \vdots \\ \vdots & \ddots & \ddots & 0 \\ 0 & \cdots & 0 & \mathbb{T}_{2x2} \end{pmatrix}_{28x28} \tag{5.21}$$

Based on these formulae the upper limits on the coupling strengths can be calculated in any basis, like the neutron-proton basis, with the original calculated $\mathbb{C}$-Matrix in the isoscalar-isovector basis as a starting point. The impact of interference on the upper limits of the coupling strengths depends hereby strongly on the chosen basis. This is shown in figure 5.2, where the green ellipse demonstrates the allowed region in the parameter space for the O_1 operator including interference. As seen there, the maximum values for the coupling strengths coincide in the isoscalar-isovector basis in case of interference and no interference, so that $\max\{c_1^0\} = \max\{c_1^0\}|_{c_1^1=0}$ and $\max\{c_1^1\} = \max\{c_1^1\}|_{c_1^0=0}$, whereas in the neutron-proton base the maximum values for the coupling strengths are larger in case of interference: $\max\{c_1^{\text{n}}\} \geq \max\{c_1^{\text{n}}\}|_{c_1^{\text{p}}=0}$ and $\max\{c_1^{\text{p}}\} \geq \max\{c_1^{\text{p}}\}|_{c_1^{\text{n}}=0}$.

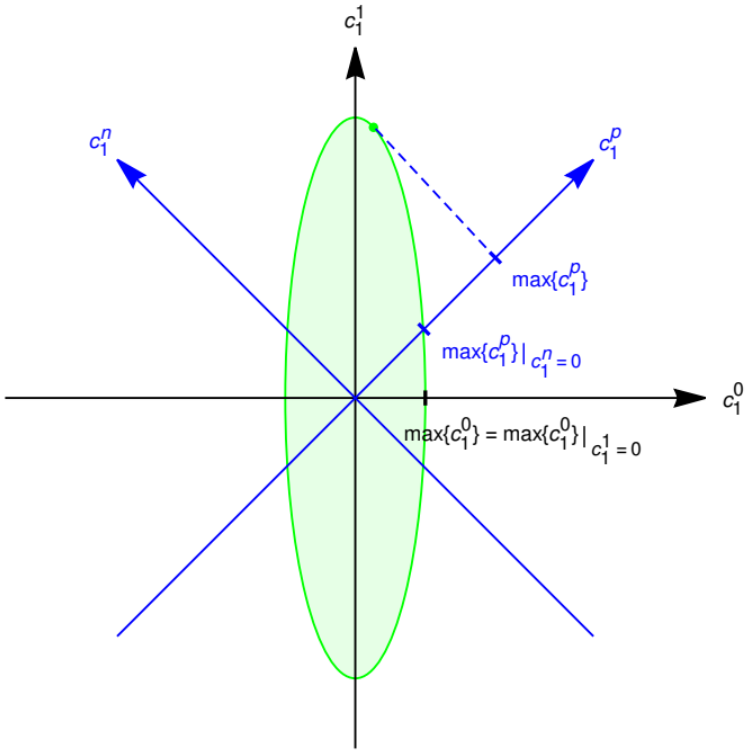

Figure 5.2 In this picture the influence of the chosen basis on the impact of interference is shown. The green ellipse demonstrates the allowed region in the parameter space for the O_1 operator including interference. In the isoscalar-isovector basis the axes of the ellipse are aligned with the axes of the coordinate system, so that the upper limit on c_1^0 coincides in case of interference and in case of no interference, where $c_1^1 = 0$: $\max\{c_1^0\} = \max\{c_1^0\}|_{c_1^1=0}$. Instead in the neutron-proton basis the axes of the ellipse are misaligned with the respective coordinate system and therefor: $c_1^{\mathrm{n}} \neq 0$ at the point for the upper limit on c_1^{p} including interference, so that: $\max\{c_1^{\mathrm{p}}\} \geq \max\{c_1^{\mathrm{p}}\}|_{c_1^{\mathrm{n}}=0}$. The figure is taken from [16].

Commonly in the literature it is assumed, that the only non-vanishing coupling constant is the isoscalar component c_i^0. Also the IceCube collaboration presents its results, the spin independent and spin dependent DM-nucleon cross section for a spin 1/2 DM particle, under this assumption. The constraints on $c_1^{\mathcal{N}}$ and $c_4^{\mathcal{N}}$ in the neutron-proton basis with and without interference can be translated into constraints on the spin independent (SI) and spin dependent (SD) cross section via [16]:

$$\begin{aligned} \sigma_{\chi\mathcal{N}}^{\mathrm{SI}} &= \frac{\mu_{\mathcal{N}}^2 (c_1^{\mathcal{N}})^2}{\pi} \\ \sigma_{\chi\mathcal{N}}^{\mathrm{SD}} &= \frac{3}{16} \frac{\mu_{\mathcal{N}}^2 (c_4^{\mathcal{N}})^2}{\pi} \,. \end{aligned} \tag{5.22}$$

With these equations the calculations of this work can be compared to published results. In general the upper limits including interference will be less restrictive than the bounds, where interference is neglected and DM couples with equal strength to protons and neutrons, but they are applicable to all models considering the respective interference and impose a rigorous upper limit on the coupling strengths. The results, that were attained by using the above presented formalism on IceCube observations of the Earth's center, are shown in the next chapter.

6 Results from IceCube data

A search for an exotic neutrino flux from the center of the Earth, induced by DM annihilations, with the IceCube Neutrino Observatory was conducted during 2011 and 2012, collecting data from 327 days of detector livetime [13]. No excess beyond the expected background from atmospheric neutrinos was detected, leading to an upper limit on the neutrino flux from DM annihilations in the Earth. Based on this observation the IceCube collaboration published upper limits on the total DM annihilation rate and the spin-independent cross section at the 90% confidence level for 11 DM masses between 10 GeV and 10 TeV, assuming a soft and two hard channels and a thermal relic annihilation cross section. The soft channel hereby refers to annihilation into $b\bar{b}$, while the two hard channels refer to annihilation into W^+W^- for DM masses larger than the rest mass of the W boson and annihilation into $\tau^+\tau^-$ for lower DM masses. Based on the reported upper limit on the total annihilation rate from IceCube, rigorous upper limits on the coupling strengths of the non-relativistic effective theory and on the corresponding DM-nucleon cross sections are derived according to the above described formalism. First the results are presented for the thermal relic annihilation cross section, then for different annihilation cross sections, given as multiples of the thermal annihilation cross section, and finally in comparison to the results from other experiments.

6.1 Constraints on the coupling strengths

In this section constraints on the coupling strengths under the assumption of the thermal relic annihilation cross section are presented. They werde derived by evaluating equation 5.9 with the procedure described in chapter 5 and are based on the reported upper limits on the total DM annihilation rate from IceCube. The results, multiplied with the squared rest mass of the W boson m_W, as function of the DM mass [$m_\chi = (10, 20, 35, 50, 100, 250, 500, 1000, 3000, 5000, 10000)$ GeV] in the isoscalar-isovector basis assuming the thermal relic annihilation cross section and the hard channels are shown in figures 6.1 and 6.2. In each subfigure the blue lines show upper limits on the isoscalar coupling strength c_i^0 and the red lines on the isovector coupling strength c_i^1. The solid line shows the result under the assumption, that the depicted coupling strength describes the only non-zero interaction, which means, that there exists no interference. The results considering an isoscalar-isovector interference are depicted as dashed lines. So in this case c_i^0 and c_i^1 can be non-zero, while all other coupling strengths vanish. The dotted line shows the results, when all coupling strengths are non-zero and interference between all operators occurs. The strongest constraints on the coupling strengths are obtained in case of no interference, which can also be seen from equation 5.8. The upper limits become the most relaxed for interference between all interactions.

For each coupling strength c_i^τ, where $i = 1, 3, ..., 15$ and $\tau = 0, 1$ the impact of interference is different. The upper limits on the coupling strengths are relaxed under isoscalar-isovector interference by about 2 orders of magnitude for c_4^τ, c_6^τ, c_7^τ, c_9^τ, c_{10}^τ and c_{14}^τ and only by a small factor e.g. for c_3^τ, c_5^τ and c_{15}^τ. This depends on the off-diagonal elements of the $\mathbb{C}$ matrix and is therefor, as seen in figure 5.2, dependent on the chosen basis, here the isoscalar-isovector basis. The smaller the off-diagonal elements are compared to the diagonal elements, the more the allowed region is aligned with the axes of the parameter space. So in a geometrical perspective the orientation and elongation of the ellipses in the parameter space determine the impact of interference on the respective coupling strength. The more the ellipses are elongated and misaligned with the c_i^0 - c_i^1 axes, the stronger is the impact. This can be seen in figure 6.3, where the allowed regions in the $c_i^0 - c_i^1$ parameter space at the 90 % confidence level for all operators are shown for a DM mass of 50 GeV, as with this DM mass the upper limits are the most constraint for the majority

of the interactions. As seen here the ellipses of c_4^τ, c_6^τ, c_7^τ, c_9^τ, c_{10}^τ and c_{14}^τ are elongated and lie on the diagonal of the parameter space, which leads to a high impact of the isoscalar-isovector interference on the upper limits. As a remark: By projecting the vertex and co-vertex of the ellipses on the $c_i^0 - c_i^1$ axes, the upper limits in case of no interference are obtained. The impact of interference between all operators on the upper limits is determined by the DM response functions, defined in appendix B, where products between coupling strengths represent this interference. There exists no interference between all operators for c_7^τ and c_{10}^τ. For that reason the upper limits for interference among all operators are the same as for isoscalar-isovector interference for these two coupling strengths. In general the following interference between all interactions is possible: $c_1^\tau c_3^\tau$, $c_4^\tau c_5^\tau$, $c_4^\tau c_6^\tau$, $c_8^\tau c_9^\tau$, $c_{12}^\tau c_{15}^\tau$ and $c_{11}^\tau c_{12}^\tau c_{15}^\tau$ resulting to the observed impact on the upper limits of the coupling strengths under interference between all operators. It is important to note, that points above the solid lines are not necessarily excluded, whereas points above the dotted lines are for all DM models in conflict with the IceCube measurements under the given assumptions.

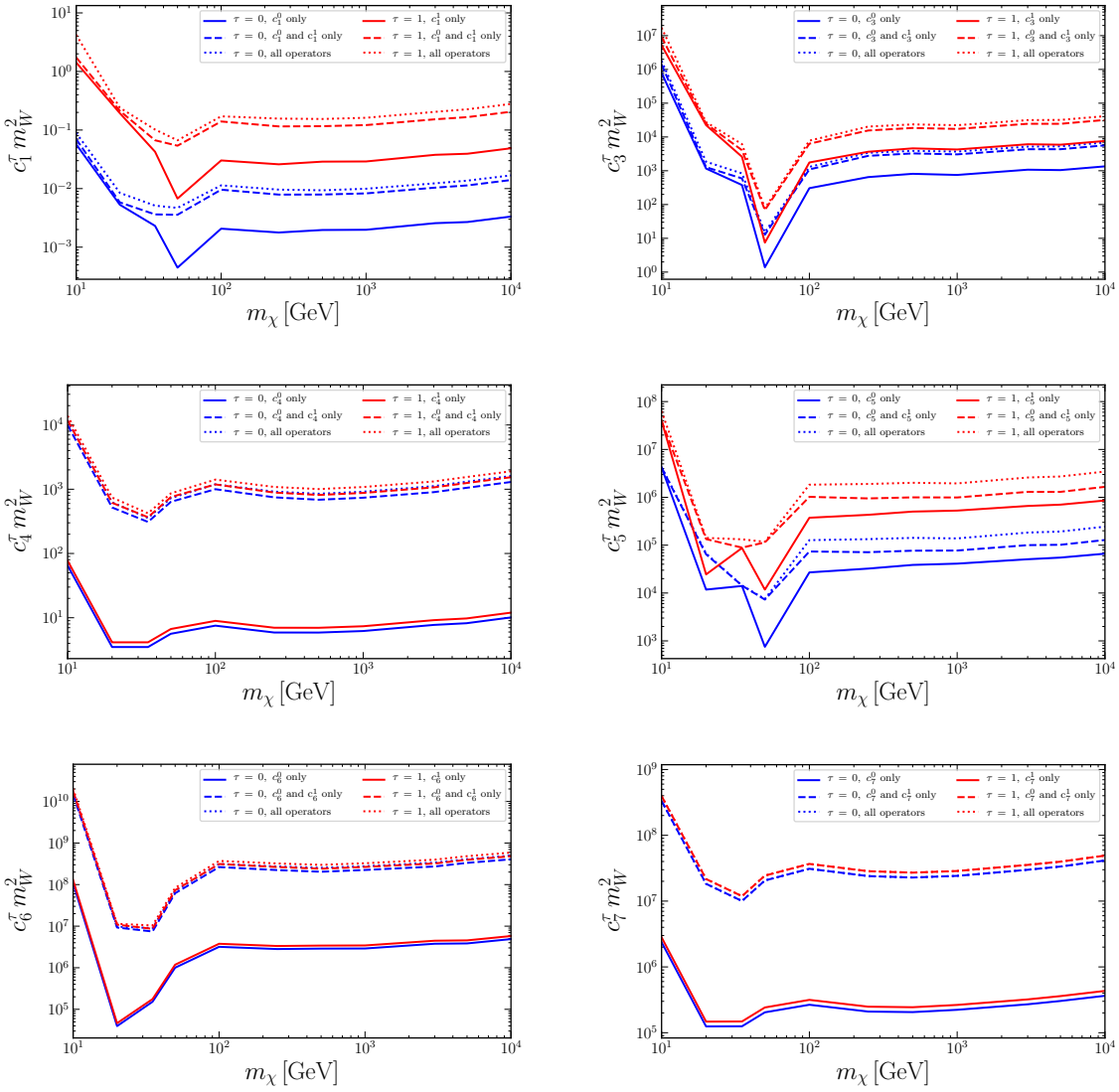

Figure 6.1 Upper limits on the coupling strengths c_i^τ, $\tau = 0, 1$, $i = 1, 3, ...7$ of the non-relativistic effective theory of DM-nucleon interactions at the 90% confidence level as function of the DM mass m_χ assuming the hard channels and the thermal relic annihilation cross section. In blue are the upper limits on the isoscalar coupling strength c_i^0 and in red on the isovector coupling strength c_i^1. For each coupling strength the solid line shows the results considering no interference, the dashed line shows the results considering isoscalar-isovector interference, and the dotted line shows the results considering interference between all operators $O_j^\tau, \tau = 0, 1$, $j = 1, 3, ...15$.

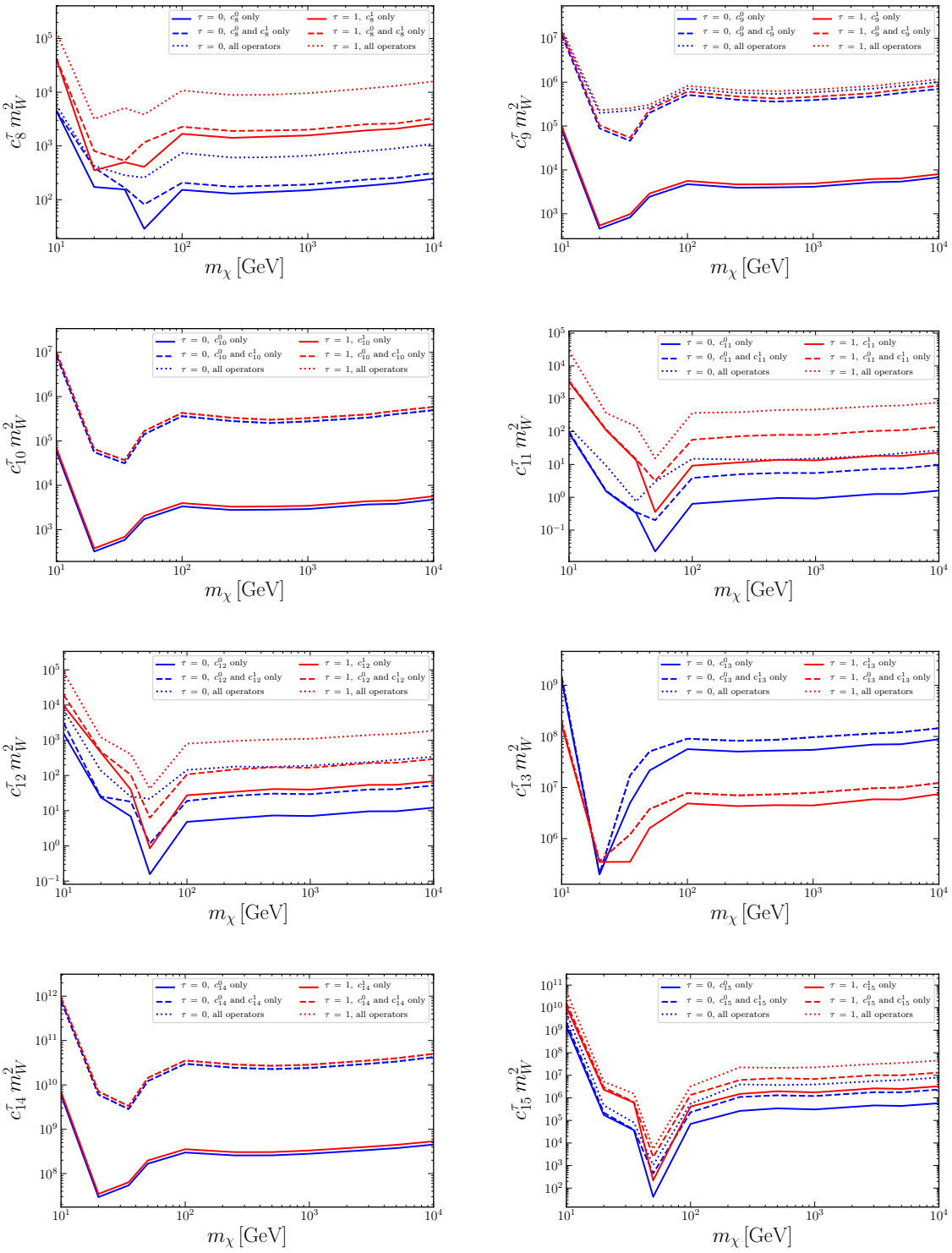

Figure 6.2 Same as figure 6.1 for coupling strengths c_i^τ, $\tau = 0, 1$, $i = 8, ..., 15$.

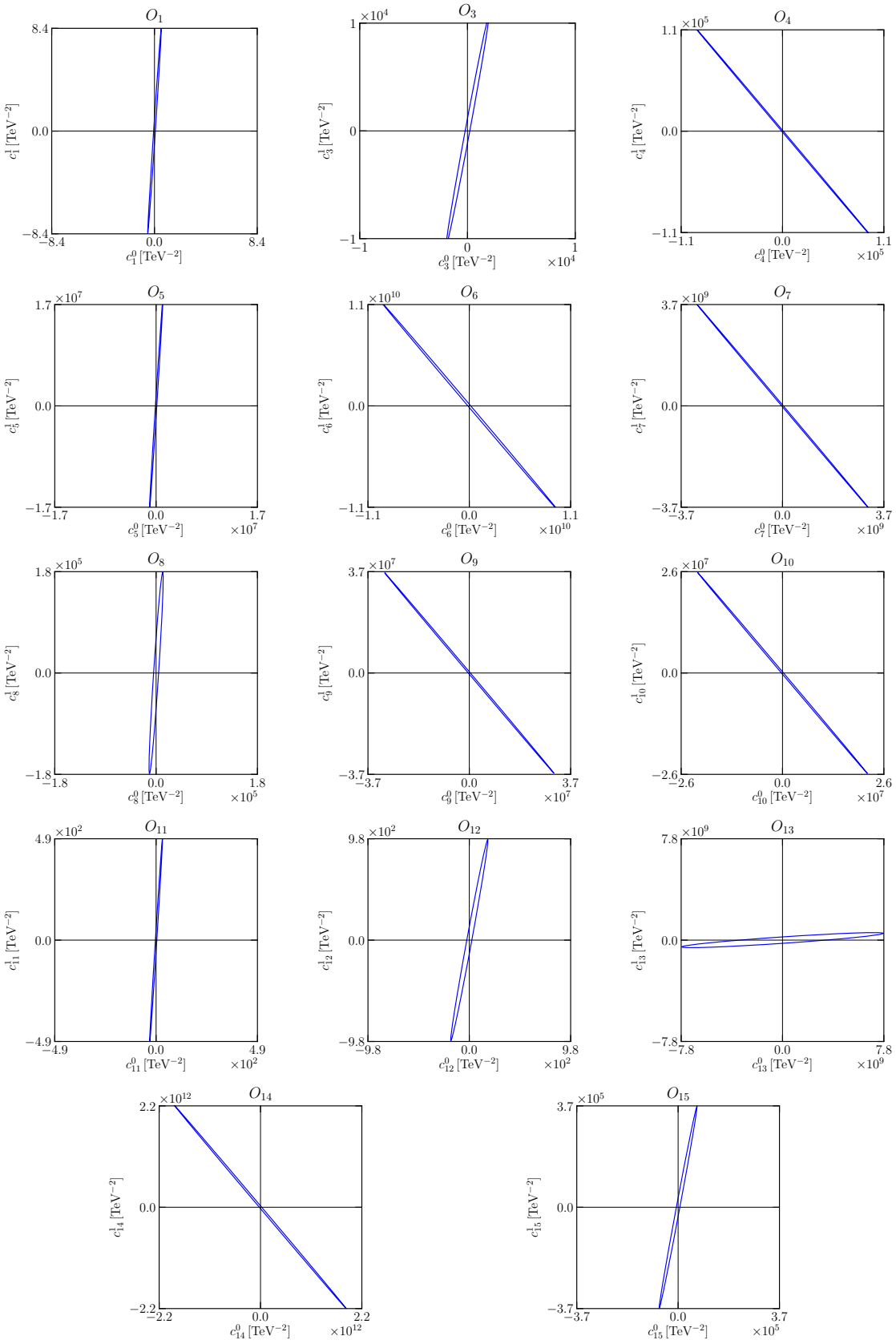

Figure 6.3 Allowed regions in the $c_i^0 - c_i^1$ parameter space at the 90 % confidence level, representing the values of the coupling strengths for isoscalar-isovector interference, allowed by the upper limits on the total annihilation rate by IceCube, for a DM mass of 50 GeV and the hard channels assuming the thermal relic annihilation cross section.

A prominent feature of the upper limits on the coupling strengths in figures 6.1 and 6.2 is the significant drop of the constraints on c_1^τ, c_3^τ, c_5^τ, c_8^τ, c_{11}^τ, c_{12}^τ and c_{15}^τ at a DM mass of 50 GeV. The reason for this lower upper limit is the resonant capture of DM by ^{56}Fe, the most abundant element in the Earth's core (see appendix A). The nuclear response functions of ^{56}Fe $W_M^{\tau\tau'}$, $W_{\Phi''}^{\tau\tau'}$ and $W_{M\Phi''}^{\tau\tau'}$ from appendix C are, together with the DM response functions from appendix B, directly connected to the relevant coupling strengths via equation 3.16 for the DM-nucleon cross section. Therefor the most constraining upper limits for many interactions are reached at a DM mass of 50 GeV, as already mentioned in section 4.3 for the special case of the spin-independent cross section reported by IceCube. The other resonant peaks, reported there for ^{16}O, ^{24}Mg and ^{28}Si, cannot be resolved in the calculations here, most probably due to the large binning of the probed DM masses. But there are more significant dips in the upper limits on the coupling strengths for other interactions, resulting from resonant peaks. For example there is also a strongly improved upper limit on c_6^τ and c_{13}^τ at a DM mass of about 20 GeV - 30 GeV, which can be explained by resonant capture of DM by ^{23}Na, ^{27}Al and ^{31}P. The constraints on these coupling strengths are not very strong, so that also elements with a small abundance can change results in this case significantly. Thus depending on the interaction the most stringent constraints are obtained for different DM masses.

The IceCube collaboration presents its results for the DM search in the Earth in terms of the spin-independent DM-nucleon cross section under the assumption, that the interaction is isoscalar [13]. They are shown in figure 4.3. In order to compare the results of this work with the published results from IceCube, the spin-independent DM-nucleon cross section $\sigma_{\chi\mathcal{N}}^{\mathrm{SI}}$ and additionally the spin-dependent DM-nucleon cross section $\sigma_{\chi\mathcal{N}}^{\mathrm{SD}}$ are calculated according to equation 5.22 in the neutron-proton basis and depicted in figure 6.4 as function of the DM mass. The cyan lines represent the constraints on the DM-neutron cross sections and the violet lines on the DM-proton cross sections. Hereby the solid lines show the upper limits on the DM-nucleon cross sections assuming that the only non-zero coupling constant is the isoscalar component c_1^0 for the spin-independent DM-nucleon cross section and the isoscalar component c_4^0 for the spin-dependent DM-nucleon cross section without interference. As the interaction is isoscalar, the upper limits should be the same for the DM-proton cross sections and the DM-neutron cross sections, so that the solid lines overlap. A small difference results however from the mass difference of order 10^{-3} between neutron and proton, which is below the resolution limit of the figures. The dashed lines show the results assuming that both c_1^0 and c_1^1 for the spin-independent DM-nucleon cross section and c_4^0 and c_4^1 for the spin-dependent DM-nucleon cross section can be non-zero and interfere, whereas all other coupling strengths vanish. The dotted lines show the upper limits on the DM-nucleon cross sections under the assumption, that all coupling strengths can be non-zero and interfere. The upper limits under the assumption of interference for the spin-independent DM-nucleon cross section are about 3 to 4 orders of magnitude larger than the ones without interference. For the spin-dependent DM-nucleon cross section they are about 3 orders of magnitude larger than without interference in case of DM-proton interaction and about 5 orders of magnitude larger in case of DM-neutron interaction. Consequently the constraints respecting interference between all operators, which are applicable to all DM models, are much more relaxed than the upper limits published by the IceCube collaboration, which are obtained under the assumption of isoscalar interaction only.

The published results can however be directly compared with the calculated upper limits on the spin-independent DM-nucleon cross section in case of no interference, in order to assess the accurateness of computations. Between a DM mass of 20 GeV and 100 GeV the calculated upper limits are about a factor of 2 to 3 smaller than the published ones, whereby the closest result is given for a DM mass of 50 GeV. For DM masses below and above this interval the factor increases in each direction to about at most 1 order of magnitude. Thus the calculated upper limits on the spin-independent cross section in case of no interference of this work are more constrained than the the published upper limits for all DM masses, but within or at most at 1 order of magnitude. This difference can be explained on the one hand side by the used Earth model. The internal structure and composition of the Earth differs between various models, which in consequence leads to different DM capture rates for the elements in the Earth and thus

to a different final result for the DM-nucleon cross sections. On the other hand also the accuracy of the numerical calculations of the $\mathbb{C}$ matrix influences the results, e.g. by the precision of the numerical algorithms of integration and by the accuracy of the DM velocity distribution. In order to obtain as exact as possible results one should go beyond the leading order in the calculations for the DM capture rate, which is however also limited by the given accuracy of the different nuclear response functions listed in appendix C, that are calculated polynomial fits of nuclear shell models provided in [12] and [52]. Thus the observed difference between the published and calculated results can be reasonably explained. Finally, as mentioned before, the resonant peaks of ^{16}O, ^{24}Mg and ^{28}Si in the published results cannot be resolved in the calculations of this work, most probably due to the large binning of the probed DM masses, but still the results are in agreement with the published results within or at most at 1 order of magnitude.

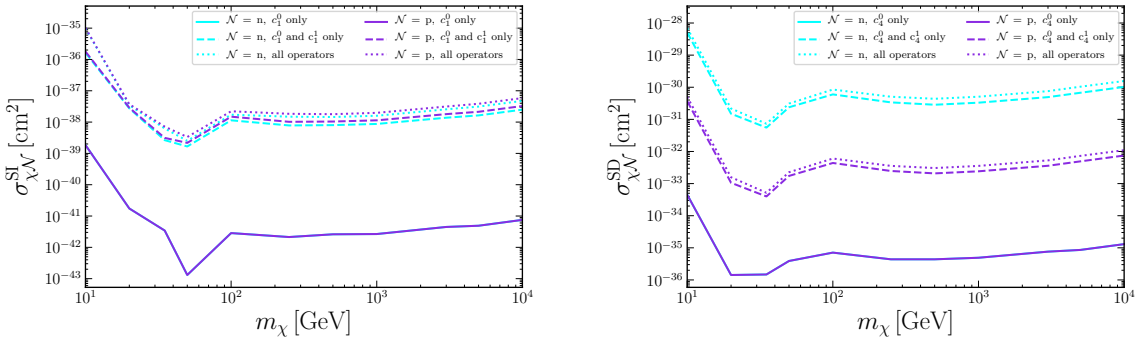

Figure 6.4 Upper limits on the spin-independent DM-nucleon cross section $\sigma^{SI}_{\chi\mathcal{N}}$ on the left and on the spin-dependent DM-nucleon cross section $\sigma^{SD}_{\chi\mathcal{N}}$ on the right at the 90% confidence level as function of the DM mass m_χ assuming the hard channels and the thermal relic annihilation cross section. In cyan are the upper limits on the DM-neutron cross sections and in violet on the DM-proton cross sections. The solid line shows the results considering no interference, i.e. c_1^0 is the only non-zero coupling strength for the spin-independent DM-nucleon cross section and c_4^0 the only one for the spin-dependent DM-nucleon cross section. The dashed line shows the results considering that c_1^0 and c_1^1 can be non-zero and interfere for the spin-independent DM-nucleon cross section and c_4^0 and c_4^1 can be non-zero and interfere for the spin-dependent DM-nucleon cross section. The dotted line shows the results considering interference between all interactions of the effective theory.

The accuracy of the nuclear response functions influences the upper limits under the assumption of interference in a special way, as the ensuing matrices are needed for their calculation. The matrices have to be positive definite, in order to be able to use the method described in chapter 5 to determine the upper limits on the coupling strengths under interference with equation 5.9 and 5.14. Else there will be negative entries on the diagonals of the inverse matrices and the upper limits on the coupling strengths become imaginary. For some elements like ^{31}P there exist nuclear response matrices, that are, due to accuracy, not positive definite for zero and small momentum transfers, which are especially important for a rather small celestial body like the Earth (The variable y of the polynomial fits for the nuclear response functions is dependent on the squared momentum transfer q as seen in appendix C). Nevertheless the method can be applied to the Earth, as also higher momentum transfers are incorporated and all elements together determine the final calculated $\mathbb{C}$ matrix of the Earth, which thus becomes positive definite. Thus this accuracy error, which is particularly relevant when the determinant is very small compared to the matrix elements and the eigenvalues are very hierarchical leading to elongated allowed parameter spaces, has a special impact on the upper limits under interference. Additional errors in the numerical calculations occur, as mentioned before, e.g. from the numerical algorithms of integration and from the DM velocity distribution.

A way to calculate the propagation of all these numerical errors and their impact on the final $\mathbb{C}$ matrix and on the upper limits on the coupling strengths under interference is presented in [15]. The accuracy of the used nuclear response functions is of order 10^{-5}. Taking only this accuracy into account and using the method described in [15] the calculated upper limits on all coupling strengths for an isoscalar-isovector interference differ from the true values by a factor of 10^{-2}. To receive results for all coupling strengths under isoscalar-isovector interference with a difference to the true values smaller than or equal to a factor of order 1, the total numerical precision has to be smaller than or equal to 10^{-4}. For a numerical precision larger than 10^{-3} the difference between calculated and true values for the upper limits on the coupling strengths under isoscalar-isovector interference becomes larger than 1 order of magnitude. In the isoscalar-isovector basis the impact of the numerical precision is especially relevant for the upper limits on the coupling strengths c_4, c_6, c_7, c_9, c_{10} and c_{14} under isoscalar-isovector interference, whereas for the other coupling strengths the relative errors are 2 orders of magnitude smaller than for the previous mentioned ones. As seen in figure 6.3 the ellipses of c_4, c_6, c_7, c_9, c_{10} and c_{14} are elongated and lie on the diagonal of the parameter space, which leads to a large error on the upper limits on the coupling strengths under isoscalar-isovector interference due to numerical precision, but also the impact of isoscalar-isovector interference on the upper limits is especially large for these coupling´strengths as mentioned before. Changing to the neutron-proton basis the impact of the numerical precision is particularly relevant for c_1, c_5 and c_{11} under isoscalar-isovector interference, but sill at the same order of magnitude as for the most affected other coupling strengths in the isoscalar-isovector basis. Altogether the robustness of the upper limits under interference can become questionable, if the numerical precision is not high enough, and thus great care has to be taken when performing the calculations.

6.2 Upper limits on the coupling strengths for different annihilation cross sections

An equilibrium between DM capture and DM annihilation can not be assumed for the Earth. For that reason all upper limits on the coupling strengths and on the DM-nucleon cross sections depend on the annihilation cross section $< \sigma_A v >$, which has to be set to a certain value. In most publications and also in this work, up to this point, the thermal relic annihilation cross section $< \sigma_A v >_{\text{th}} = 3 \cdot 10^{-26} \text{cm}^3\text{s}^{-1}$ is chosen. As shown in chapter 4 several experiments set upper limits on the DM annihilation cross section at the 95 % confidence level, which are depicted in figure 4.4 for a combined analysis of MAGIC and Fermi-LAT observations of dwarf spheroidal galaxies. Depending on the DM mass these constraints are between $0.1 < \sigma_A v >_{\text{th}}$ for a DM mass of 10 GeV and $100 < \sigma_A v >_{\text{th}}$ for a DM mass of 10000 GeV. Nevertheless it is useful to investigate the impact of different annihilation cross sections on the upper limits on the coupling strengths for all examined DM masses, which is done in this section. Hereby the annihilation cross section is given as multiples of the thermal relic annihilation cross section.

The relation between the total DM annihilation rate Γ_A and the DM capture rate C is given by equation 3.4. In this equation the annihilation cross section $< \sigma_A v >$ enters via equation 3.3 for the equilibrium time τ in combination with equation 3.11 for the annihilation coefficient C_A. An equilibrium between DM capture and DM annihilation is reached, when $\tanh^2(t_\oplus/\tau) \approx 1$ in equation 3.4 and thus $\Gamma_A \approx \frac{1}{2}C$. As the annihilation coefficient C_A is proportional to $< \sigma_A v >$, the equilibrium is reached earlier for larger $< \sigma_A v >$-values, which corresponds to a shorter equilibrium time according to equation 3.3. The equilibrium between DM capture and DM annihilation is also dependent on the DM mass, which influences the equilibrium time on the one hand via the annihilation coefficient, which is proportional to $m_\chi^{3/2}$, and on the other hand via the DM capture rate, which depends on the DM mass according to equation 3.22. An upper bound on the DM capture rate for each investigated DM mass is set by the reported upper limits on the total DM annihilation rate. For these upper limits on the DM capture rate the corresponding equilibrium times for each DM mass can be calculated, which results in that sense in a lower bounds on the equilibrium time based on IceCube data, which are DM mass dependent. The reported total DM

annihilation rate decreases with increasing DM mass and is approximately proportional to m_χ^{-3} for DM masses up to $m_\chi = 1000$ GeV, from where the proportionality slowly shifts to $m_\chi^{-3/2}$, which then holds for DM masses above $m_\chi = 3000$ GeV. In case of DM capture - DM annihilation equilibrium these proportionalities also hold for the DM capture rate. Thus in case of equilibrium the lower limits on the equilibrium time, which correspond to the measured upper limits on the total DM annihilation rate, are proportional to $m_\chi^{3/4}$ up to $m_\chi = 1000$ GeV and almost constant starting at $m_\chi = 3000$ GeV. Consequently according to the IceCube measurements it holds: the larger the DM mass is, the later equilibrium is reached up to a DM mass of 3000 GeV, whereas for DM masses larger than 3000 GeV the equilibrium time is almost constant. In the Earth DM capture - DM annihilation equilibrium has not yet been attained, as mentioned before, and thus the exact values for the upper limits on the DM capture rate and their proportionality to the DM mass have to be calculated numerically, but in general similar trends for the different DM masses apply.

In order to investigate the impact of different annihilation cross sections on the upper limits on the coupling strengths, equation 5.9 has to be evaluated. The right side of the equation equals the upper limits from equation 5.14, which is applicable in case of DM capture - DM annihilation equilibrium, so that:

$$c_\alpha^{\max} \tanh\left(\frac{\kappa}{\sqrt{(\mathbb{C}^{-1})_{\alpha\alpha}}} c_\alpha^{\max}\right) = \sqrt{2(\mathbb{C}^{-1})_{\alpha\alpha}\Gamma_A^{\text{u.l.}}} = c_\alpha^{\max,\text{eq}} \,. \tag{6.1}$$

This equation can be further recast with $c_\alpha^{\max,\text{eq}} = \sqrt{2(\mathbb{C}^{-1})_{\alpha\alpha}\Gamma_A^{\text{u.l.}}}$ to the relation:

$$\frac{c_\alpha^{\max}}{c_\alpha^{\max,\text{eq}}} \tanh\left(\kappa\sqrt{2\Gamma_A^{\text{u.l.}}}\,\frac{c_\alpha^{\max}}{c_\alpha^{\max,\text{eq}}}\right) = 1 \,. \tag{6.2}$$

With this equation the relation between the upper limits on the coupling strengths for different annihilation cross sections $c_\alpha^{\max}$ and the upper limits on the coupling strengths assuming DM capture - DM annihilation equilibrium $c_\alpha^{\max,\text{eq}}$ can be calculated. The relation depends on the reported upper limits on the total DM annihilation rate by IceCube, which themselves depend on the DM mass as described above, and on κ, that depends on the DM mass and the annihilation cross section via the annihilation coefficient according to equation 5.3. As the relation of $c_\alpha^{\max}$ to its equilibrium value depends only on these parameters, the effect on the upper limits on the coupling strengths is the same for all interactions. It is only dependent on the DM mass, the annihilation cross section and the reported upper limits on the total annihilation rate. Using equation 5.3 for κ the argument of tanh in equation 6.2 contains: $t_\oplus\sqrt{2\Gamma_A^{\text{u.l.}}\cdot C_A} = t_\oplus/\tau^{eq}$, where τ^{eq} is the respective equilibrium time in case of DM capture - DM annihilation equilibrium. Thus the same dependencies on the DM mass and on the annihilation cross section apply for the relation $c_\alpha^{\max}$ to $c_\alpha^{\max,\text{eq}}$ as for the DM capture - DM annihilation equilibrium, which have been described before: The higher the annihilation cross section and the lower the DM mass are, starting at 3000 GeV, the more the upper limits on the coupling strengths equal to their values in the equilibrium case. For DM masses above 3000 GeV the influence of the DM mass is however negligible. Clearly approximately the same value for $c_\alpha^{\max}$ and $c_\alpha^{\max,\text{eq}}$ is obtained for $c_\alpha^{\max}/c_\alpha^{\max,\text{eq}} \approx 1$. As the tanh in equation 6.2 has to be approximately 1 for $c_\alpha^{\max}/c_\alpha^{\max,\text{eq}} \approx 1$ the argument of it, determined by $\kappa\sqrt{2\Gamma_A^{\text{u.l.}}}$, has to be so large, that the equation is fulfilled with high accuracy and thus also the values of the upper limits on the coupling strengths $c_\alpha^{\max}$ and $c_\alpha^{\max,\text{eq}}$ equal to each other with high accuracy. By increasing the annihilation cross section arbitrarily far the relation $c_\alpha^{\max}/c_\alpha^{\max,\text{eq}} \approx 1$ can be attained for any investigated DM mass. In table 6.1 the relation $c_\alpha^{\max}/c_\alpha^{\max,\text{eq}}$ is shown for the investigated DM masses and different annihilation cross sections, given as multiples of the thermal relic annihilation cross section.

$c_\alpha^{\max}/c_\alpha^{\max,\mathrm{eq}}$		$<\sigma_A v>$ as multiples of $<\sigma_A v>_{\mathrm{th}}$				
		10^0	10^1	10^2	10^3	10^4
m_χ [GeV]	10	1.28556	1.01138	1	1	1
	20	2.14615	1.32409	1.01686	1	1
	35	2.41195	1.45583	1.04476	1.00002	1
	50	2.53163	1.51690	1.06199	1.00006	1
	100	2.65271	1.57947	1.08197	1.00016	1
	250	4.52668	2.59242	1.54822	1.07172	1.00010
	500	5.55158	3.15952	1.84735	1.18649	1.00278
	1000	6.16082	3.49820	2.02982	1.26879	1.00939
	3000	6.62012	3.75404	2.16881	1.33506	1.01865
	5000	6.66237	3.77760	2.18165	1.34130	1.01971
	10000	6.54341	3.71129	2.14553	1.32379	1.01681

Table 6.1 The relation $c_\alpha^{\max}/c_\alpha^{\max,\mathrm{eq}}$ between the upper limits on the coupling strengths for different DM annihilation cross sections $c_\alpha^{\max}$ and the upper limits under DM capture - DM annihilation equilibrium $c_\alpha^{\max,\mathrm{eq}}$ is shown for the investigated DM masses and different annihilation cross sections, given as multiples of the thermal relic annihilation cross section.

The impact of the annihilation cross section on the upper limits on the coupling strengths c_i^τ assuming no interference as function of the DM mass is additionally visualized in figures 6.5, 6.6, 6.7 and 6.8. In these figures the upper limits are depicted for 5 different annihilation cross sections, starting at the thermal relic value in blue until the value, where the upper limits on the coupling strengths equal the value in case of DM capture - DM annihilation equilibrium $(C-\Gamma_A)_{\mathrm{eq}}$ in green. As seen in table 6.1 and in the figures an increasing $<\sigma_A v>$-value leads to lower upper limits on the coupling strengths, until they reach the value for DM capture - DM annihilation equilibrium. Up to a DM mass of 3000 GeV it holds: The higher the DM mass is, the stronger is the impact of the increasing $<\sigma_A v>$-value, as for higher DM masses the upper limits on the coupling strengths, assuming the thermal relic annihilation cross section, are further away from their equilibrium values. Or in other words: the upper limits on the coupling strengths for lower DM masses reach their equilibrium values for lower annihilation cross sections. For DM masses between 3000 GeV and 10000 GeV the effect of an increasing annihilation cross section remains approximately the same, independent of the investigated DM mass.

These effects are illustrated at some examples in the following. The $c_\alpha^{\max}$ value for a DM mass of $m_\chi = 50$ GeV and for an annihilation cross section of $<\sigma_A v> = 10^2 <\sigma_A v>_{\mathrm{th}}$ differs by 6.2% from the equilibrium value $c_\alpha^{\max,\mathrm{eq}}$, whereas e.g for a DM mass of $m_\chi = 250$ GeV the approximately same difference of 7.2% is obtained for an annihilation cross section of $<\sigma_A v> = 10^3 <\sigma_A v>_{\mathrm{th}}$. Assuming the thermal relic annihilation cross section as a starting point, the upper limits for a DM mass of 10 GeV are reduced at most by a factor of about 1.28, for a DM mass of 50 GeV by a factor of about 2.53 and for a DM mass of 10000 GeV by a factor of about 6.54. These factors are, as discussed before, the same for all upper limits on the coupling strengths, independent if they are isoscalar or isovector and which interaction is investigated. In some cases the change of the upper limits on the coupling strengths due to an increasing annihilation cross section is so large, that the DM mass with the lowest upper limit under the assumption of the thermal annihilation cross section, isn't any more the DM mass with the most stringent constraint, when the upper limits reach their equilibrium value. This is e.g. the case for c_4^τ and c_7^τ. As a remark: By choosing the annihilation cross section high enough DM capture - DM annihilation equilibrium can be attained for any investigated DM masses. In this case also equation 5.14 can be used to determine the upper limits on the coupling strengths, which reduces the numerical effort on computations.

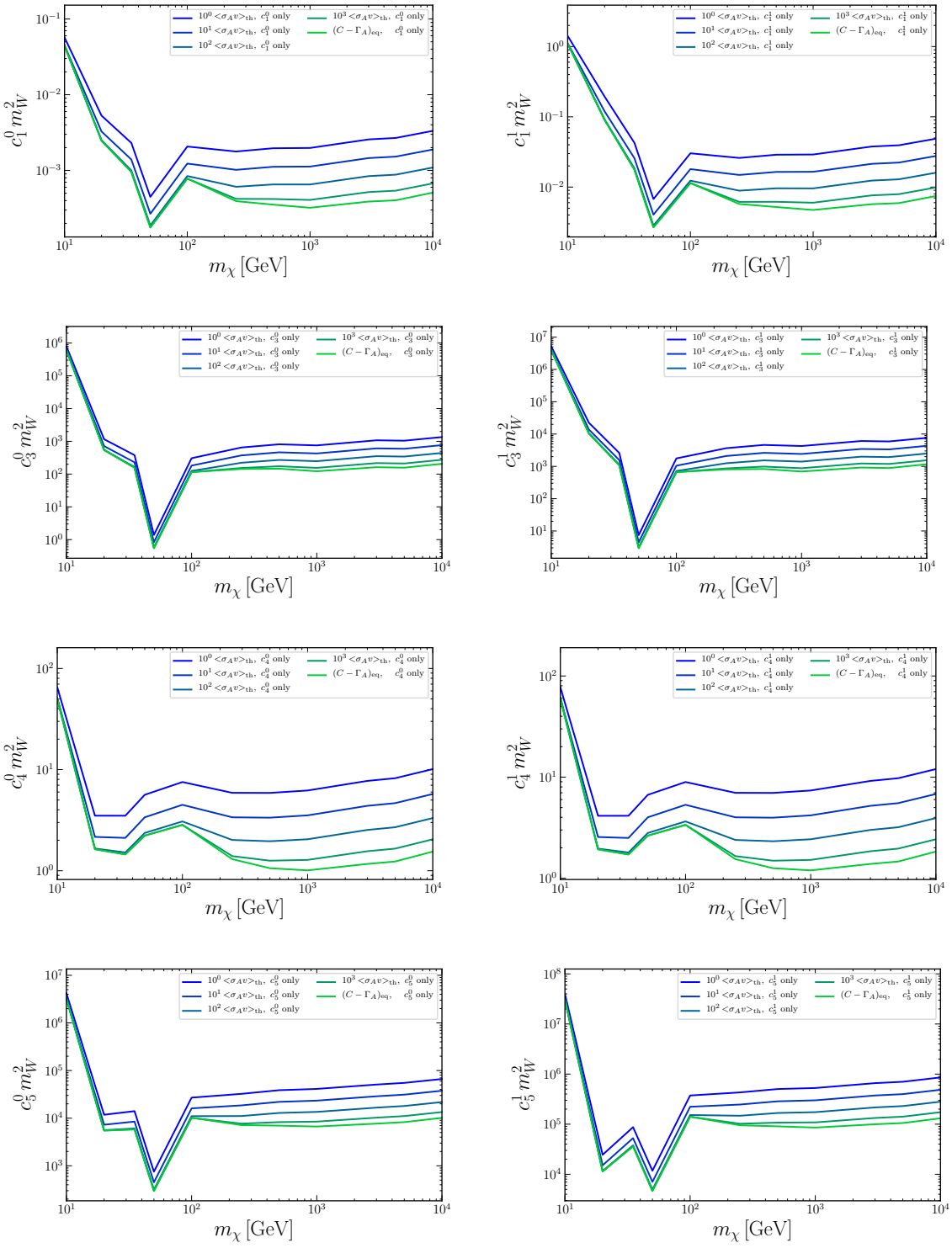

Figure 6.5 Upper limits on the coupling strengths c_i^τ, $i = 1, 3, 4, 5$, $\tau = 0, 1$ assuming no interference at the 90 % confidence level for increasing values of the annihilation cross-section, given as multiples of the thermal relic annihilation cross section $< \sigma_A v >_{\rm th} = 3 \cdot 10^{-26} {\rm cm}^3 {\rm s}^{-1}$ in blue, up to the point, where the upper limits reach the value in case of DM capture - DM annihilation equilibrium $(C - \Gamma_A)_{\rm eq}$ in green. The isoscalar coupling strengths c_i^0 are on the left side and the isovector coupling strengths c_i^1 on the right sight for each interaction $i = 1, 3, 4, 5$.

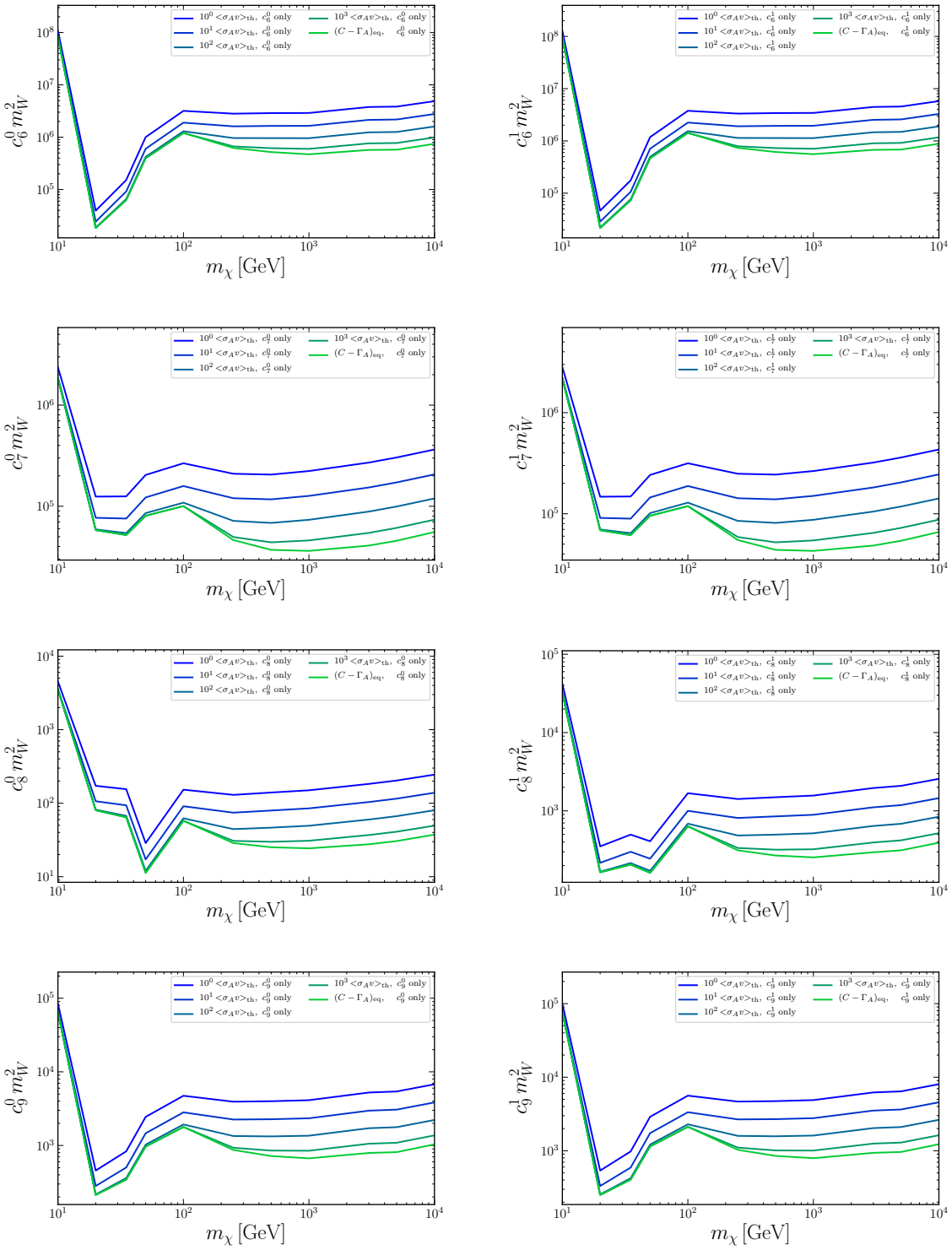

Figure 6.6 Same as figure 6.5 for coupling strengths $c_i^\tau,\ i = 6, ..., 9$.

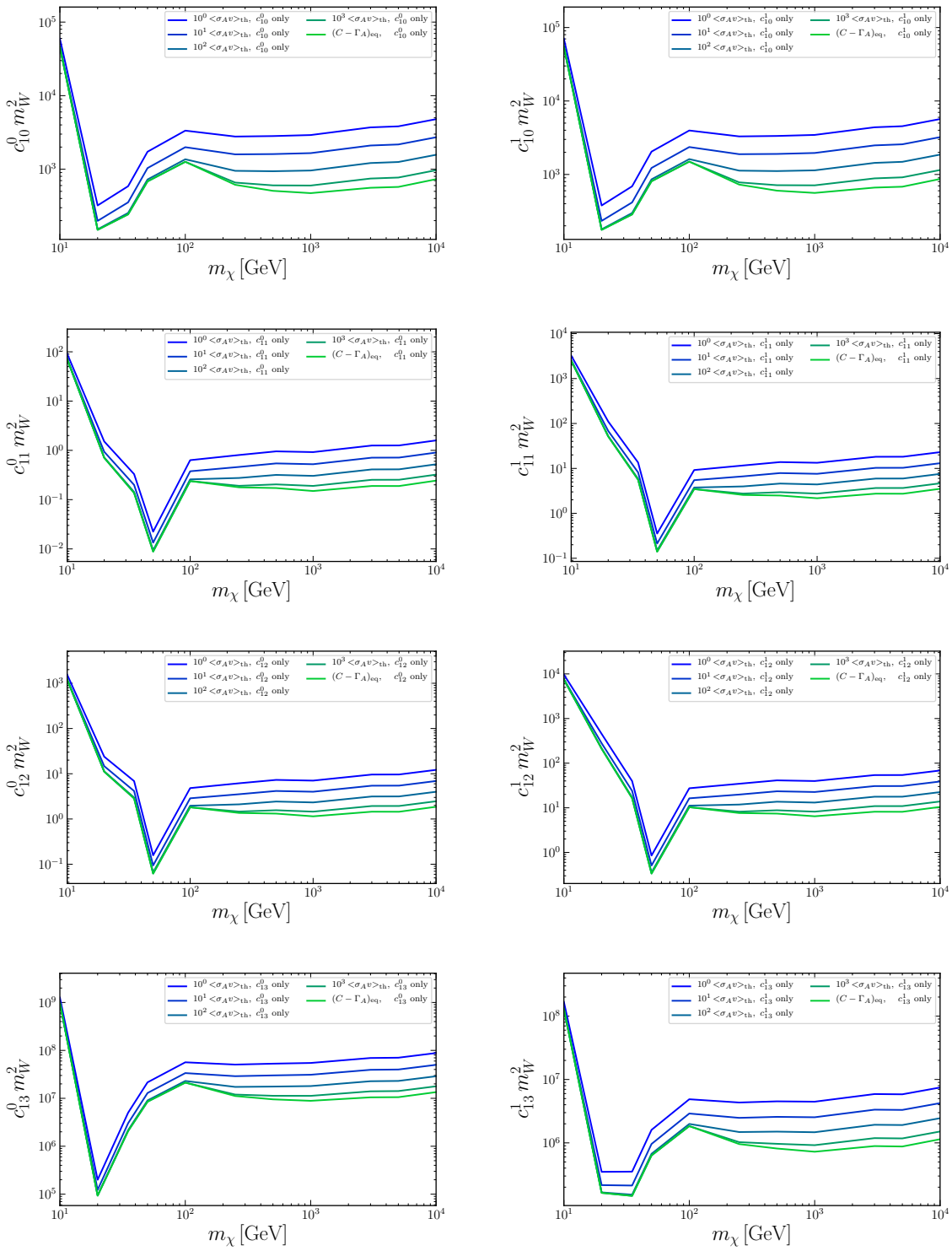

Figure 6.7 Same as figure 6.5 for coupling strengths c_i^τ, $i = 10, ...13$.

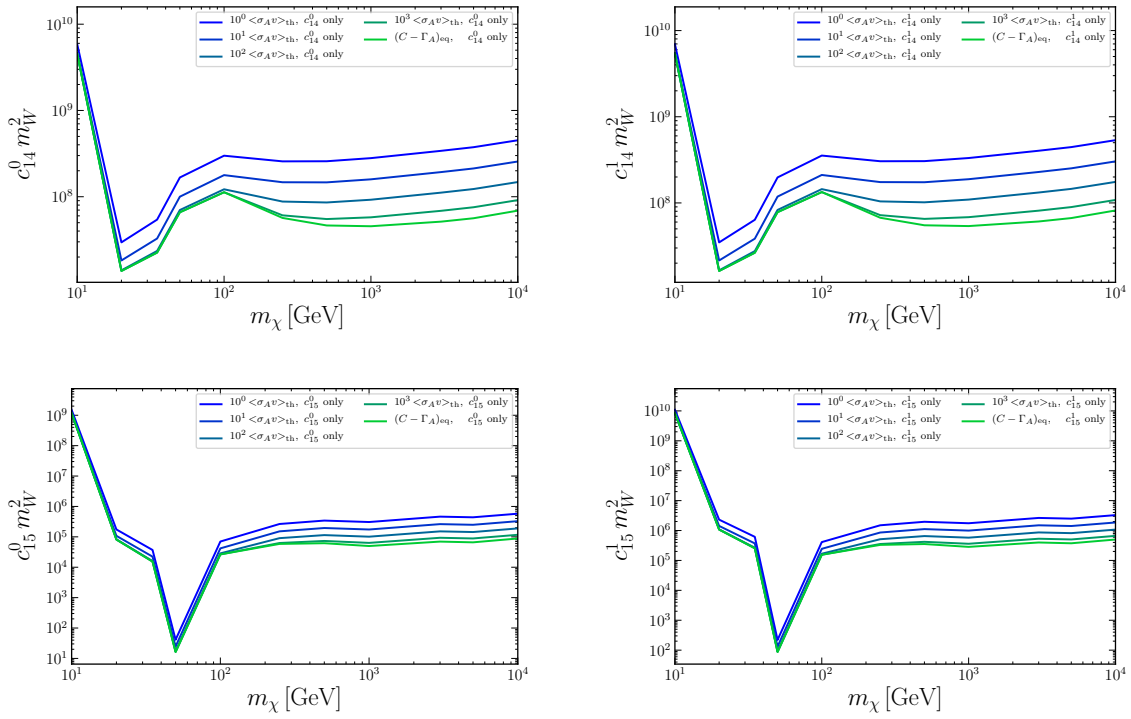

Figure 6.8 Same as figure 6.5 for coupling strengths $c_i^\tau,\ i = 14, 15$.

The constraints on the coupling strengths under interference for different annihilation cross sections are shown as addition in appendix D, where the same effects as described above can be observed. The independence of the factors from the interaction or respective coupling strength also applies in case of a basis change. However, when constraining the DM-nucleon cross-sections, the factors are subject to equation 5.22 and have to be squared, as the coupling strengths themselves are squared in this equation. Thus the factors, describing the relation $\sigma_{\chi\mathcal{N}}^{\text{max}}/\sigma_{\chi\mathcal{N}}^{\text{max,eq}}$ between the upper limits on the DM-nucleon cross section for different DM annihilation cross sections $\sigma_{\chi\mathcal{N}}^{\text{max}}$ and the upper limits under DM capture - DM annihilation equilibrium $\sigma_{\chi\mathcal{N}}^{\text{max,eq}}$, change to the values depicted in table 6.2. But as both coupling strengths and factors are computed by the equations for the DM-nucleon cross-sections the effects of the changing annihilation cross section for the different DM masses remain the same.

The upper limits on the DM-nucleon cross sections, which are based on the coupling strengths $c_1^{\mathcal{N}}$ and $c_4^{\mathcal{N}}$ in the neutron-proton base, are depicted in figure 6.9. In the upper row are the upper limits on the spin-independent DM-nucleon cross section and in the lower row on the spin-dependent DM-nucleon cross section. On the left side are the upper limits on the DM-neutron cross sections and on the right side the upper limits on the DM-proton cross sections. Hereby the solid lines show the upper limits on the DM-nucleon cross sections assuming that the only non-zero coupling strength is the isoscalar component c_1^0 for the spin-independent and the isoscalar component c_4^0 for the spin-dependent DM-nucleon cross section. The dashed lines show the results assuming that both c_1^0 and c_1^1 for the spin-independent DM-nucleon cross section and c_4^0 and c_4^1 for the spin-dependent DM-nucleon cross section can be non-zero and interfere, whereas all other coupling strengths vanish. The dotted lines show the upper limits on the DM-nucleon cross sections under the assumption, that all coupling strengths can be non-zero and interfere. In any case the upper limits are depicted for 4 different annihilation cross sections, starting at the thermal relic value, which is depicted in cyan, until the value, where DM capture - DM annihilation equilibrium is reached, which is shown in green. As seen here the same effects occur for changing annihilation cross sections as in the isoscalar-isovector basis and the DM-nucleon cross sections are reduced for increasing values of the annihilation cross section by the factors depicted in table 6.2.

$\sigma^{\text{max}}_{\chi\mathcal{N}}/\sigma^{\text{max,eq}}_{\chi\mathcal{N}}$		$<\sigma_A v>$ as multiples of $<\sigma_A v>_{\text{th}}$				
		10^0	10^1	10^2	10^3	10^4
m_χ [GeV]	10	1.65266	1.02289	1	1	1
	20	4.60595	1.75321	1.03400	1	1
	35	5.81749	2.11945	1.09151	1.00004	1
	50	6.40917	2.30098	1.12782	1.00012	1
	100	7.03688	2.49474	1.17067	1.00031	1
	250	20.4908	6.72066	2.39700	1.14859	1.00020
	500	30.8200	9.98255	3.41272	1.40777	1.00557
	1000	37.9557	12.2374	4.12017	1.60984	1.01886
	3000	43.8260	14.0928	4.70374	1.78238	1.03764
	5000	44.3872	14.2702	4.75958	1.79908	1.03981
	10000	42.8162	13.7736	4.60329	1.75242	1.03391

Table 6.2 The relation $\sigma^{\text{max}}_{\chi\mathcal{N}}/\sigma^{\text{max,eq}}_{\chi\mathcal{N}}$ between the upper limits on the DM-nucleon cross section for different DM annihilation cross sections $\sigma^{\text{max}}_{\chi\mathcal{N}}$ and the upper limits under DM capture - DM annihilation equilibrium $\sigma^{\text{max,eq}}_{\chi\mathcal{N}}$ is shown for different annihilation cross sections and the investigated DM masses.

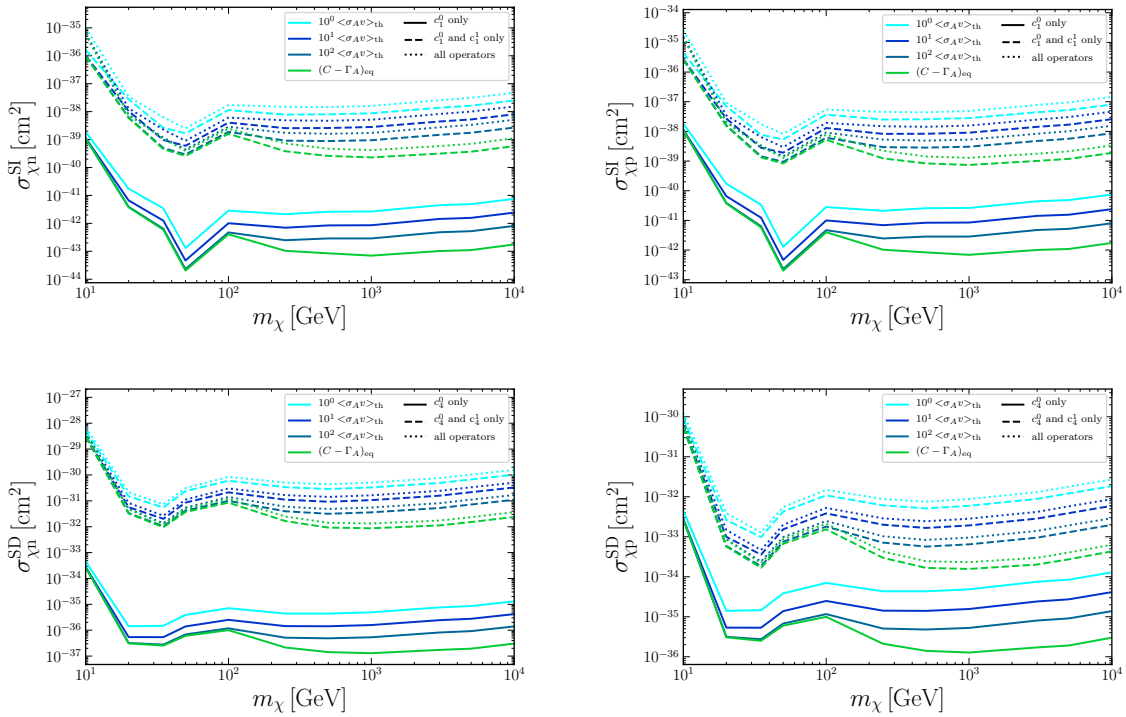

Figure 6.9 Upper limits on the spin-independent DM-nucleon cross section on top and the spin-dependent DM-nucleon cross section at the bottom at the 90% confidence level for increasing values of the annihilation cross-section, given as multiples of the thermal relic annihilation cross section $<\sigma_A v>_{\text{th}} = 3 \cdot 10^{-26}\text{cm}^3\text{s}^{-1}$ in cyan, up to the point, where the upper limits reach the value in case of DM capture - DM annihilation equilibrium $(C-\Gamma_A)_{\text{eq}}$, in green. Results for the DM-neutron cross sections are on the left and for the DM-proton cross sections on the right. Solid lines represent the results considering no interference, i.e. c_1^0 is the only non-zero coupling strength for the spin-independent cross section and c_4^0 the only one for the spin-dependent cross section. The dashed lines show the results considering interference between the isoscalar and isovector interactions, i.e. c_1^0 and c_1^1 can be non-zero and interfere for the spin-independent cross section and c_4^0 and c_4^1 for the spin-dependent cross section. The dotted lines show the results considering interference between all interactions of the effective theory.

6.3 Comparison of results with other experiments

Many DM detection experiments search for DM interactions with nuclei. By applying the method and formulae of chapter 5 to the null search results of these experiments, rigorous model independent upper limits on the coupling strengths of the non-relativistic effective theory of DM-nucleon interactions can be set and thus the results of the different experiments can be compared. In this section the upper limits on the coupling strengths of this work, derived by the non-observation of an exotic neutrino flux from the Earth's center, are compared to the results of three other experiments. The first one is also conducted by the IceCube collaboration. Besides the indirect DM search in the Earth IceCube conducts an indirect DM search in the direction of the Sun, in which the equilibrium between DM capture and DM annihilation has already been attained [36]. Upper limits on the coupling strengths resulting from the non-observation of a neutrino flux excess in this search, have been derived in [16]. The two other experiments are direct detection searches, namely XENON1T [29] and PICO-60 [27] [28]. XENON1T uses xenon as target material and PICO-60 initially CF_3I and then C_3F_8. For both experiments the upper limits on the coupling strengths are derived from the non-observation of a significant excess in the number of nuclear recoil events. These constraints can be calculated by using an analogous form of the equations of chapter 5. Details about this formalism are presented in [15]. In figures 6.10, 6.11, 6.12 and 6.13 the upper limits on the coupling strengths c_i^τ for $i = 1, 3, ..., 15$ and $\tau = 0, 1$ are depicted at the 90 % confidence level as function of the DM mass from the non-observation of a signal at XENON1T in brown, at PICO-60 in magenta, at IceCube in direction of the Sun in yellow (called IC Sun) and at IceCube in direction of the Earth's center in blue (called IC Earth). For both IceCube experiments the thermal relic annihilation cross section and DM annihilation into W^+W^- for DM masses larger than the rest mass of the W boson and DM annihilation into $\tau^+\tau^-$ for lower DM masses are assumed. The solid lines show the results under the assumption, that the depicted coupling strength describes the only non-zero interaction, which means that there exists no interference. The results considering an isoscalar-isovector interference are depicted as dashed lines. So in this case c_i^0 and c_i^1 can be non-zero and interfere, while all other coupling strengths vanish. The dotted lines show the results, when all coupling strengths are non-zero and interference between all operators occurs.

As seen in the figures for most interactions the most stringent upper limits on the coupling strengths assuming no interference are obtained from XENON1T. However for DM masses between about 300 GeV and 2500 GeV IC Sun gives stronger constraints on c_4^τ, c_6^0, c_7^τ and c_{14}^0 than XENON1T. In addition the upper limits on c_4^τ and c_7^τ for DM masses lower than about 20 GeV are the most constrained by PICO-60, whereby the lower the mass is, the more constraining PICO-60 gets compared to XENON1T. This holds for all interactions, so that the upper limits on c_9^τ, c_{10}^τ and c_{14}^τ from PICO-60 and XENON1T become almost the same for a DM mass of 10 GeV. Upper limits on the coupling strengths assuming no interference from IC Earth are especially strong for a DM mass of about 50 GeV, which is based on the resonant capture of DM due to the high abundance of ^{56}Fe in the Earth's core. At this DM mass the upper limits on c_1^τ, c_3^τ, c_{11}^τ, c_{12}^τ and c_{15}^τ obtained from IC Earth are more stringent than the ones from IC Sun and PICO-60 or at least at the same order of magnitude. Also for high DM masses of about 10000 GeV the IC Earth upper limits on the coupling strength c_1^τ are comparable to the upper limits from IC Sun and PICO-60. But they are always weaker than the XENON1T constraints on all coupling strengths.

The impact of interference between the isoscalar and isovector interaction on the upper limits on the coupling strengths is significant for many interactions, so that the constraints are clearly relaxed compared to the upper limits under the assumption of no interference. For the upper limits from XENON1T and PICO-60 the impact of isoscalar-isovector interference is especially relevant for c_4^τ, c_6^τ, c_7^τ, c_9^τ, c_{10}^τ, c_{13}^τ and c_{14}^τ, where the constraints are relaxed by about 2 orders of magnitude for XENON1T and 4 orders of magnitude for PICO-60. For these coupling strengths the constraints under isoscalar-isovector interference from IC Earth are relaxed by about 2 orders of magnitude, besides in the case of c_{13}^τ, where the impact on the upper limits is relatively small for IC Earth. The upper limits on the coupling strengths assuming isoscalar-isovector interference from IC Sun are however not as much affected by the impact of

the interference as the results from the other experiments. For that reason the most stringent upper limits under isoscalar-isovector interference on c_4^τ, c_6^τ, c_7^τ, c_9^τ, c_{10}^τ and c_{14}^τ for DM masses of 20 GeV to 10000 GeV and on c_{13}^τ for DM masses of 100 GeV to 10000 GeV are obtained from IceCube Sun. AS a remark: IC Sun does not provide upper limits for DM masses below 20 GeV in contrast to the other experiments.

For some coupling strengths the upper limits under interference between all operators are more relaxed than the constraints under isoscalar-isovector interference. As described in section 6.1 the impact of interference between all operators on the constraints is determined by the DM response functions, defined in appendix B, and differs for each coupling strength. The upper limits under interference between all operators are especially strong relaxed compared to the results under isoscalar-isovector interference for PICO-60 in case of c_4^τ, c_{11}^τ and c_{12}^τ, namely by about 2 orders of magnitude. Thus the upper limits assuming interference between all operators from PICO-60 become weaker than the constraints under all operator interference from IC Earth for these coupling strengths. Also the constraints on some coupling strengths from XENON1T become more relaxed assuming all operator interference. Thus the most stringent upper limits on c_1^0, c_{11}^0, c_{12}^0 and c_{15}^0 under interference between all operators for DM masses of about 300 GeV to 3000 GeV are given by IC Sun, in addition to the most stringent upper limits already obtained under isoscalar-isovector interference.

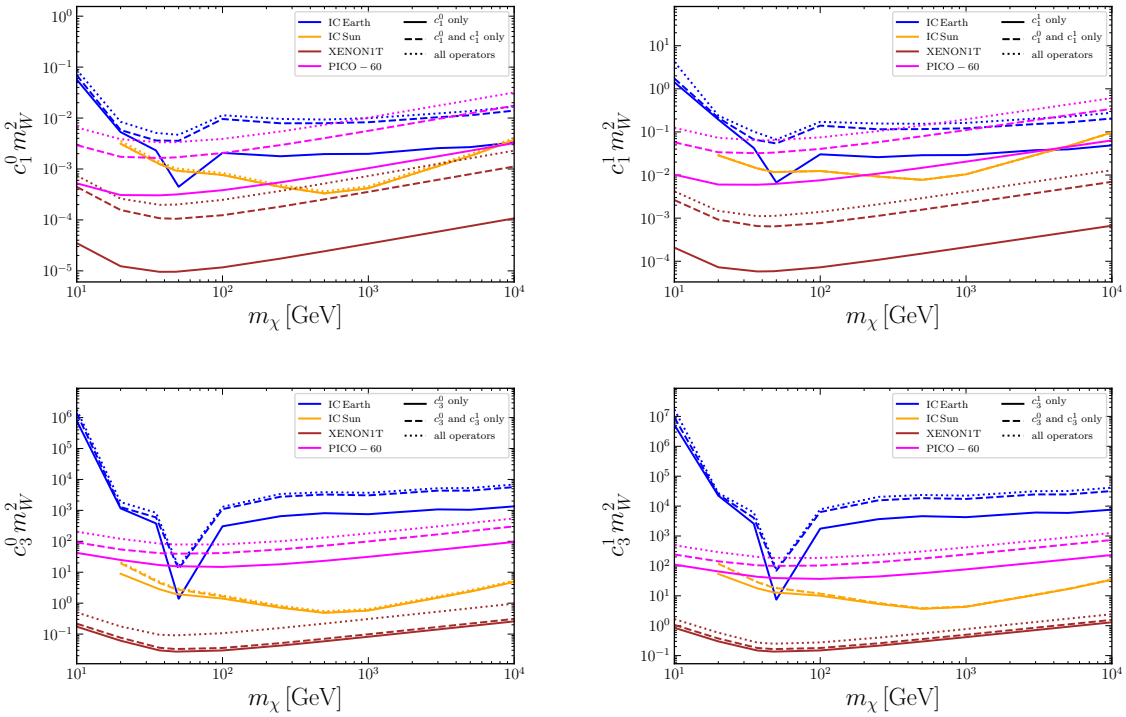

Figure 6.10 Upper limits on the coupling strengths c_i^τ, $i = 1, 3$, $\tau = 0, 1$ at the 90 % confidence level as function of the DM mass from the non-observation of a signal at XENON1T in brown, at PICO-60 in magenta, at IceCube in direction of the Sun in yellow (called IC Sun) and at IceCube in direction of the Earth's center in blue (called IC Earth). The thermal relic annihilation cross section and DM annihilation into W^+W^- for masses larger than the rest mass of the W boson and DM annihilation into $\tau^+\tau^-$ for lower DM masses are assumed for both IceCube experiments. The solid lines show the results without interference. The dashed lines show the results considering an isoscalar-isovector interference and the dotted lines show the results, when all coupling strengths are non-zero and interference between all operators occurs. The isoscalar strengths c_i^0 are depicted on the left side and the isovector strengths c_i^1 on the right sight.

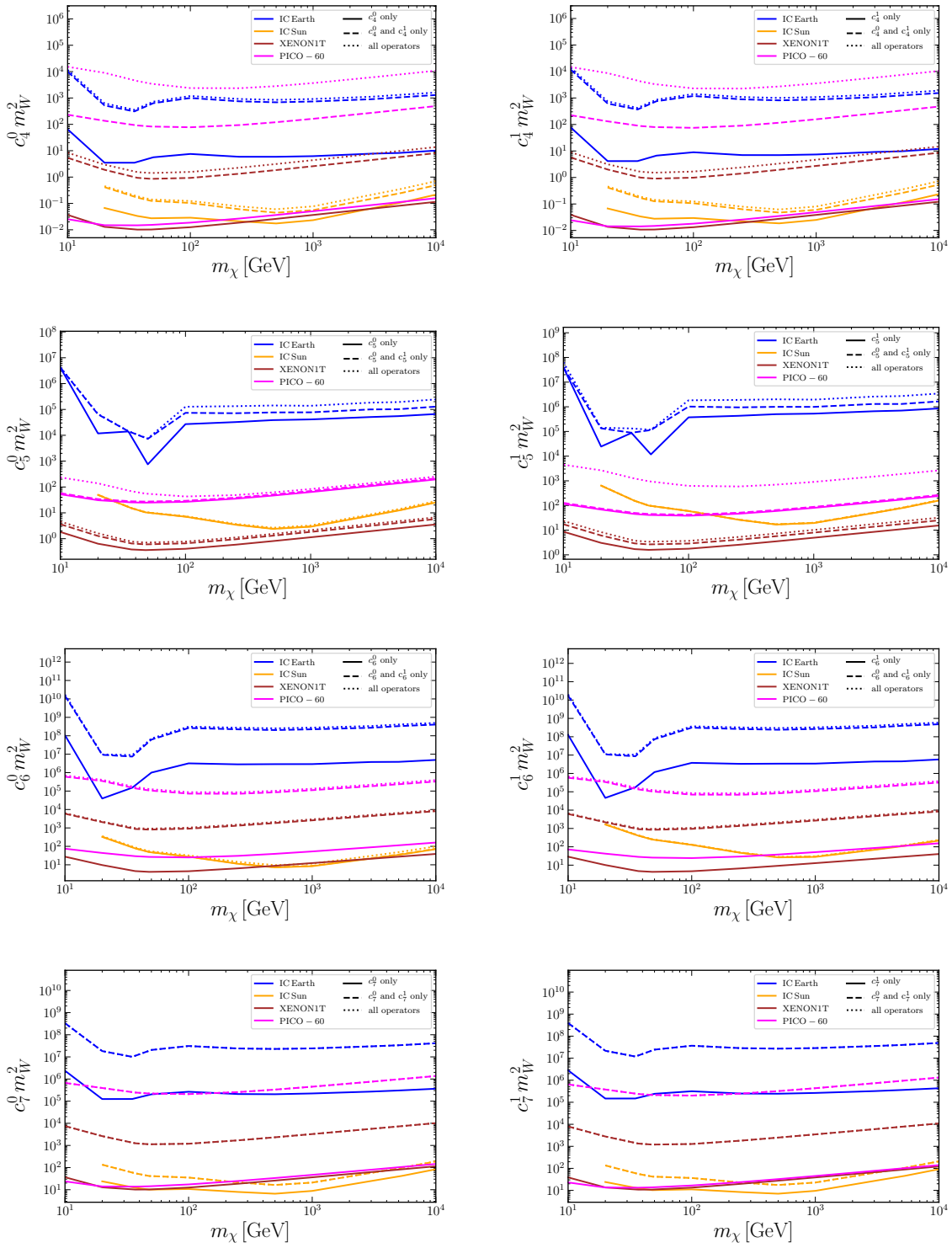

Figure 6.11 Same as figure 6.10 for coupling strengths c_i^τ, $i = 4, ..., 7$.

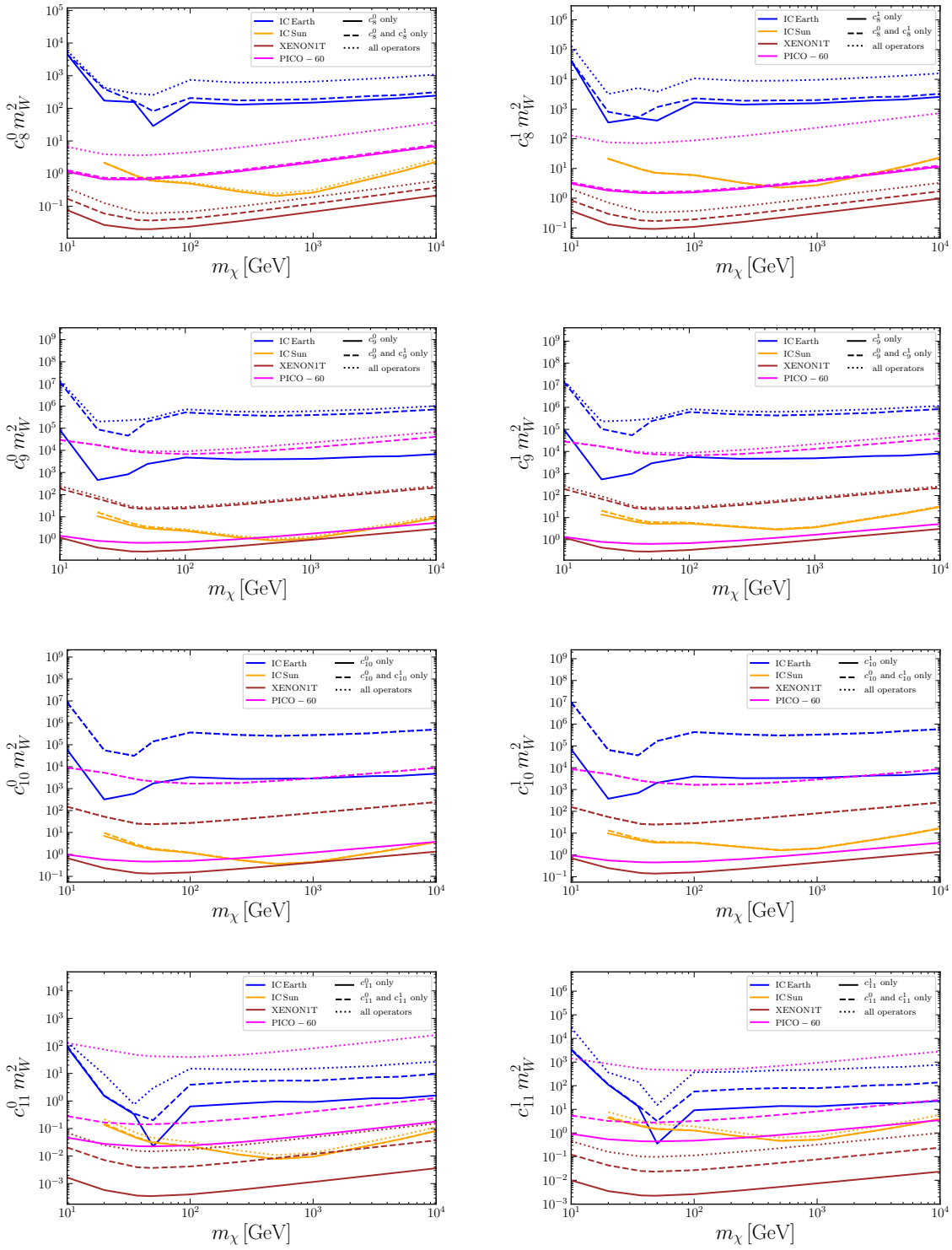

Figure 6.12 Same as figure 6.10 for coupling strengths c_i^τ, $i = 8, ..., 11$.

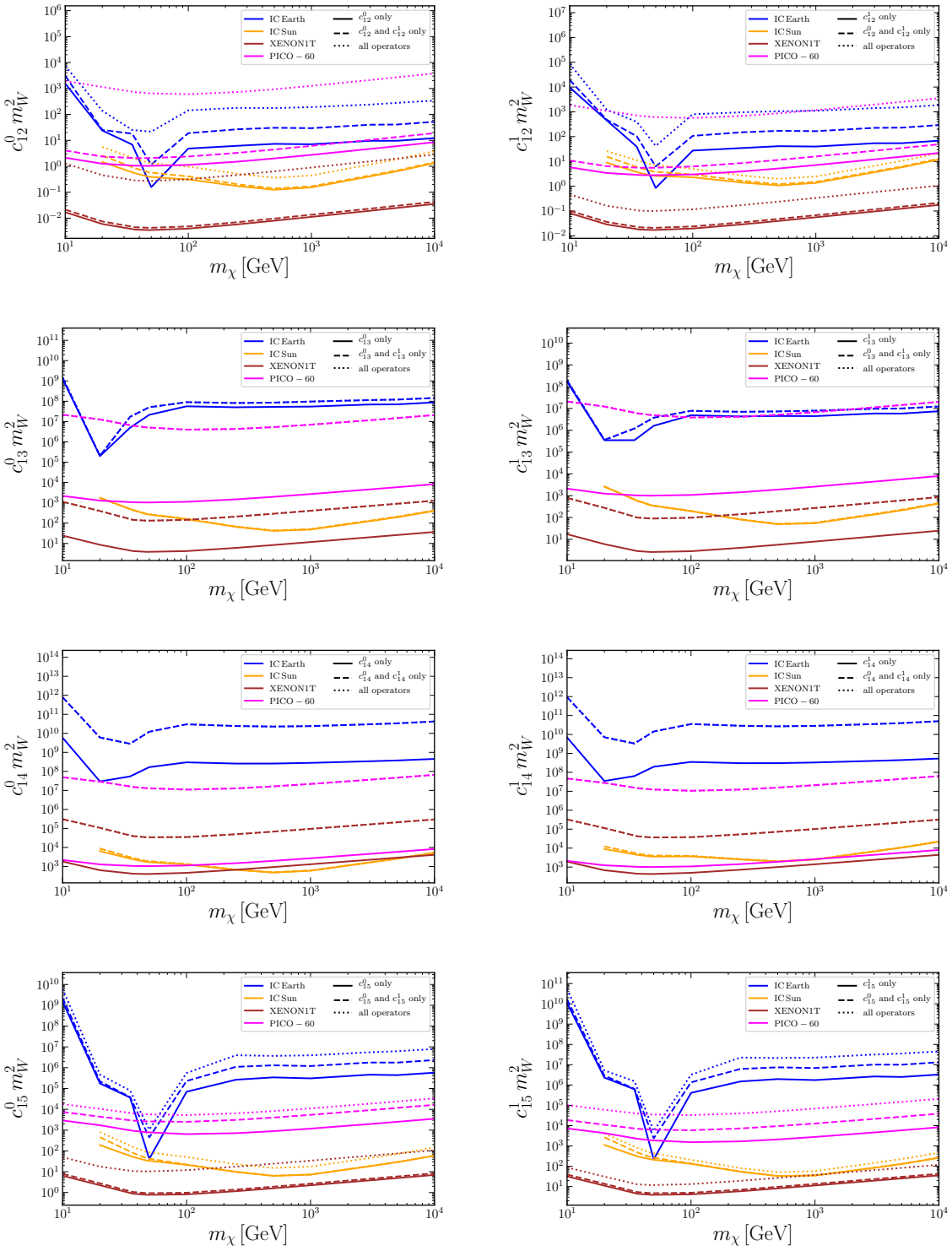

Figure 6.13 Same as figure 6.10 for coupling strengths c_i^τ, $i = 12, ..., 15$.

The effect of isoscalar-isovector interference on the upper limits on the coupling strengths can be illustrated by plotting the allowed regions at the 90 % confidence level in the c_i^0 - c_i^1 parameter space, which is done in figure 6.14 for XENON1T in brown, PICO-60 in magenta, IC Sun in yellow and IC Earth in blue for the thermal relic annihilation cross section $< \sigma_A v >_{\text{th}} = 3 \cdot 10^{-26} \text{cm}^3\text{s}^{-1}$. In addition the allowed regions from IC Earth are also depicted for $10 \cdot < \sigma_A v >_{\text{th}}$ in teal and for an annihilation cross section, where DM capture - DM annihilation equilibrium $(C - \Gamma_A)_{\text{eq}}$ is attained, in green. The ellipses are drawn for a DM mass of 50 GeV, as for most interactions the most stringent upper limits from IC Earth are obtained at this DM mass. As a remark it is mentioned, that the allowed regions from XENON1T do not include the point $c_i^0 = c_i^1 = 0$ because of the large number of signal events, observed by XENON1T compared to the background. This may be interpreted as a hint for DM, which is however not part of this work, where the focus lies on the derivation of rigorous upper limits on the coupling strengths, and can thus also not be seen in the allowed regions. As described in section 6.1 the orientation and elongation of the ellipses in the parameter space determine the impact of the isoscalar-isovector interference on the constraints on the coupling strengths. The more the ellipses are elongated and misaligned with the c_i^0 - c_i^1 axes the stronger is the impact, but also the stronger is the relative error on the constraints.

The plots of all interactions are zoomed in to the center, where the smallest allowed regions are. In most cases the bounds on the allowed region of one experiment are outside the zoomed-in area, so that it appears only in the background of the allowed regions of the other experiments, like for IC Sun at $\mathcal{O}_1$. If the three allowed regions from IC Earth, resulting from the different annihilation cross sections, are outside this zoomed-in area, a light blue background is displayed, as e.g. at $\mathcal{O}_4$. For the operators $\mathcal{O}_1$, $\mathcal{O}_3$, $\mathcal{O}_5$, $\mathcal{O}_8$, $\mathcal{O}_{11}$, $\mathcal{O}_{12}$, $\mathcal{O}_{13}$ and $\mathcal{O}_{15}$ the allowed region from XENON1T lies completely within the allowed regions from the other experiments. This is also the case, if one plots the allowed regions for all other DM masses of 10 Gev - 10000 GeV, besides in case of $\mathcal{O}_{13}$, where the allowed regions from IC Sun and XENON1T intersect starting at about 100 GeV up to 10000 GeV. For the here depicted DM mass of 50 GeV an intersection of the allowed regions from the different experiments occurs for the operators $\mathcal{O}_4$, $\mathcal{O}_6$, $\mathcal{O}_7$, $\mathcal{O}_9$, $\mathcal{O}_{10}$ and $\mathcal{O}_{14}$. As seen for these interactions different experiments can not only be compared, instead the allowed regions from the different experiments can be combined, in order to put more stringent constraints on the upper limits, as allowed points must lie inside the intersection of the allowed regions from all experiments. In principle the combined allowed region is almost simply the intersection of the allowed regions from all experiments, but points close to the boundary of the intersection region may be excluded by more than 90 % confidence level, when combining the results of the experiments. A method to derive rigorous model independent upper limits on the coupling strengths from combining several experiments has been introduced in [15], but goes beyond the scope of this work. As the combined allowed regions are however similar to the pure intersection, qualitative conclusions can be made for the upper limits without interference and under isoscalar-isovector interference, though no exact results can be presented. The upper limits in case of no interference are obtained by projecting the vertex and co-vertex of the ellipses on the $c_i^0 - c_i^1$ axes. These upper limits are determined by the result of the most constraining experiment. Thus a combination of experiments will not improve these limits significantly. In case of isoscalar-isovector interference the allowed region can be stronger constrained by the combination of experiments. This is most notably, when the allowed regions of the experiments are orthogonal to each other in the parameter space as for $\mathcal{O}_4$, $\mathcal{O}_6$, $\mathcal{O}_7$, $\mathcal{O}_9$, $\mathcal{O}_{10}$, $\mathcal{O}_{13}$ and $\mathcal{O}_{14}$. For these interactions the differential cross section from equation 3.16 is driven by the spin-dependent nuclear response functions $W_{\Sigma'}^{\tau\tau'}$ or $W_{\Sigma''}^{\tau\tau'}$ from appendix C. The complementarity between XENON1T, PICO-60 and IC Sun for these interactions is based on the fact, that xenon has one unpaired neutron, while fluorine and hydrogen have one unpaired proton. For the other operators $\mathcal{O}_1$, $\mathcal{O}_3$, $\mathcal{O}_5$, $\mathcal{O}_8$, $\mathcal{O}_{11}$, $\mathcal{O}_{12}$ and $\mathcal{O}_{15}$ the differential cross section is driven by the nuclear response functions $W_M^{\tau\tau'}$ or $W_{\Phi''}^{\tau\tau'}$, that have a large hierarchy between xenon and the elements of the other experiments. For that reason the allowed region from XENON1T lies within the allowed regions from the other experiments for these operators.

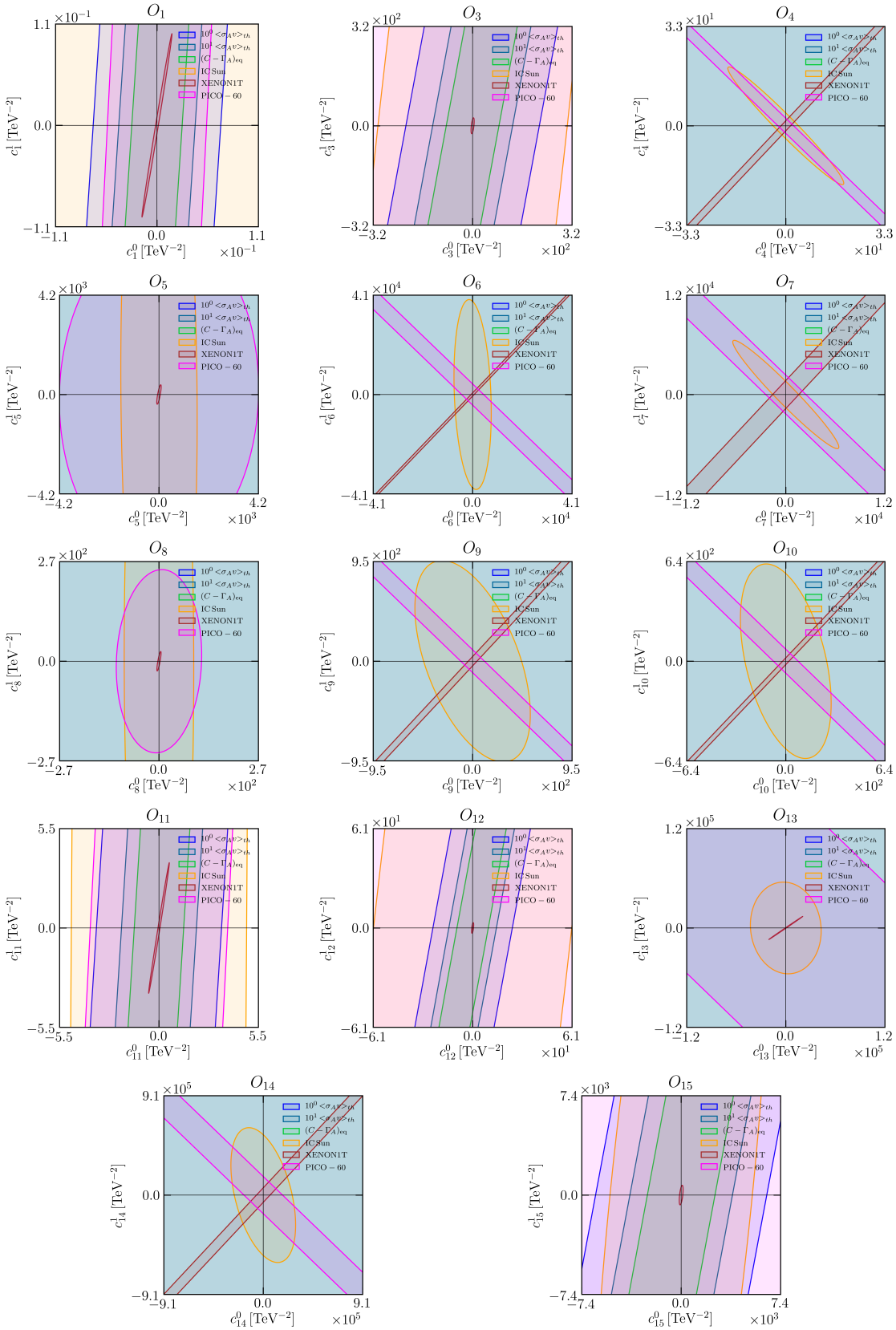

Figure 6.14 Allowed regions at the 90 % confidence level in the $c_i^0 - c_i^1$ parameter space from XENON1T in brown, PICO-60 in magenta, IC Sun in yellow and IC Earth for the thermal relic annihilation cross section $< \sigma_A v >_{\text{th}} = 3 \cdot 10^{-26} \text{cm}^3\text{s}^{-1}$ in blue, for $10 \; < \sigma_A v >_{\text{th}}$ in teal and for an annihilation cross section, where DM capture - DM annihilation equilibrium $(C - \Gamma_A)_{\text{eq}}$ is attaiend, in green, for a DM mass of 50 GeV.

The allowed regions are plotted for a DM mass of 50 GeV, as the upper limits from IC Earth are especially strong at this DM mass due to the high abundance of ^{56}Fe in the Earth's core, as mentioned before. The nuclear response functions $W_M^{\tau\tau'}$ or $W_{\Phi''}^{\tau\tau'}$ of ^{56}Fe drive the differential cross section at this DM mass for the operators $\mathcal{O}_1$, $\mathcal{O}_3$, $\mathcal{O}_5$, $\mathcal{O}_8$, $\mathcal{O}_{11}$, $\mathcal{O}_{12}$ and $\mathcal{O}_{15}$. For $\mathcal{O}_3$, $\mathcal{O}_{11}$ and $\mathcal{O}_{12}$ the allowed regions from IC Earth are smaller than the allowed regions from PICO-60 and IC SUN at this DM mass assuming the thermal relic annihilation cross section. Additionally under the assumption of an annihilation cross section of $10 \ < \sigma_A v >_{\text{th}}$ the allowed regions for $\mathcal{O}_1$ and $\mathcal{O}_{15}$ from IC Earth are smaller than the allowed regions from PICO-60 and IC Sun. But all allowed regions for the operators $\mathcal{O}_1$, $\mathcal{O}_3$, $\mathcal{O}_5$, $\mathcal{O}_8$, $\mathcal{O}_{11}$, $\mathcal{O}_{12}$ and $\mathcal{O}_{15}$ are, even for an annihilation cross section, where DM capture - DM annihilation equilibrium is attained, larger than the allowed regions from XENON1T due to the hierarchy of $W_M^{\tau\tau'}$ and $W_{\Phi''}^{\tau\tau'}$ between xenon and the other elements. The allowed regions for the operators $\mathcal{O}_4$, $\mathcal{O}_6$, $\mathcal{O}_7$, $\mathcal{O}_9$, $\mathcal{O}_{10}$, $\mathcal{O}_{13}$ and $\mathcal{O}_{14}$ from IC Earth are larger than the allowed regions for these operators from the other experiments, as in the used Earth model only ^{23}Na, ^{27}Al and ^{31}P, whose abundances are low in the Earth, possess the spin-dependent nuclear response functions $W_{\Sigma'}^{\tau\tau'}$ or $W_{\Sigma''}^{\tau\tau'}$. As a remark: Several elements with low abundances in the Earth, like e.g. hydrogen, which also possesses the nuclear response functions $W_{\Sigma'}^{\tau\tau'}$ and $W_{\Sigma''}^{\tau\tau'}$, are not part of the used Earth model PREM (see appendix A) and could potentially have an impact on the allowed regions especially for the respective operators, but in general their influence on the upper limits should be small compared to the elements with higher abundances. The impact of interference is dependent on the chosen basis. But as a basis change is basically a rotation in the parameter space the relative orientation of the allowed regions to each other remains the same. Thus the statements above hold also when changing for example to the neutron-proton basis.

For higher DM masses the upper limits from IC Earth are weaker than for a DM mass of 50 GeV, but the impact of the equilibrium time and thus of the chosen annihilation cross section on the upper limits becomes stronger with higher DM masses according to table 6.1. For that reason the upper limits on the coupling strengths $c_i^\tau,\ i = 1, 3,\ \tau = 0, 1$ from IC Earth at the 90 % confidence level assuming no interference for increasing values of the annihilation cross-section, starting at the thermal relic annihilation cross section $< \sigma_A v >_{\text{th}} = 3 \cdot 10^{-26}\text{cm}^3\text{s}^{-1}$ in blue, up to the point, where the upper limits reach the values in case of DM capture - DM annihilation equilibrium $(C - \Gamma_A)_{\text{eq}}$ in green, are compared to the upper limits of the other experiments in figures 6.15, 6.16, 6.17 and 6.18, where XENON1T is depicted in brown, PICO-60 in magenta and IC Sun in yellow. The impact of the increasing annihilation cross section on the coupling strengths from IC Earth is described in the following. For the operator $\mathcal{O}_1$ the upper limits are under the assumption of the thermal relic annihilation cross section for a DM mass of about 10000 GeV already comparable to the upper limits from IC Sun and PICO-60 as mentioned before. Assuming DM capture - DM annihilation equilibrium the upper limits on c_1^0 are more stringent or at least comparable to the upper limits from IC Sun for all investigated DM masses and the constraints on c_1^1 for all DM masses higher than 35 GeV. The upper limits on c_1^0 and c_1^1 are under the assumption of equilibrium also more stringent than the upper limits from PICO-60 for a DM mass of about 50 GeV and starting from a DM mass of about 200 GeV until 10000 GeV. The assumption of DM capture - DM annihilation equilibrium leads also for other interactions to comparable upper limits to other experiments. Assuming equilibrium, the upper limits on c_{11}^0 become comparable to the upper limits from PICO-60 for a DM mass of 10000 GeV and the upper limits on c_{11}^1 to the upper limits from PICO-60 and IC Sun. Also the upper limits on the coupling strengths c_{12}^0 and c_{12}^1 are shifted for higher DM masses under the assumption of equilibrium down to values comparable to IC Sun and PICO 60. For c_{12}^0 the upper limits under the equilibrium assumption are more stringent than the ones from PICO-60 starting at a DM mass of 300 GeV and for c_{12}^1 starting at a DM mass of about 1200 GeV. For a DM mass of 10000 GeV the upper limits on c_{12}^0 and c_{12}^1 are comparable to the ones from IC Sun. For all other interactions the assumption of higher annihilation cross sections, until DM capture - DM annihilation equilibrium is reached, does not lead to additional constraints, that are comparable to the upper limits from the other experiments. In any case the upper limits from IC Earth remain less stringent than the upper limits from XENON1T.

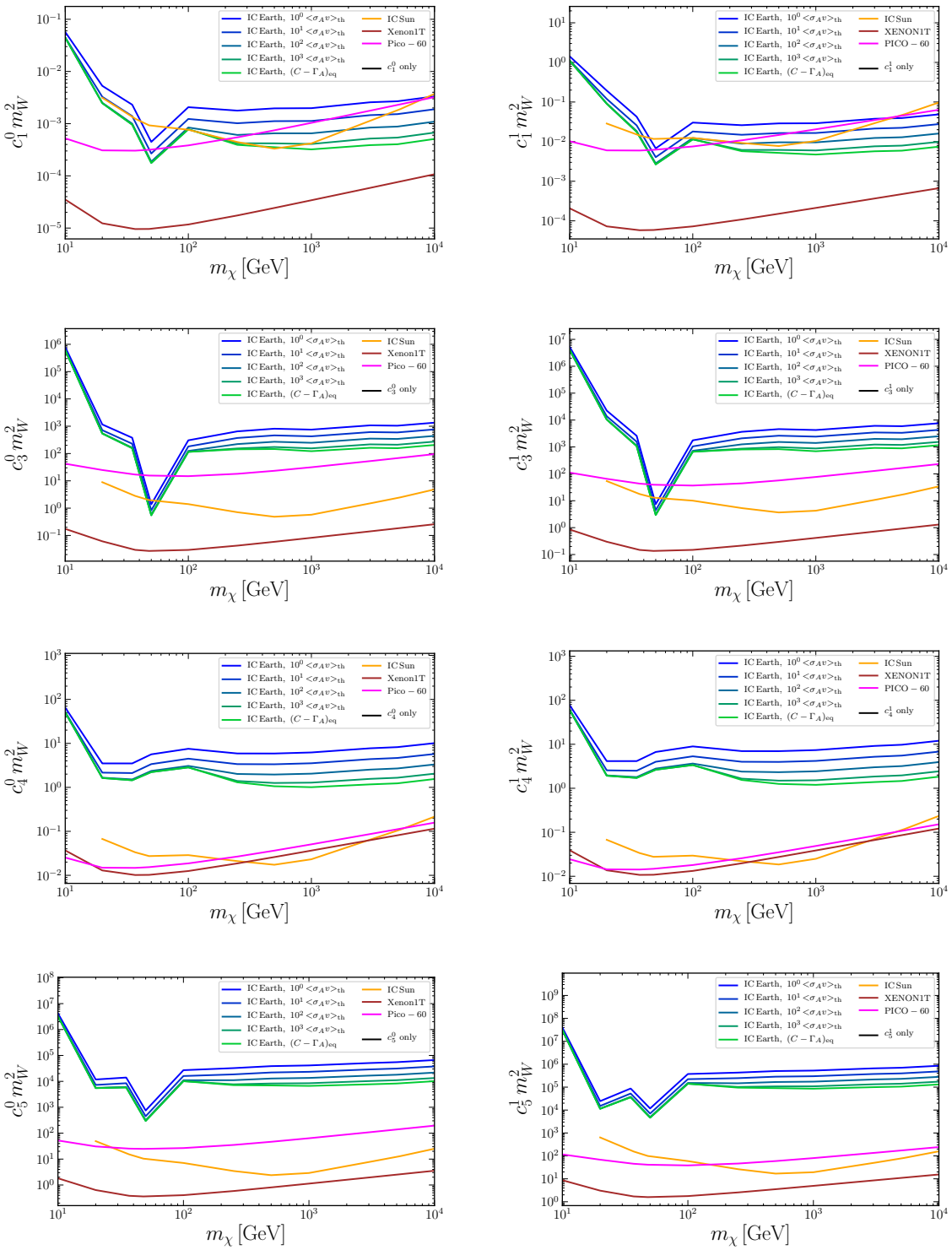

Figure 6.15 Upper limits on the coupling strengths c_i^τ, $i = 1, 3, 4, 5$, $\tau = 0, 1$ assuming no interference from IC Earth at the 90 % confidence level as function of the DM mass for increasing values of the annihilation cross-section, given as multiples of the thermal relic annihilation cross section $< \sigma_A v >_{\rm th} = 3 \cdot 10^{-26} {\rm cm}^3 {\rm s}^{-1}$ in blue, up to the point, where the upper limits reach the values in case of DM capture - DM annihilation equilibrium $(C - \Gamma_A)_{\rm eq}$ in green, compared to the upper limits from XENON1T in brown, PICO-60 in magenta, and IC Sun in yellow. The isoscalar strengths c_i^0 are depicted on the left side and the isovector strengths c_i^1 on the right sight.

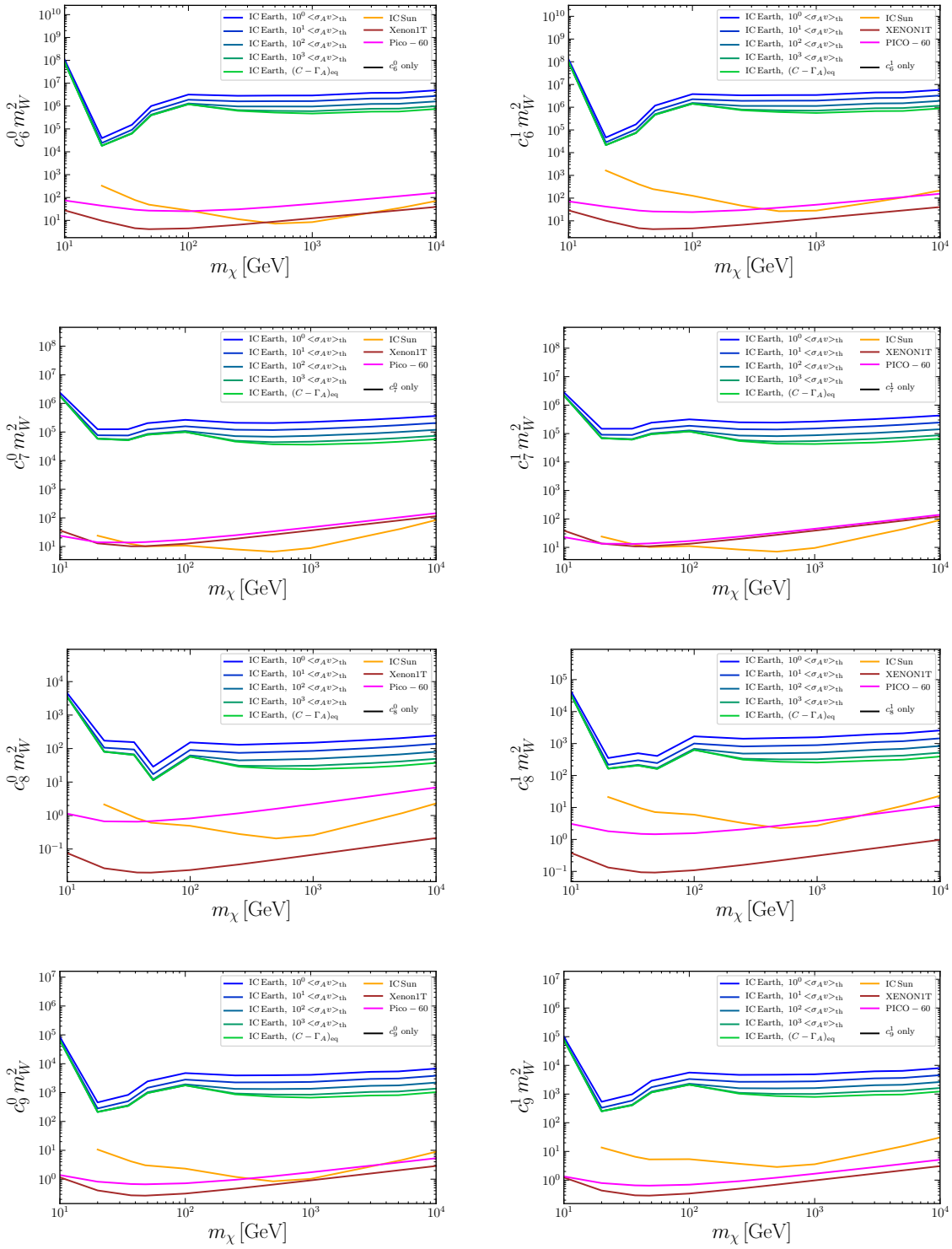

Figure 6.16 Same as figure 6.15 for coupling strengths $c_i^\tau,\ i = 6, ..., 9$.

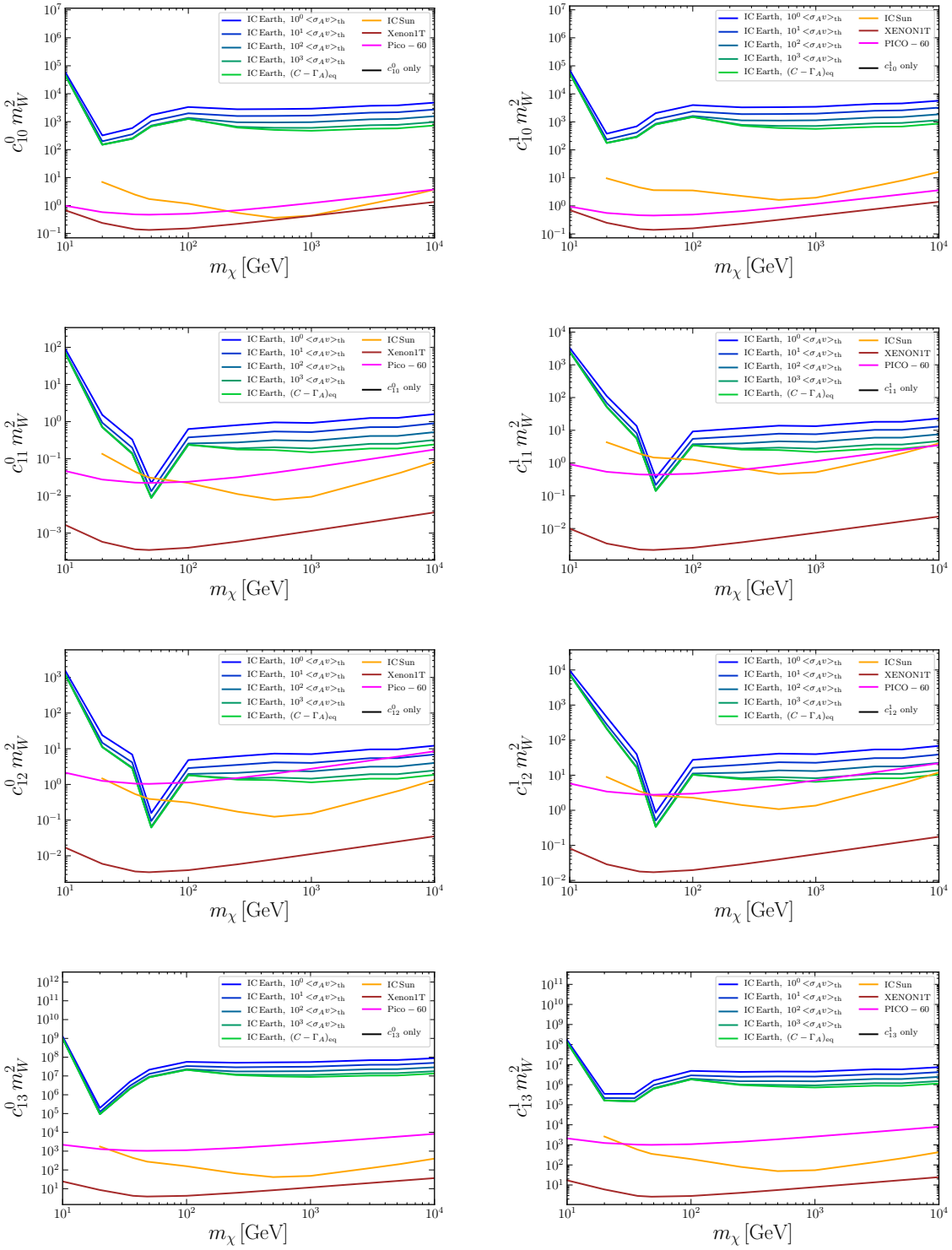

Figure 6.17 Same as figure 6.15 for coupling strengths c_i^τ, $i = 10, ..., 13$.

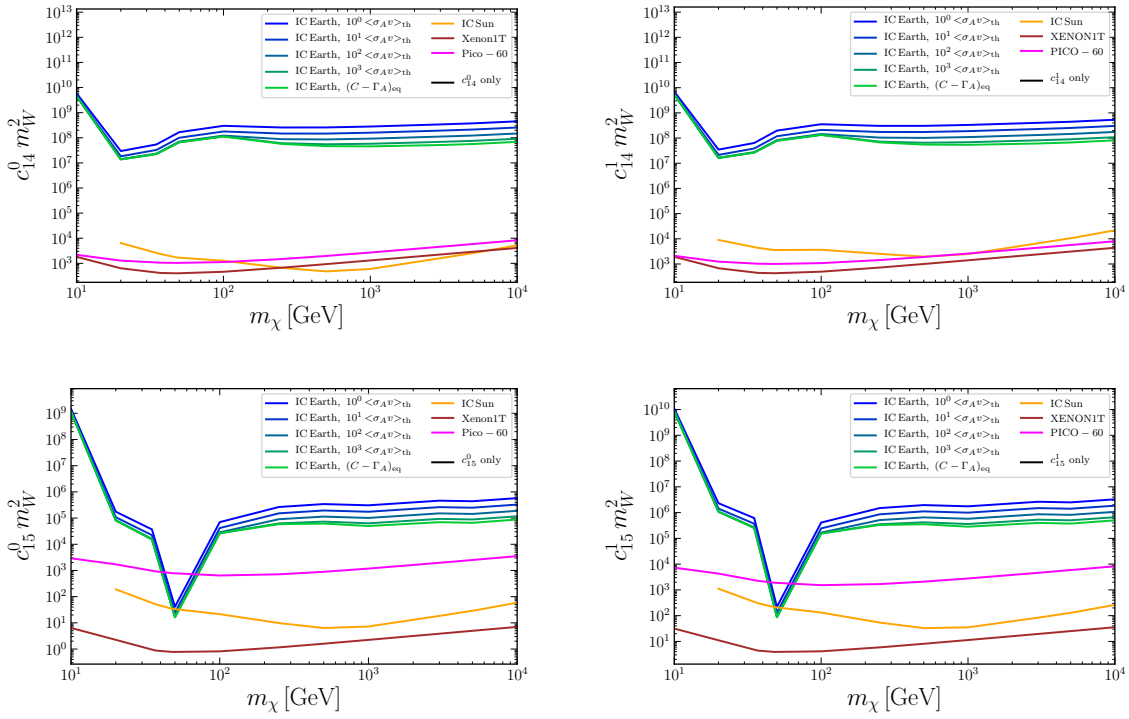

Figure 6.18 Same as figure 6.15 for coupling strengths c_i^τ, $i = 14, 15$.

In addition the upper limits on the coupling strengths from IC Earth in comparison to the upper limits from the other experiments at the 90 % confidence level assuming isoscalar - isovector interference and interference between all operators for increasing values of the annihilation cross-section as multiples of the thermal relic annihilation cross section are shown in appendix E. As seen in figure E.5 the upper limits on c_1^0 under interference between all operators from IC Earth assuming DM capture - DM annihilation equilibrium are comparable to the upper limits from XENON1T for a DM mass of 10000 GeV.

In figure 6.19 the upper limits on the spin-independent and spin-dependent DM-nucleon cross-section, obtained from the four experiments, are shown. The constraints from IC Sun are depicted in yellow, from XENON1T in brown and from PICO-60 in magenta. For IC Earth the results assuming the thermal relic annihilation cross-section are shown in cyan and assuming DM capture - DM annihilation equilibrium in green. The most stringent upper limits on the DM-nucleon spin-independent cross section assuming no interference are obtained from XENON1T. For the DM-nucleon spin-dependent cross section without interference the most stringent constraints below about 20 GeV are obtained from PICO-60, between about 300 GeV and 2500 GeV from IC Sun and for all other DM masses from XENON1T. This is similar to the results in the isoscalar-isovector basis for c_1^τ and c_4^τ. As a remark the spin-independent DM-nucleon cross-section corresponds to the coupling strength $c_1^\mathcal{N}$ and the spin-dependent DM-nucleon cross-section to the coupling strength $c_4^\mathcal{N}$ in the neutron-proton basis according to equation 5.22. Assuming isoscalar-isovector interference the most stringent upper limits on the spin-independent DM-nucleon cross section are obtained from XENON1T for all DM masses as in the isoscalar-isovector basis. However for the spin-dependent DM-nucleon cross section the basis change to the neutron-proton basis leads to most stringent constraints from other experiments than in the isoscalar-isovector basis. For the spin-dependent DM-neutron cross section the most stringent upper limits are obtained from IC Sun for DM masses between about 300 GeV and 2500 GeV, whereas for all other DM masses the most stringent constraints are obtained from XENON1T. This is in contrast to the isoscalar-isovector basis, where all most stringent upper limits are obtained from IC Sun. The reason for this change can be seen for a DM mass of 50 GeV in figure 6.14 at O_4. With the basis change to the neutron-proton basis the allowed regions are rotated by 45 degrees and

are almost aligned with the c_4^n - c_4^p parameter axes. The allowed region from XENON1T is very "thin" and elongated, which leads in the new neutron-proton basis under isoscalar-isovector interference to very stringent upper limits on the spin-dependent DM-neutron cross section and less stringent upper limits on the spin-dependent DM-proton cross section. Thus the most stringent upper limits on the spin-dependent DM-neutron cross section under isoscalar-isovector interference are obtained from XENON1T, whereas the most stringent upper limits on the spin-dependent DM-proton cross section under isoscalar-isovector interference are obtained from IC Sun for the investigated DM mass of 50 GeV. This effect also applies to the other DM masses, for which the most stringent constraints on the spin-dependent DM-neutron cross section under isoscalar-isovector interference are obtained from XENON1T. In general the upper limits under interference are always basis dependent through the rotation of the allowed regions in the parameter space at a basis change. Thus the basis dependence also applies to the interference between all operators, which leads to comparable outcomes as in case of isoscalar-isovector interference.

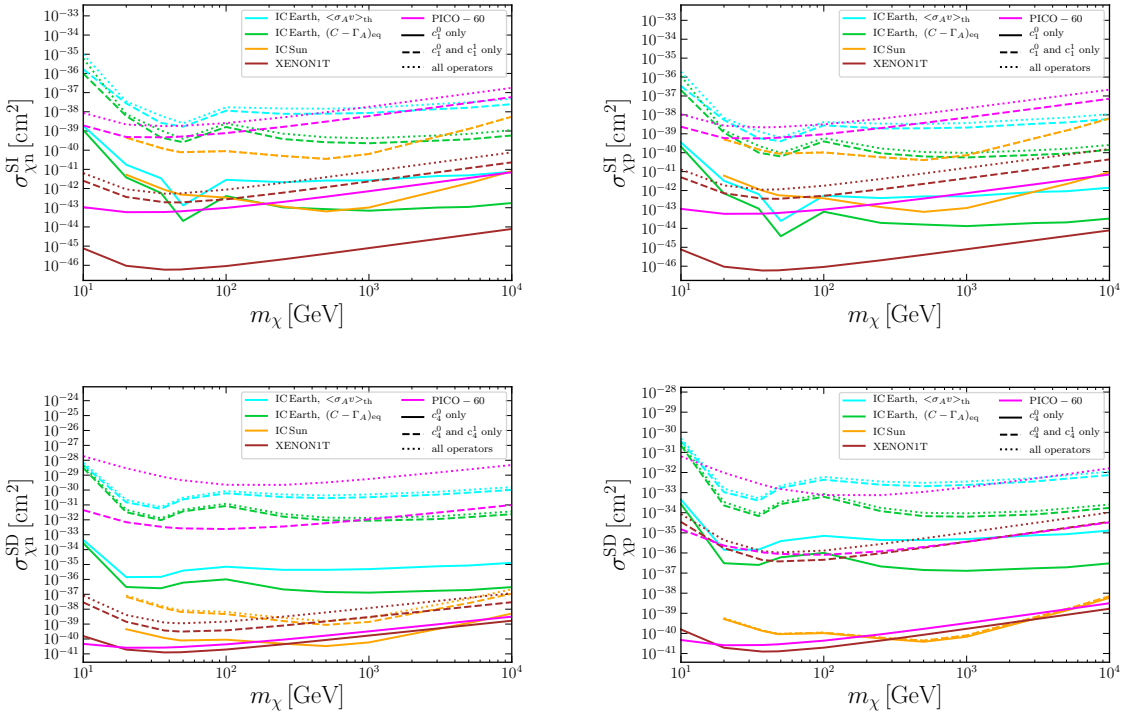

Figure 6.19 Upper limits on the spin-independent DM-nucleon cross section on top and the spin-dependent DM-nucleon cross section at the bottom at the 90% confidence level from the four experiments are shown. The constraints from IC Sun are depicted in yellow, from XENON1T in brown and from PICO-60 in magenta. For IC Earth the results assuming the thermal relic annihilation cross-section are shown in cyan and assuming DM capture - DM annihilation equilibrium in green. Results for the DM-neutron cross sections are on the left and for the DM-proton cross sections on the right. Solid lines represent the results considering no interference, i.e. c_1^0 is the only non-zero coupling strength for the spin-independent cross section and c_4^0 the only one for the spin-dependent cross section. The dashed lines show the results considering interference between the isoscalar and isovector interactions, i.e. c_1^0 and c_1^1 can be non-zero and interfere for the spin-independent cross section and c_4^0 and c_4^1 for the spin-dependent cross section. The dotted line shows the results considering interference between all interactions of the effective theory.

The comparison of the results for the DM-nucleon cross sections from IC Earth with the results from the other experiments is similar to the comparison of the results for the coupling strengths in the isoscalar-isovector basis, which is based on the fact, that the DM-nucleon cross sections are proportional to the respective squared coupling strengths and the allowed regions of all experiments stay in the same position to each other under a basis change. However this basis change can lead to differences in the results between

the experiments under the assumption of interference as explained before. The effect of the increasing annihilation cross section on the upper limits on the couplings strengths from IC Earth is the same in every basis and also for the constraints on the DM-nucleon cross sections as described in section 6.2. The factors, describing the impact of the changing annihilation cross sections on the upper limits on the DM-nucleon cross sections, can be seen in table 6.2. The upper limits from IC Earth are always larger than the most constraining ones independent of the assumption on the interference and on the annihilation cross section, but for a DM mass of 10000 GeV the upper limits on the spin-independent DM-proton cross-section under the assumption of interference between all operators and under DM capture - DM annihilation equilibrium are at the same order as the most constraining upper limits from Xenon1T, which is also the case for c_1^0 in the isoscalar-isovector basis. The results for interference between all operators are as mentioned before applicable to any model. Thus also results from IC Earth can be relevant under the assumption of DM capture - DM annihilation equilibrium and could be used for a combination of results from different experiments like in [15].

7 Constraining dark matter properties with Earth's internal heat flow

The IceCube experiment, its results and the analysis in this work are based on DM annihilations into neutrino final states. But DM also annihilates into other SM particles, that remain in the Earth's core and are a potential heat source inside Earth. In this chapter the possibility to set upper limits on the DM-nucleon cross sections by setting a constraint on the heat flow, induced by DM annihilations in the Earth's core, is investigated.

7.1 Internal heat flow of the Earth

The Earth is heated by the Sun. This heat is partly reflected by the atmosphere, the surface and the clouds and the rest is absorbed at low depths and re-radiated [85]. This assumption of an Earth-Sun heat equilibrium leads to an Earth's blackbody temperature of about 280 K, which coincides with the observed one between 250 K and 300 K. If the incident sunlight was instead absorbed by the Earth, a heating rate of about 170000 TW of the Earth would exist. In addition to this externally driven heat equilibrium, there exists an internal heat flow of Earth, which has minimal effects on the overall heat of the Earth, but can be measured underground and has been studied before [86].

In the experiments boreholes are drilled deep into the ground and temperature gradients are measured. Multiplying this temperature gradient with the thermal conductivity of the surrounding material yields a heat flux [87]. Compared to the radius of the Earth the deepest boreholes of about 12 kilometers are still rather close to Earth's surface and the measured temperature gradients are fairly high with values between 10 K/km and 50 K/km. With these temperature gradients all rock in the deeper parts of the Earth would be molten in contradiction to seismic measurements. Thus they cannot hold for larger depths. Current estimates place temperature gradients for the Earth's interior between 0.6 K/km and 0.8K/km. Averaging over all measurements the internal heat flux is about 0.087 W/m^2, which gives, by integrating over the surface of the Earth, an internal heat flow of approximately 44.2 TW [88]. This heat flow is independent of the solar flux and anything above Earth's surface and its measurement is unique to Earth compared to other planets [14].

While the value of the heat flow is well known, its complete origin is under theoretical debate. The decay of Uranium and Thorium in the crust produces a significant amount of heat in the Earth, namely about 40 % of the total [88]. The decay of other radioactive elements like potassium adds to this, although there is much less in the crust, but potentially more in the mantle or the outer core. The origin of the remaining heat is yet undetermined and is based on processes in the core or even the mantle. This is underpinned by models of the core's heat output, that give values between 2.3 TW and 21 TW [89]. Thus there exists a residual internal heat flow in the Earth, for which so far no origin is known and which can therefor potentially be used as an upper limit on the heat flow from DM annihilations. A conservative choice to constrain the heat flow, induced by DM annihilations in the Earth's core, is 20 TW [14].

7.2 Constraints on the DM-nucleon cross sections from Earth's residual internal heat flow

The heat flow resulting from DM annihilations can be used to set model-independent constraints on the DM-nucleon cross sections $\sigma^{SI}_{\chi\mathcal{N}}$. This has been done in [14] for the spin-independent DM-nucleon cross section, whereby the cross section is assumed to be larger than for typical weakly interacting DM particles. Figure 7.1 is taken from this paper. It shows on the left side the constraints in the $\sigma^{SI}_{\chi\mathcal{N}}$-$m_\chi$ plane from astrophysical observations in green, from high-altitude detectors in light red and from underground detectors in yellow. Very large cross sections are constrained by astrophysical limits from the stability of the Milky Way disk [90], from cosmic rays[91] and from the CMB [92]. Small cross-sections are examined by underground detectors like XENON1T and PICO-60. For these experiments the cross section of DM has to be large enough to cause a nuclear recoil, but small enough to allow the DM to pass through the Earth to the detector, in order to be detected [14]. In between is the window, where $\sigma^{SI}_{\chi\mathcal{N}}$ can be relatively large. In some extent this window has been excluded by high altitude experiments, but not completely and these exclusions are partly doubtful according to [14]. Thus the authors of the paper investigate the cross sections in this window. The investigation is based on DM capture and annihilation in the Earth, whereby SM final states are assumed, that deposit nearly all their energy in the Earth's core. Through this process a heat flow would be produced, that is, with 3260 TW, more than 2 orders of magnitudes larger than the residual measured value of Earth's internal heat flow and thus a large area in the $\sigma^{SI}_{\chi\mathcal{N}}$-$m_\chi$ plane can be excluded.

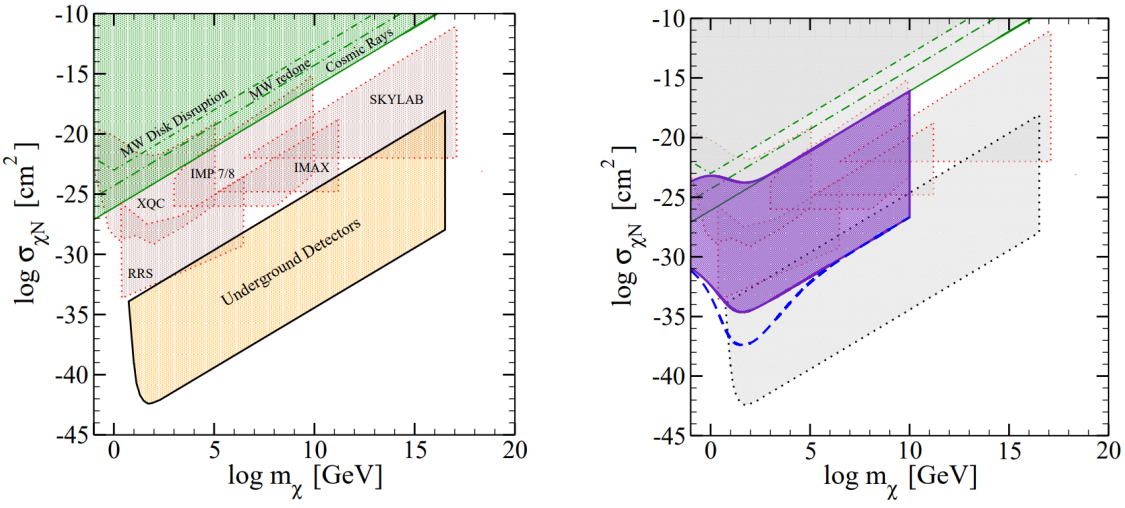

Figure 7.1 On the left side the constraints in the $\sigma^{SI}_{\chi\mathcal{N}}$-$m_\chi$ plane are shown from astrophysical detectors in green, from high-altitude detectors in light red and from underground detectors in yellow. On the right sight the violet area in the $\sigma^{SI}_{\chi\mathcal{N}}$-$m_\chi$ plane shows the spin-independent DM-nucleon cross sections, for which DM annihilations lead to an internal heat flow, which is more than 2 orders of magnitude larger than the residual measured internal heat flow in the Earth. Above the dashed line DM capture is only efficient enough to lead to a heat flow equal to or larger than the residual measured Earth's internal heat flow. The figures are taken from [77].

This area is shown in figure 7.1 on the right side. The upper bound on this area is set by the condition, that the spin-independent DM-nucleon cross section has to be small enough, that DM has sufficient time to drift to the core after been captured. The lower bound results from the condition, that the capture of DM has to be efficient, which means that the cross section has to be so large, that 90 % of the DM particles, traversing the Earth, are captured in order to efficiently produce heat. In addition a Poisson probability is used to compute a lower bound on the cross section, where the capture rate is not so efficient, so that the heat flow from DM annihilations equals to or is larger than the residual measured Earth's internal heat flow. In this paper constraints from neutrino experiments are not included,

resonant scattering is neglected and an equilibrium between DM capture and DM annihilation is assumed.

The focus in this chapter will be to fine-tune the upper limits on the DM-nucleon cross sections under the constraint, that the upper limit on the heat flow from DM annihilations in the Earth's core is bounded by the residual measured Earth's internal heat flow. Hereby the DM capture rate will be computed by the formalism presented in chapter 3, which includes resonant scattering, and the upper limits on the DM-nucleon cross sections will be computed with the formalism of chapter 5, which leads to rigorous model-independent results, where DM capture - DM annihilation equilibrium is not assumed. In addition an upper limit on the heat flow, induced by DM annihilations in the Earth's core, based on the results from IceCube, will be calculated, which sets an upper limit on a potential DM contribution to the residual measured Earth's internal heat flow.

In order to set the constraints on the DM-nucleon cross-sections by using the residual measured Earth's internal heat flow as upper limit on the heat flow from DM annihilations, some assumptions have to be made. The first one is an estimate of the kinetic heating due to DM capture. Since DM particles are considered to move non-relativistically with a velocity of approximately $10^{-3}c$, the maximum energy transfer to the nucleons during scattering is about 10^{-6} of the possible annihilation energy $m_\chi c^2$. Thus the contribution of kinetic heating is negligible. How much energy is transferred through DM annihilations into heat in the Earth's core depends on the annihilation channels and their branching ratios. The basic channels into which DM annihilates are: $q\bar{q}$, $l\bar{l}$, $\nu\bar{\nu}$, W^+W^-, ZZ and Higgs particles or mixed Higgs/gauge boson final states [75]. Only neutrinos can escape from the Earth's core and thus do not participate in the heating of it. By contrast all other particles deposit all their energy, apart from small corrections due to particle rest masses, in the Earth's core. Thus the possible annihilation energy $m_\chi c^2$ is reduced by the energy of the neutrinos. Besides the direct annihilation into $\nu\bar{\nu}$, neutrinos originate as final states from the decays of the SM particles, produced in the DM annihilations. Charged leptons, apart from electrons, produce neutrinos. In the case of quarks, hadronization will produce hadrons, whose subsequent decay can produce neutrinos. The decay of gauge bosons and Higgs particles produces leptons or quarks, which follow the previously described evolution. All these neutrinos will reduce the available energy for heating through DM annihilations. Some examples are listed in the following for ν_μ and $\bar{\nu}_\mu$ as final states from [75], where the mass dependence on m_χ is based on oscillations and on energy losses of primary particles: For a DM annihilation into $b\bar{b}$, like in the soft channel of IceCube, ν_μ and and $\bar{\nu}_\mu$ have a mass dependent average energy of 10 % of the total available annihilation energy $m_\chi c^2$, for an annihilation into $\tau^+\tau^-$ between 22 % and 32 % of $m_\chi c^2$ and for an annihilation into W^+W^- between 34 % and 36 % of $m_\chi c^2$, as in the hard channels of IceCube. For an annihilation directly into $\nu\bar{\nu}$ the neutrino energy is 100 % of $m_\chi c^2$. Thus the used DM model with its annihilation channels and their branching ratios determines the possible heat deposit into Earth's core due to DM annihilations. For this analysis the same assumption as in [14] will be made, that all energy is used for the heating of Earth's core, which results in the most stringent upper limits on the DM-nucleon cross sections. Adaptions to specific DM models can be made by using the annihilation channel dependent neutrino energy losses. Under this assumption the heat flow Γ_{heat} can be transferred into the total DM annihilation rate Γ_A via:

$$\Gamma_A = \frac{1}{2}\frac{\Gamma_{\text{heat}}}{m_\chi} \,. \tag{7.1}$$

This relation can be used in equation 3.4, so that:

$$\frac{1}{2}\frac{\Gamma_{\text{heat}}}{m_\chi} = \frac{1}{2}C_A N(t_\oplus)^2 = \frac{1}{2}C \tanh^2\left(\frac{t_\oplus}{\tau}\right) \,. \tag{7.2}$$

With this equation the upper limits on the coupling strengths according to equation 5.9 can be determined and with these the constraints on the DM-nucleon cross sections according to equation 5.22.

7.3 Results from Earth's residual internal heat flow

As a first step the mass dependent upper limits on the total DM annihilation rate are calculated with equation 7.1 by using the residual measured Earth's internal heat flow of 20 TeV as upper limit on the heat flow from DM annihilations. The results are shown in table 7.1.

m_χ [GeV]	10	20	35	50	100	250	500	1000	3000	5000	10000
$\Gamma_A^{\text{u.l.}}$ [10^{18}s^{-1}]	6240	3120	1780	1250	624	250	125	62.4	20.8	12.5	6.24

Table 7.1 Upper limits on the total DM annihilation rate $\Gamma_A^{\text{u.l.}}$, calculated by using the residual measured Earth's internal heat flow as upper limit on the heat flow from DM annihilations, for the investigated DM masses m_χ.

By evaluating equations 5.9 and 5.22 with the procedure described in chapter 5, rigorous upper limits on the spin-independent and spin-dependent DM-nucleon cross section, based on the calculated upper limits on the total DM annihilation rate, were derived, which are depicted in figure 7.2. The cyan lines represent the constraints on the DM-neutron cross sections and the violet lines on the DM-proton cross sections. Hereby the solid lines show the upper limits assuming that c_1^0 is the only non-zero coupling strength for the spin-independent and c_4^0 for the spin-dependent cross sections. The dashed lines show the results assuming that both c_1^0 and c_1^1 for the spin-independent cross sections and c_4^0 and c_4^1 for the spin-dependent cross sections can be non-zero and interfere, whereas all other coupling strengths vanish. The dotted lines show the upper limits on the DM-nucleon cross sections under the assumption, that all coupling strengths can be non-zero and interfere.

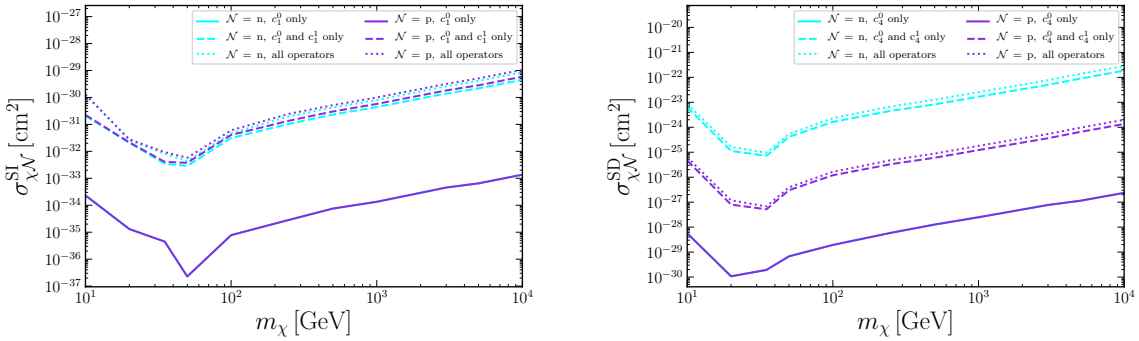

Figure 7.2 Upper limits on the spin-independent DM-nucleon cross section $\sigma^{\text{SI}}_{\chi\mathcal{N}}$ on the left and on the spin-dependent DM-nucleon cross section $\sigma^{\text{SD}}_{\chi\mathcal{N}}$ on the right as function of the DM mass m_χ, derived by using the residual measured Earth's internal heat flow as upper limit on the heat flow from DM annihilations assuming that all energy of the DM particles is used for heating in Earth's core. In cyan are the upper limits on the DM-neutron cross sections and in violet on the DM-proton cross sections. The solid line shows the results considering no interference, the dashed line shows the results considering isoscalar-isovector interference and the dotted line shows the results considering interference between all interactions of the effective theory.

There is no impact of an increasing annihilation cross section on the upper limits, as DM capture - DM annihilation equilibrium for such a relatively large DM-nucleon cross section has already been attained. This can be seen in equation 7.2, where it holds for the thermal relic annihilation cross section $< \sigma_A v >_{\text{th}}$: $\tanh^2(t_\oplus/\tau) = 1$ for all investigated DM masses, given the numerical precision of the computations. Thus also the less computational demanding form to derive the upper limits on the coupling strengths of equation 5.14 could be used for the computations. The impact of interference is the same as before

in case of the IceCube upper limits. Assuming interference relaxes the constraints and leads to rigorous model-independent upper limits on the DM-nucleon cross sections.

In order to compare the results of this work with the results from [14] the spin-independent DM-nucleon cross-section assuming no interference is used. The resonant capture of DM leads to a peak in the upper limits on the spin-independent DM-nucleon cross section assuming no interference for a DM mass of approximately 50 GeV. At this DM mass the results are comparable to the ones from the paper. But in the paper the peak in the upper limits, computed by a Poisson distribution, is very broad leading to deviations to the results of this work. For a DM mass of 10 GeV the upper limits on the cross section in the paper are 3 orders of magnitude smaller than the results of this work, for a DM mass of 100 GeV and 1000 GeV they are 2 orders of magnitude smaller and for a DM mass of 10000 GeV they are 1 order of magnitude smaller. Thus the detailed calculations of this work lead to weaker upper limits on the spin-independent DM-nucleon cross section than previously computed in [14]. But this result does not have an impact on the main focus of the paper to close the window between the upper limits from underground experiments and the upper limits from astrophysical observations.

The upper limits on the DM-nucleon cross sections, that are derived by using the residual measured Earth's internal heat flow as upper limit on the heat flow from DM annihilations, are by far weaker than the upper limits derived from IceCube data. As the upper limit on the DM total annihilation rate, derived from the residual measured Earth's internal heat flow, is between 5 orders of magnitude for a DM mass of 10 GeV and 10 orders of magnitude for a DM mass of 10000 GeV larger than in case of IceCube date, also the upper limits on the DM-nucleon cross-sections become larger. They are between 5 orders of magnitude weaker for a DM mass of 10 GeV and 8 orders of magnitude weaker for a DM mass of 10000 GeV than in case of IceCube data, where DM capture - DM annihilation equilibrium cannot be assumed, which increases the bounds especially for higher DM masses. As a remark the assumption on the annihilation channels can change the bounds in both cases and thus, dependent on the concrete used DM model and respective assumptions, the results can be adapted.

By using the upper limits on the total DM annihilation rate from IceCube data $\Gamma_A^{\text{u.l.}}$, assuming the hard channels, an upper bound on the internal heat flow of the Earth $\Gamma_{\text{heat}}^{\text{u.l.}}$, induced by DM annihilations in Earth's core, can be set. This is done straight forward by solving equation 7.1 for Γ_{heat}, under the assumption, that all DM energy is deposited in Earth's core, which leads to the maximal limits on the heat flow. The results are shown in table 7.2.

m_χ [GeV]	10	20	35	50	100	250	500	1000	3000	5000	10000
$\Gamma_{\text{heat}}^{\text{u.l.}}$ [10^3W]	96500	5770	2640	1790	1040	72.6	22.4	10.4	4.50	3.40	2.58

Table 7.2 Upper limits on the internal heat flow of the Earth $\Gamma_{\text{heat}}^{\text{u.l.}}$, induced by DM annihilations in Earth's core, calculated by using the upper limit on the total DM annihilation rate from IceCube data assuming the hard channels, for the investigated DM masses m_χ.

The highest upper limit on the internal heat flow of the Earth is derived for a DM mass of 10 GeV. Even at this DM mass the internal heat flow is about 5 orders of magnitude smaller than the Earth's residual measured internal heat flow of 20 TW. Thus based on IceCube data only a very small fraction of Earth's residual measured internal heat flow could be based on a potential heat flow in the Earth induced by DM annihilations in the Earth's core.

8 Conclusion and Outlook

During Earth's journey through the galaxy, DM particles from the galactic halo become captured in the gravitational field of the Earth via weak interactions with nucleons. Through subsequent scatterings the DM particles loose energy and sink to Earth's core, where they thermalise and self-annihilate into SM particles. From these only neutrinos can escape Earth's core and can be measured directly in detectors. All other particles remain in the Earth and can contribute to the residual measured internal heat flow of the Earth. In this work measurements from the Earth are used to determine rigorous model independent upper limits on the coupling strengths of the non-relativistic effective theory of DM-nucleon interactions and on the corresponding DM-nucleon cross sections, taking into account interference among operators. Hereby the main part of the work is based on data, collected by the IceCube observatory in a search for DM annihilations in the Earth. Through the non-observation of an exotic neutrino flux from the Earth's center upper limits on the total DM annihilation rate for different DM masses can be set. From these constraints the upper limits on the coupling strengths including interference at the 90 % confidence level can be determined with the formalism presented in this work. Hereby the whole parameter space of the effective theory of all possible 28 interactions and their interference for spin-1/2 DM, for DM masses between 10 GeV and 10000 GeV, has been investigated. The most stringent constraints are obtained in case of resonant capture, which arises for many interactions at a DM mass of 50 GeV due to ^{56}Fe.

In published limits the DM-nucleon interaction is commonly assumed to be isoscalar, which is very restrictive, as in many DM models the DM-nucleon interaction is not the same for protons and neutrons. Under the assumption of isoscalar-isovector interference the upper limits on several coupling strengths are relaxed by about two orders of magnitude according to the calculations of this work. Hereby the impact of interference is dependent on the chosen basis, which is in this work for the coupling strengths the isoscalar-isovector basis. The corresponding upper limits on the DM-nucleon cross sections in the neutron-proton basis are relaxed by three orders of magnitude and in case of the spin-dependent DM-neutron cross section even by five orders of magnitude when assuming isoscalar-isovector interference. In published limits only the spin-independent and spin-dependent interaction are considered, but in order to be applicable to any DM model all interactions and interference between them have to be included. This can lead to further relaxation of the upper limits depending on the considered coupling strength.

For the Earth an equilibrium between DM capture and DM annihilation can not be assumed, which leads to upper limits, that are dependent on the assumed annihilation cross section. An increasing annihilation cross section leads to lower upper limits on the coupling strengths. Hereby it holds up to a DM mass of 3000 GeV: the higher the DM mass is, the stronger is the impact on the upper limits and the later DM capture - DM annihilation equilibrium is attained. For DM masses between 3000 GeV and 10000 GeV the effect of an increasing annihilation cross section remains approximately the same, independent of the investigated DM mass. The factors, by which the upper limits are reduced, compared to the commonly assumed thermal relic annihilation cross section, are independent of the considered interaction and the chosen basis. The most stringent upper limits are obtained for values of the annihilation cross section, where DM capture - DM annihilation equilibrium is attained. In this case the upper limits on the coupling strengths can be lowered for a DM mass of 50 GeV by a factor of about 2.5 and for a DM mass of 10000 GeV by a factor of about 6.5, compared to the upper limits obtained under the assumption of the thermal relic annihilation cross section. For the upper limits on the DM-nucleon cross sections these factors have to be squared.

The results of this work are compared to the results of three other experiments: an IceCube search into the direction of the Sun, where DM capture - DM annihilation equilibrium has already been attained, and two direct detection experiments: XENON1T and PICO-60. For most interactions the most stringent upper limits on the coupling strengths assuming no interference are obtained from XENON1T. As the results from the IceCube search in the direction of the Sun are not as much affected by the impact of interference as the results from the other experiments, several coupling strengths are the most constraint by this experiment under interference. The upper limits from the IceCube search in the center of the Earth are almost for the whole parameter space of the effective theory less restrictive than the most constraining upper limits from the other experiments. But for a DM mass of 10000 GeV under the assumption of interference between all operators and an annihilation cross section, where DM capture - DM annihilation equilibrium has been attained, the upper limits on the coupling strength c_1^0 and on the spin-independent DM-proton cross section are at the same order of magnitude as the most constraining upper limits from the other experiments, namely from Xenon1T.

In the Earth an internal heat flow can be measured, for which to some extent the origin is unknown so far. Using this residual measured heat flow as a constraint on the heat flow, induced by DM annihilations, upper limits on the DM-nucleon cross sections can be derived. These constraints are, as before, based on DM capture and annihilation in the Earth. In contrast to the previous results neutrinos are not measured or take part in the heating, instead all other SM particles, into which DM annihilates, contribute to Earth's residual measured heat flow. The resultant upper limits are at least 5 orders of magnitudes weaker than the previous computed ones, based on the non-observation of an exotic neutrino flux. Thus, based on IceCube data, also only a very small fraction of Earth's residual measured heat flow could be based on DM annihilations.

New results from the IceCube collaboration for a 8-years DM search in the Earth are pending. They will improve the upper limits on the spin-independent DM-nucleon cross section by approximately 1 order of magnitude, making them, under the assumption of a large annihilation cross section, competitive to the most constraining upper limits from the other experiments for a wide range of DM masses and different assumptions on the interference. One can expect, that with the new results also all upper limits on the coupling strengths will become more restrictive. Thus an analysis of the new IceCube data can lead to more stringent results, that could be comparable to other experiments in a wider range of the parameter space of the non-relativistic effective theory of DM-nucleon interactions. In order to fine-tune a new analysis, a more sophisticated Earth model than used in this work could be applied, which includes also less abundant elements and the atmosphere of the Earth. An effective way to constrain the parameter space of the non-relativistic effective theory of DM-nucleon interactions is the combination of the results from different experiments, especially in case of operators depending on spin-dependent nuclear response functions, as allowed regions of these operators are, depending on the target material, often rectangular to each other. Thus an analysis of the pending IceCube data from observations of Earth's center with an improved Earth model including the combination of results from different experiments could follow this work.

A Earthmodel

Several assumptions have to be made, in order to derive upper limits on the coupling strengths of the non-relativistic effective theory of DM-nucleon interactions and the corresponding DM-nucleon cross sections including interference between the different interactions. In this work these constraints are set based on IceCube observations of Earth's center. Therefor the composition of the Earth has to be known exactly, because it strongly influences the DM capture rate via equation 3.22. The used Earth model is called preliminary reference Earth model (PREM) [44]. It is a one-dimensional model of the average Earth properties as function of the radius. It includes elastic properties, density, attenuation, pressure, and gravity. PREM is based on a large data set of astronomic-geodetic data, free oscillation and long-period surface wave data and body waves. To be in agreement with the entire data set PREM incorporates anelastic dispersion and anisotropy and therefore the model is frequency-dependent and for the upper mantle transversely isotropic.

From this model the density and mass as function of the radius are used, whereat the chemical composition of the Earth is divided into two regions. The inner region goes out to 54.4 % of Earth's radius with a total mass portion of 32.2 % of Earth's mass. The remaining part of the radius and mass belongs to the outer region. The inner region is called Earth's core and the outer region Earth's mantle. For the calculations the Earth is a perfect sphere with a radius of 6379.1 km and a total mass of $5.9722 * 10^{24}$ kg. The chemical composition in the core and the mantle is shown in table A.1.

Elements [%]	^{16}O	^{23}Na	^{24}Mg	^{27}Al	^{28}Si	^{31}P	^{32}S	^{40}Ca	^{52}Cr	^{56}Fe	^{58}Ni
Core	0.000	0.000	0.000	0.000	6.000	0.200	1.900	0.000	0.900	85.500	5.200
Mantle	44.00	0.270	22.800	2.350	21.000	0.009	0.025	2.530	0.260	6.260	0.196

Table A.1 Chemical composition of the Earth, following PREM

B DM response functions

The DM response functions, used in equation 3.16, are listed here according to [49] [53]. The DM particle spin J_χ is set to 1/2 in this work.

$$
\begin{aligned}
R_M^{\tau,\tau'}\left(v_\mathcal{T}^{\perp 2}, \frac{q^2}{m_\mathcal{N}^2}\right) &= c_1^\tau c_1^{\tau'} + \frac{J_\chi(J_\chi+1)}{3}\left[\frac{q^2}{m_\mathcal{N}^2} v_\mathcal{T}^{\perp 2} c_5^\tau c_5^{\tau'} + v_\mathcal{T}^{\perp 2} c_8^\tau c_8^{\tau'} + \frac{q^2}{m_\mathcal{N}^2} v_\mathcal{T}^{\perp 2} c_{11}^\tau c_{11}^{\tau'}\right] \\
R_{\Phi''}^{\tau,\tau'}\left(v_\mathcal{T}^{\perp 2}, \frac{q^2}{m_\mathcal{N}^2}\right) &= \frac{q^2}{4m_\mathcal{N}^2} c_3^\tau c_3^{\tau'} + \frac{J_\chi(J_\chi+1)}{12}\left(c_{12}^\tau - \frac{q^2}{m_\mathcal{N}^2} c_{15}^\tau\right)\left(c_{12}^{\tau'} - \frac{q^2}{m_\mathcal{N}^2} c_{15}^{\tau'}\right) \\
R_{\Phi'' M}^{\tau,\tau'}\left(v_\mathcal{T}^{\perp 2}, \frac{q^2}{m_\mathcal{N}^2}\right) &= c_3^\tau c_1^{\tau'} + \frac{J_\chi(J_\chi+1)}{3}\left(c_{12}^\tau - \frac{q^2}{m_\mathcal{N}^2} c_{15}^\tau\right) c_{11}^{\tau'} \\
R_{\Phi'}^{\tau,\tau'}\left(v_\mathcal{T}^{\perp 2}, \frac{q^2}{m_\mathcal{N}^2}\right) &= \frac{J_\chi(J_\chi+1)}{12}\left[c_{12}^\tau c_{12}^{\tau'} + \frac{q^2}{m_\mathcal{N}^2} c_{13}^\tau c_{13}^{\tau'}\right] \\
R_{\Sigma''}^{\tau,\tau'}\left(v_\mathcal{T}^{\perp 2}, \frac{q^2}{m_\mathcal{N}^2}\right) &= \frac{q^2}{4m_\mathcal{N}^2} c_{10}^\tau c_{10}^{\tau'} + \frac{J_\chi(J_\chi+1)}{12}\left[c_4^\tau c_4^{\tau'} + \frac{q^2}{m_\mathcal{N}^2}(c_4^\tau c_6^{\tau'} + c_6^\tau c_4^{\tau'})\right. \\
&\quad \left. + \frac{q^2}{m_\mathcal{N}^4} c_6^\tau c_6^{\tau'} + v_\mathcal{T}^{\perp 2} c_{12}^\tau c_{12}^{\tau'} + \frac{q^2}{m_\mathcal{N}^2} v_\mathcal{T}^{\perp 2} c_{13}^\tau c_{13}^{\tau'}\right] \\
R_{\Sigma'}^{\tau,\tau'}\left(v_\mathcal{T}^{\perp 2}, \frac{q^2}{m_\mathcal{N}^2}\right) &= \frac{1}{8}\left[\frac{q^2}{m_\mathcal{N}^2} v_\mathcal{T}^{\perp 2} c_3^\tau c_3^{\tau'} + v_\mathcal{T}^{\perp 2} c_7^\tau c_7^{\tau'}\right] + \frac{J_\chi(J_\chi+1)}{12}\left[c_4^\tau c_4^{\tau'} + \frac{q^2}{m_\mathcal{N}^2}(c_9^\tau c_9^{\tau'}\right. \\
&\quad \left. + \frac{v_\mathcal{T}^{\perp 2}}{2}\left(c_{12}^\tau - \frac{q^2}{m_\mathcal{N}^2} c_{15}^\tau\right)\left(c_{12}^{\tau'} - \frac{q^2}{m_\mathcal{N}^2} c_{15}^{\tau'}\right) + \frac{q^2}{2m_\mathcal{N}^2} v_\mathcal{T}^{\perp 2} c_{14}^\tau c_{14}^{\tau'}\right] \\
R_{\Delta}^{\tau,\tau'}\left(v_\mathcal{T}^{\perp 2}, \frac{q^2}{m_\mathcal{N}^2}\right) &= \frac{J_\chi(J_\chi+1)}{3}\left[\frac{q^2}{m_\mathcal{N}^2} c_5^\tau c_5^{\tau'} + c_8^\tau c_8^{\tau'}\right] \\
R_{\Delta\Sigma'}^{\tau,\tau'}\left(v_\mathcal{T}^{\perp 2}, \frac{q^2}{m_\mathcal{N}^2}\right) &= \frac{J_\chi(J_\chi+1)}{3}\left[c_5^\tau c_4^{\tau'} - c_8^\tau c_9^{\tau'}\right]
\end{aligned}
\tag{B.1}
$$

C Nuclear response functions

The nuclear response functions, used in equation 3.16, are listed here as analytic expressions according to [12] [52], for all elements of this work, contained in the used Earth model PREM. They were determined by using the mathematica package DMFormFactor from [53], in order to evaluate the reduced matrix elements of nuclear charges and currents in the harmonic oscillator basis. This requires as an input one-body density matrix elements (OBDMEs) for ground-state to ground-state transitions of the target nuclei, that were computed by using the shell model code Nushell@MSU [93] [94]. In the harmonic oscillator basis the nuclear response functions depend on the momentum transfer through the variable $y = (bq/2)^2$ with the harmonic oscillator basis length parameter $b = \sqrt{41.467/(45A^{-1/3} - 25A^{-2/3}}$ fm. Only non-zero nuclear response functions are listed.

Oxygen (^{16}O)

$$
\begin{aligned}
W_M^{00}(y) &= 0.000032628(395.084 - 200.042y + y^2)^2 e^{-2y} \\
W_{\Phi''}^{00}(y) &= 0.000032628(3.66055 - y)^2 e^{-2y} \\
W_{M\Phi''}^{00}(y) &= (-0.0471874 + 0.0367831y - 0.00664641y^2 + 0.000032628y^3) e^{-2y}
\end{aligned} \tag{C.1}
$$

Sodium (^{23}Na)

$$
\begin{aligned}
W_M^{00}(y) &= (42.0965 - 63.4498y + 32.5913y^2 - 6.57878y^3 + 0.483166y^4) e^{-2y} \\
W_M^{01}(y) &= (-1.83028 + 3.81972y - 2.50445y^2 + 0.597822y^3 - 0.04545y^4) e^{-2y} \\
W_M^{10}(y) &= (-1.83028 + 3.81972y - 2.50445y^2 + 0.597822y^3 - 0.04545y^4) e^{-2y} \\
W_M^{11}(y) &= (0.0795776 - 0.212207y + 0.182941y^2 - 0.0543892y^3 + 0.00523012y^4) e^{-2y} \\
W_{\Sigma''}^{00}(y) &= (0.0126672 - 0.0262533y + 0.0401886y^2 - 0.010514y^3 + 0.00078605y^4) e^{-2y} \\
W_{\Sigma''}^{01}(y) &= (0.0107811 - 0.020986y + 0.0360971y^2 - 0.00876213y^3 + 0.000626718y^4) e^{-2y} \\
W_{\Sigma''}^{10}(y) &= (0.0107811 - 0.020986y + 0.0360971y^2 - 0.00876213y^3 + 0.000626718y^4) e^{-2y} \\
W_{\Sigma''}^{11}(y) &= (0.00917577 - 0.0167053y + 0.0332751y^2 - 0.00765719y^3 + 0.000597676y^4) e^{-2y} \\
W_{\Sigma'}^{00}(y) &= (0.0253345 - 0.0750847y + 0.100235y^2 - 0.0384261y^3 + 0.00466396y^4) e^{-2y} \\
W_{\Sigma'}^{01}(y) &= (0.0215622 - 0.0652627y + 0.0941439y^2 - 0.0379511y^3 + 0.00472138y^4) e^{-2y} \\
W_{\Sigma'}^{10}(y) &= (0.0215622 - 0.0652627y + 0.0941439y^2 - 0.0379511y^3 + 0.00472138y^4) e^{-2y} \\
W_{\Sigma'}^{11}(y) &= (0.0183515 - 0.0567009y + 0.0887794y^2 - 0.0374699y^3 + 0.00477955y^4) e^{-2y} \\
W_{\Phi''}^{00}(y) &= ((0.612149 - 0.49308y + 0.107832y^2) e^{-2y} \\
W_{\Phi''}^{01}(y) &= (-0.075893 + 0.060682y - 0.0110124y^2) e^{-2y} \\
W_{\Phi''}^{10}(y) &= (-0.075893 + 0.060682y - 0.0110124y^2) e^{-2y} \\
W_{\Phi''}^{11}(y) &= (0.00940911 - 0.00747826y + 0.00163204y^2) e^{-2y} \\
W_{\Phi'}^{00}(y) &= (0.000495589 - 0.00010394y + 0.00000544981y^2) e^{-2y} \\
W_{\Phi'}^{01}(y) &= (-0.0000552785 - 0.000369894y + 0.0000393968y^2) e^{-2y}
\end{aligned}
$$

$$
\begin{aligned}
W^{10}_{\Phi'}(y) &= (-0.0000552785 - 0.000369894y + 0.0000393968y^2)\mathrm{e}^{-2y} \\
W^{11}_{\Phi'}(y) &= (0.00000616583 + 0.00008381y + 0.0002848y^2)\mathrm{e}^{-2y} \\
W^{00}_{\Delta}(y) &= (0.0335711 - 0.0268568y + 0.00656896y^2)\mathrm{e}^{-2y} \\
W^{01}_{\Delta}(y) &= (0.0161021 - 0.0128817y + 0.00362952y^2)\mathrm{e}^{-2y} \\
W^{10}_{\Delta}(y) &= 0.0161021 - 0.0128817y + 0.00362952y^2)\mathrm{e}^{-2y} \\
W^{11}_{\Delta}(y) &= (0.00772326 - 0.00617861y + 0.0021619y^2)\mathrm{e}^{-2y} \\
W^{00}_{M\Phi''}(y) &= (-5.07498 + 5.86765y - 2.09908y^2 + 0.226345y^3)\mathrm{e}^{-2y} \\
W^{01}_{M\Phi''}(y) &= (0.62922 - 0.727336y + 0.243236y^2 - 0.0210943y^3)\mathrm{e}^{-2y} \\
W^{10}_{M\Phi''}(y) &= (0.220651 - 0.382932y + 0.17682y^2 - 0.0226015y^3)\mathrm{e}^{-2y} \\
W^{11}_{M\Phi''}(y) &= (-0.0273574 + 0.0474719y - 0.0213121y^2 + 0.00280825y^3)\mathrm{e}^{-2y} \\
W^{00}_{\Sigma'\Delta}(y) &= (-0.0291634 + 0.0548817y - 0.0305345y^2 + 0.00476387y^3)\mathrm{e}^{-2y} \\
W^{01}_{\Sigma'\Delta}(y) &= (-0.013988 + 0.0263236y - 0.0171362y^2 + 0.00306717y^3)\mathrm{e}^{-2y} \\
W^{10}_{\Sigma'\Delta}(y) &= (-0.024821 + 0.0482732y - 0.02884y^2 + 0.00481368y^3)\mathrm{e}^{-2y} \\
W^{11}_{\Sigma'\Delta}(y) &= (-0.0119052 + 0.0231539y - 0.0164035y^2 + 0.00310235y^3)\mathrm{e}^{-2y}
\end{aligned} \tag{C.2}
$$

Magnesium (^{24}Mg)

$$
\begin{aligned}
W^{00}_{M}(y) &= (0.123467(9.63385 - 7.49299y + y^2)^2\mathrm{e}^{-2y} \\
W^{00}_{\Phi''}(y) &= 0.0260816(2.5 - y)^2\mathrm{e}^{-2y} \\
W^{00}_{M\Phi''}(y) &= (-1.36673 + 1.6097y - 0.567072y^2 + 0.056747y^3)\mathrm{e}^{-2y}
\end{aligned} \tag{C.3}
$$

Aluminium (^{27}Al)

$$
\begin{aligned}
W^{00}_{M}(y) &= (87.0146 - 146.097y + 83.5367y^2 - 18.5981y^3 + 1.43446y^4)\mathrm{e}^{-2y} \\
W^{01}_{M}(y) &= (-3.22283 + 7.00266y - 4.92756y^2 + 1.33587y^3 - 0.11524y^4)\mathrm{e}^{-2y} \\
W^{10}_{M}(y) &= (-3.22283 + 7.00266y - 4.92756y^2 + 1.33587y^3 - 0.11524y^4)\mathrm{e}^{-2y} \\
W^{11}_{M}(y) &= (0.119366 - 0.31831y + 0.337291y^2 - 0.132526y^3 + 0.018155y^4)\mathrm{e}^{-2y} \\
W^{00}_{\Sigma''}(y) &= (0.0309465 - 0.0367242y + 0.0265347y^2 - 0.00241606y^3 + 0.0110011y^4)\mathrm{e}^{-2y} \\
W^{01}_{\Sigma''}(y) &= (0.0260233 - 0.0210567y + 0.0158643y^2 + 0.000606077y^3 + 0.0105713y^4)\mathrm{e}^{-2y} \\
W^{10}_{\Sigma''}(y) &= (0.0260233 - 0.0210567y + 0.0158643y^2 + 0.000606077y^3 + 0.0105713y^4)\mathrm{e}^{-2y} \\
W^{11}_{\Sigma''}(y) &= (0.0218834 - 0.00944476y + 0.011506y^2 + 0.000953537y^3 + 0.0104813y^4)\mathrm{e}^{-2y} \\
W^{00}_{\Sigma'}(y) &= (0.0618929 - 0.210848y + 0.244466y^2 - 0.0942682y^3 + 0.0243737y^4)\mathrm{e}^{-2y} \\
W^{01}_{\Sigma'}(y) &= (0.0520466 - 0.18713y + 0.233007y^2 - 0.0985082y^3 + 0.0259327y^4)\mathrm{e}^{-2y} \\
W^{10}_{\Sigma'}(y) &= (0.0520466 - 0.18713y + 0.233007y^2 - 0.0985082y^3 + 0.0259327y^4)\mathrm{e}^{-2y} \\
W^{11}_{\Sigma'}(y) &= (0.0437667 - 0.165622y + 0.221193y^2 - 0.101991y^3 + 0.0277477y^4)\mathrm{e}^{-2y} \\
W^{00}_{\Phi''}(y) &= (2.80498 - 2.24306y + 0.455491y^2)\mathrm{e}^{-2y} \\
W^{01}_{\Phi''}(y) &= (-0.180417 + 0.137389y - 0.0239615y^2)\mathrm{e}^{-2y} \\
W^{10}_{\Phi''}(y) &= (-0.180417 + 0.137389y - 0.0239615y^2)\mathrm{e}^{-2y}
\end{aligned}
$$

$$
\begin{aligned}
W^{11}_{\Phi''}(y) &= (0.021493 - 0.0156159y + 0.00596886y^2)\mathrm{e}^{-2y} \\
W^{00}_{\Phi'}(y) &= (0.0000680703 - 0.000376682y + 0.00340251y^2)\mathrm{e}^{-2y} \\
W^{01}_{\Phi'}(y) &= (-0.0010092 + 0.00298228y + 0.00281525y^2)\mathrm{e}^{-2y} \\
W^{10}_{\Phi'}(y) &= (-0.0010092 + 0.00298228y + 0.00281525y^2)\mathrm{e}^{-2y} \\
W^{11}_{\Phi'}(y) &= (0.0149622 - 0.00563307y + 0.00440385y^2)\mathrm{e}^{-2y} \\
W^{11}_{\Phi'}(y) &= (0.021493 - 0.0156159y + 0.00596886y^2)\mathrm{e}^{-2y} \\
W^{00}_{\Delta}(y) &= (0.126043 - 0.100835y + 0.0237577y^2)\mathrm{e}^{-2y} \\
W^{01}_{\Delta}(y) &= (0.0850285 - 0.0680228y + 0.016845y^2)\mathrm{e}^{-2y} \\
W^{10}_{\Delta}(y) &= (0.0850285 - 0.0680228y + 0.016845y^2)\mathrm{e}^{-2y} \\
W^{11}_{\Delta}(y) &= (0.05736 - 0.045888y + 0.012102y^2)\mathrm{e}^{-2y} \\
W^{00}_{M\Phi''}(y) &= (-15.6228 + 19.3589y - 7.23234y^2 + 0.79705y^3)\mathrm{e}^{-2y} \\
W^{01}_{M\Phi''}(y) &= (1.00112 - 1.15934y + 0.40275y^2 - 0.0364952y^3)\mathrm{e}^{-2y} \\
W^{10}_{M\Phi''}(y) &= (0.578632 - 1.00438y + 0.491252y^2 - 0.0730693y^3)\mathrm{e}^{-2y} \\
W^{11}_{M\Phi''}(y) &= (-0.0370794 + 0.0852545y - 0.0449284y^2 + 0.00866992y^3)\mathrm{e}^{-2y} \\
W^{00}_{\Sigma'\Delta}(y) &= (-0.0883243 + 0.185775y - 0.104001y^2 + 0.0163635y^3)\mathrm{e}^{-2y} \\
W^{01}_{\Sigma'\Delta}(y) &= (-0.0595834 + 0.125323y - 0.0717204y^2 + 0.011398y^3)\mathrm{e}^{-2y} \\
W^{10}_{\Sigma'\Delta}(y) &= (-0.0742731 + 0.170242y - 0.105744y^2 + 0.0188197y^3)\mathrm{e}^{-2y} \\
W^{11}_{\Sigma'\Delta}(y) &= (-0.0501045 + 0.114845y - 0.0729898y^2 + 0.0131315y^3)\mathrm{e}^{-2y}
\end{aligned} \tag{C.4}
$$

Silicon (^{28}Si)

$$
\begin{aligned}
W^{00}_{M}(y) &= 0.281695(7.44089 - 6.37784y + y^2)^2\mathrm{e}^{-2y} \\
W^{00}_{\Phi''}(y) &= 0.0739103(2.5 - y)^2\mathrm{e}^{-2y} \\
W^{00}_{M\Phi''}(y) &= (-2.68415 + 3.37434y - 1.281y^2 + 0.144292y^3)\mathrm{e}^{-2y}
\end{aligned} \tag{C.5}
$$

Phosphorus (^{31}P)

$$
\begin{aligned}
W^{00}_{M}(y) &= (38.2357 - 69.0704y + 43.4498y^2 - 11.0707y^3 + 0.982271y^4)\mathrm{e}^{-2y} \\
W^{01}_{M}(y) &= (-1.23341 + 2.75859y - 2.2227y^2 + 0.75098y^3 - 0.0864898y^4)\mathrm{e}^{-2y} \\
W^{10}_{M}(y) &= (-1.23341 + 2.75859y - 2.2227y^2 + 0.75098y^3 - 0.0864898y^4)\mathrm{e}^{-2y} \\
W^{11}_{M}(y) &= (0.0397876 - 0.1061y + 0.105547y^2 - 0.0464186y^3 + 0.0076155y^4)\mathrm{e}^{-2y} \\
W^{00}_{\Sigma''}(y) &= (0.00414265 - 0.0032891y + 0.00743249y^2 - 0.00269138y^3 + 0.00277379y^4)\mathrm{e}^{-2y} \\
W^{01}_{\Sigma''}(y) &= (0.00363025 - 0.00197639y + 0.00581303y^2 - 0.00148204y^3 + 0.00215207y^4)\mathrm{e}^{-2y} \\
W^{10}_{\Sigma''}(y) &= (0.00363025 - 0.00197639y + 0.00581303y^2 - 0.00148204y^3 + 0.00215207y^4)\mathrm{e}^{-2y} \\
W^{11}_{\Sigma''}(y) &= (0.00318122 - 0.000938087y + 0.00467858y^2 - 0.000679619y^3 + 0.0016697y^4)\mathrm{e}^{-2y} \\
W^{00}_{\Sigma'}(y) &= (0.0082853 - 0.0298521y + 0.0465999y^2 - 0.0355087y^3 + 0.0117227y^4)\mathrm{e}^{-2y} \\
W^{01}_{\Sigma'}(y) &= (0.0072605 - 0.0270656y + 0.0425594y^2 - 0.0323588y^3 + 0.0103814y^4)\mathrm{e}^{-2y} \\
W^{10}_{\Sigma'}(y) &= (0.0072605 - 0.0270656y + 0.0425594y^2 - 0.0323588y^3 + 0.0103814y^4)\mathrm{e}^{-2y}
\end{aligned}
$$

$$
\begin{aligned}
W^{11}_{\Sigma'}(y) &= (0.00636245 - 0.0245117y + 0.0389045y^2 - 0.0294649y^3 + 0.00919363y^4)\mathrm{e}^{-2y} \\
W^{00}_{\Phi''}(y) &= (1.19696 - 0.957567y + 0.191514y^2)\mathrm{e}^{-2y} \\
W^{01}_{\Phi''}(y) &= (0.0996532 - 0.0797226y + 0.0159445y^2)\mathrm{e}^{-2y} \\
W^{10}_{\Phi''}(y) &= (0.0996532 - 0.0797226y + 0.0159445y^2)\mathrm{e}^{-2y} \\
W^{11}_{\Phi''}(y) &= (0.00829666 - 0.00663733y + 0.00132747y^2)\mathrm{e}^{-2y} \\
W^{00}_{\Delta}(y) &= 0.000365072(2.5 - y)^2\mathrm{e}^{-2y} \\
W^{01}_{\Delta}(y) &= 0.0000992141(2.5 - y)^2\mathrm{e}^{-2y} \\
W^{10}_{\Delta}(y) &= 0.0000992141(2.5 - y)^2\mathrm{e}^{-2y} \\
W^{11}_{\Delta}(y) &= 0.000026963(2.5 - y)^2\mathrm{e}^{-2y} \\
W^{00}_{M\Phi''}(y) &= (-6.7651 + 8.81641y - 3.52846y^2 + 0.433726y^3)\mathrm{e}^{-2y} \\
W^{01}_{M\Phi''}(y) &= (-0.563231 + 0.734013y - 0.293763y^2 + 0.03611y^3)\mathrm{e}^{-2y} \\
W^{10}_{M\Phi''}(y) &= (0.21823 - 0.378265y + 0.211864y^2 - 0.0381899y^3)\mathrm{e}^{-2y} \\
W^{11}_{M\Phi''}(y) &= (0.0181688 - 0.0314925y + 0.0176388y^2 - 0.00317951y^3)\mathrm{e}^{-2y} \\
W^{00}_{\Sigma'\Delta}(y) &= (-0.00434794 + 0.00957203y - 0.00830496y^2 + 0.00206873y^3)\mathrm{e}^{-2y} \\
W^{01}_{\Sigma'\Delta}(y) &= (-0.00118162 + 0.00260135y - 0.002257y^2 + 0.000562209y^3)\mathrm{e}^{-2y} \\
W^{10}_{\Sigma'\Delta}(y) &= (-0.00381015 + 0.00886346y - 0.00751584y^2 + 0.00183203y^3)\mathrm{e}^{-2y} \\
W^{11}_{\Sigma'\Delta}(y) &= (-0.00103547 + 0.00240878y - 0.00204255y^2 + 0.000497883y^3)\mathrm{e}^{-2y}
\end{aligned} \tag{C.6}
$$

Sulfur (^{32}S)

$$
\begin{aligned}
W^{00}_{M}(y) &= 0.580305(5.92494 - 5.43118y + y^2)^2\mathrm{e}^{-2y} \\
W^{00}_{\Phi''}(y) &= 0.0765941(2.5 - y)^2\mathrm{e}^{-2y} \\
W^{00}_{M\Phi''}(y) &= (-3.12284 + 4.11173y - 1.6721y^2 + 0.210827y^3)\mathrm{e}^{-2y}
\end{aligned} \tag{C.7}
$$

Calcium (^{40}Ca)

$$
\begin{aligned}
W^{00}_{M}(y) &= 0.000016743(1378.8 - 1387.54y + 281.953y^2 - y^3)^2\mathrm{e}^{-2y} \\
W^{00}_{\Phi''}(y) &= 0.0000376718(13.117 - 8.74678y + y^2)^2\mathrm{e}^{-2y} \\
W^{00}_{M\Phi''}(y) &= (-0.454214 + 0.759976y - 0.432314y^2 + 0.0971138y^3 - 0.00730079y^4 \\
&\quad + 0.0000251146y^5)\mathrm{e}^{-2y}
\end{aligned} \tag{C.8}
$$

Chromium (^{52}Cr)

$$
\begin{aligned}
W^{00}_{M}(y) &= (53.7944 - 132.417y + 118.148y^2 - 47.0832y^3 + 8.66093y^4 - 0.668565y^5 \\
&\quad + 0.0178903y^6)\mathrm{e}^{-2y} \\
W^{01}_{M}(y) &= (-4.13803 + 13.369y - 14.9627y^2 + 7.37066y^3 - 1.70602y^4 + 0.174317y^5 \\
&\quad - 0.00604326y^6)\mathrm{e}^{-2y}
\end{aligned}
$$

$$
\begin{aligned}
W_M^{10}(y) &= (-4.13803 + 13.369y - 14.9627y^2 + 7.37066y^3 - 1.70602y^4 + 0.174317y^5 \\
&\quad - 0.00604326y^6)\mathrm{e}^{-2y} \\
W_M^{11}(y) &= (0.318309 - 1.27324y + 1.7912y^2 - 1.08692y^3 + 0.312679y^4 - 0.0414801y^5 \\
&\quad + 0.00204138y^6)\mathrm{e}^{-2y} \\
W_{\Phi''}^{00}(y) &= (2.80823 - 4.49316y + 2.44718y^2 - 0.519936y^3 + 0.0376034y^4)\mathrm{e}^{-2y} \\
W_{\Phi''}^{01}(y) &= (-0.932576 + 1.49212y - 0.813183y^2 + 0.173068y^3 - 0.012546y^4)\mathrm{e}^{-2y} \\
W_{\Phi''}^{10}(y) &= (-0.932576 + 1.49212y - 0.813183y^2 + 0.173068y^3 - 0.012546y^4)\mathrm{e}^{-2y} \\
W_{\Phi''}^{11}(y) &= (0.309696 - 0.495514y + 0.270215y^2 - 0.0576078y^3 + 0.00418588y^4)\mathrm{e}^{-2y} \\
W_{M\Phi''}^{00}(y) &= (-12.2909 + 24.96y - 17.7122y^2 + 5.32514y^3 - 0.663953y^4 + 0.0259371y^5)\mathrm{e}^{-2y} \\
W_{M\Phi''}^{01}(y) &= ((4.08166 - 8.2889y + 5.88422y^2 - 1.77113y^3 + 0.221244y^4 - 0.0086537y^5)\mathrm{e}^{-2y} \\
W_{M\Phi''}^{10}(y) &= (0.945455 - 2.64727y + 2.39138y^2 - 0.909919y^3 + 0.149586y^4 \\
&\quad - 0.00876145y^5)\mathrm{e}^{-2y} \\
W_{M\Phi''}^{11}(y) &= (-0.313973 + 0.879125y - 0.794315y^2 + 0.302513y^3 - 0.0498139y^4 \\
&\quad + 0.00292318y^5)\mathrm{e}^{-2y}
\end{aligned} \tag{C.9}
$$

Iron (^{56}Fe)

$$
\begin{aligned}
W_M^{00}(y) &= (62.3888 - 160.428y + 152.644y^2 - 67.2779y^3 + 14.478y^4 - 1.43665y^5 \\
&\quad + 0.0525291y^6)\mathrm{e}^{-2y} \\
W_M^{01}(y) &= (-4.45633 + 14.6422y - 18.2579y^2 + 10.8919y^3 - 3.2296y^4 + 0.446836y^5 \\
&\quad - 0.0220016y^6)\mathrm{e}^{-2y} \\
W_M^{10}(y) &= (-4.45633 + 14.6422y - 18.2579y^2 + 10.8919y^3 - 3.2296y^4 + 0.446836y^5 \\
&\quad - 0.0220016y^6)\mathrm{e}^{-2y} \\
W_M^{11}(y) &= (0.318309 - 1.27323y + 1.99188y^2 - 1.54562y^3 + 0.622264y^4 - 0.122277y^5 \\
&\quad + 0.00921525y^6)\mathrm{e}^{-2y} \\
W_{\Phi''}^{00}(y) &= (4.22872 - 6.76595y + 3.79067y^2 - 0.867433y^3 + 0.069506y^4)\mathrm{e}^{-2y} \\
W_{\Phi''}^{01}(y) &= (-0.778655 + 1.24585y - 0.741661y^2 + 0.194658y^3 - 0.0183967y^4)\mathrm{e}^{-2y} \\
W_{\Phi''}^{10}(y) &= (-0.778655 + 1.24585y - 0.741661y^2 + 0.194658y^3 - 0.0183967y^4)\mathrm{e}^{-2y} \\
W_{\Phi''}^{11}(y) &= (0.143378 - 0.229404y + 0.144606y^2 - 0.0422756y^3 + 0.00486921y^4)\mathrm{e}^{-2y} \\
W_{M\Phi''}^{00}(y) &= (-16.2427 + 33.8776y - 25.2342y^2 + 8.30471y^3 - 1.20334y^4 + 0.0604243y^5)\mathrm{e}^{-2y} \\
W_{M\Phi''}^{01}(y) &= (2.99085 - 6.23805y + 4.81422y^2 - 1.74483y^3 + 0.288128y^4 - 0.015993y^5)\mathrm{e}^{-2y} \\
W_{M\Phi''}^{10}(y) &= (1.16019 - 3.24853y + 3.31473y^2 - 1.54264y^3 + 0.325832y^4 - 0.0253084y^5)\mathrm{e}^{-2y} \\
W_{M\Phi''}^{11}(y) &= (-0.213631 + 0.598168y - 0.622338y^2 + 0.308014y^3 - 0.0735211y^4 \\
&\quad + 0.00669858y^5)\mathrm{e}^{-2y}
\end{aligned} \tag{C.10}
$$

Nickel (^{58}Ni)

$$
\begin{aligned}
W_M^{00}(y) &= (66.9246 - 175.389y + 169.877y^2 - 76.127y^3 + 16.6597y^4 - 1.6839y^5 \\
&\quad + 0.0628067y^6)\mathrm{e}^{-2y} \\
W_M^{01}(y) &= (-2.30773 + 7.63937y - 10.3404y^2 + 6.95311y^3 - 2.30652y^4 + 0.350525y^5 \\
&\quad - 0.0185041y^6)\mathrm{e}^{-2y} \\
W_M^{10}(y) &= (-2.30773 + 7.63937y - 10.3404y^2 + 6.95311y^3 - 2.30652y^4 + 0.350525y^5 \\
&\quad - 0.0185041y^6)\mathrm{e}^{-2y} \\
W_M^{11}(y) &= (0.0795762 - 0.318305y + 0.548985y^2 - 0.503018y^3 + 0.250492y^4 - 0.0603789y^5 \\
&\quad + 0.00545169y^6)\mathrm{e}^{-2y} \\
W_{\Phi''}^{00}(y) &= (5.4697 - 8.75152y + 4.88454y^2 - 1.10715y^3 + 0.0875404y^4)\mathrm{e}^{-2y} \\
W_{\Phi''}^{01}(y) &= (-0.231284 + 0.370054y - 0.264922y^2 + 0.0935201y^3 - 0.0110873y^4)\mathrm{e}^{-2y} \\
W_{\Phi''}^{10}(y) &= (-0.231284 + 0.370054y - 0.264922y^2 + 0.0935201y^3 - 0.0110873y^4)\mathrm{e}^{-2y} \\
W_{\Phi''}^{11}(y) &= (0.00977975 - 0.0156476y + 0.0136707y^2 - 0.00592935y^3 + 0.00140426y^4)\mathrm{e}^{-2y} \\
W_{M\Phi''}^{00}(y) &= (-19.1326 + 40.3764y - 30.3339y^2 + 10.0435y^3 - 1.4629y^4 + 0.0741493y^5)\mathrm{e}^{-2y} \\
W_{M\Phi''}^{01}(y) &= (0.809015 - 1.7073y + 1.48687y^2 - 0.692274y^3 + 0.145722y^4 - 0.00939131y^5)\mathrm{e}^{-2y} \\
W_{M\Phi''}^{10}(y) &= (0.659741 - 1.84727y + 2.0953y^2 - 1.10461y^3 + 0.25912y^4 - 0.0218459y^5)\mathrm{e}^{-2y} \\
W_{M\Phi''}^{11}(y) &= (-0.0278969 + 0.0781112y - 0.0956406y^2 + 0.0607914y^3 - 0.0211633y^4 \\
&\quad + 0.00276687y^5)\mathrm{e}^{-2y}
\end{aligned}
\tag{C.11}
$$

D Additional figures to section 6.2 under the assumption of interference

Additional figures to section 6.2 are presented here concerning the impact of the annihilation cross section on the coupling strengths under the assumption of interference. The upper limits on the coupling strengths $c_i^\tau,\ i = 1, 3, ..., 15$ under the assumption of isoscalar-isovector interference for different annihilation cross sections are shown in figures D.1, D.2, D.3 and D.4. For the assumption of interference between all interactions the constraints on the coupling strengths $c_i^\tau,\ i = 1, 3, ..., 15$ for different annihilation cross sections are shown in figures D.5, D.6, D.7 and D.8.

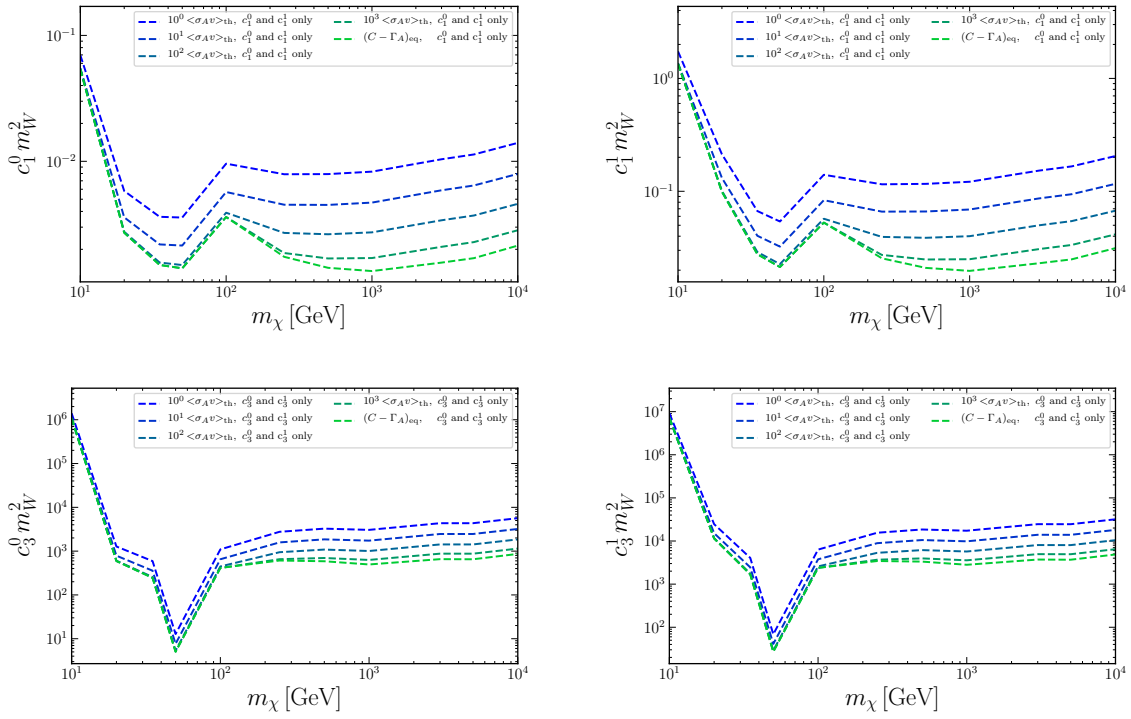

Figure D.1 Upper limits on the coupling strengths $c_i^\tau,\ i = 1, 3,\ \tau = 0, 1$ under the assumption of isoscalar-isovector interference for increasing values of the annihilation cross-section, given as multiples of the thermal relic annihilation cross section $< \sigma_A v >_{\rm th} = 3 \cdot 10^{-26} {\rm cm}^3 {\rm s}^{-1}$ in blue, up to the point, where the upper limits reach the values in case of DM capture - DM annihilation equilibrium $(C - \Gamma_A)_{\rm eq}$, in green. The isoscalar strenghts c_i^0 are on the left side and the isovector strengths c_i^1 on the right sight for each interaction $i = 1, 3$.

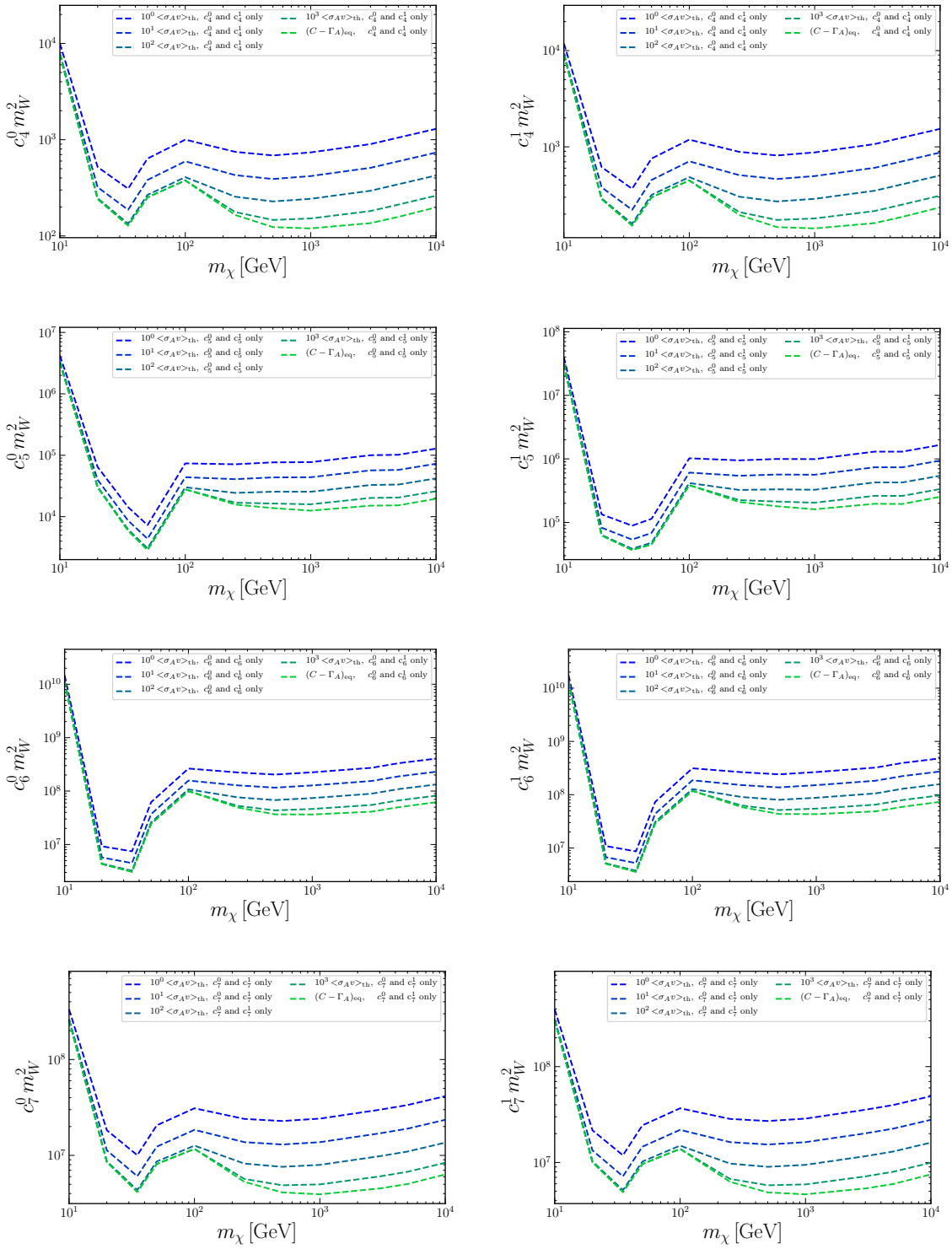

Figure D.2 Same as figure D.1 for coupling strengths c_i^τ, $i = 4, ..., 7$.

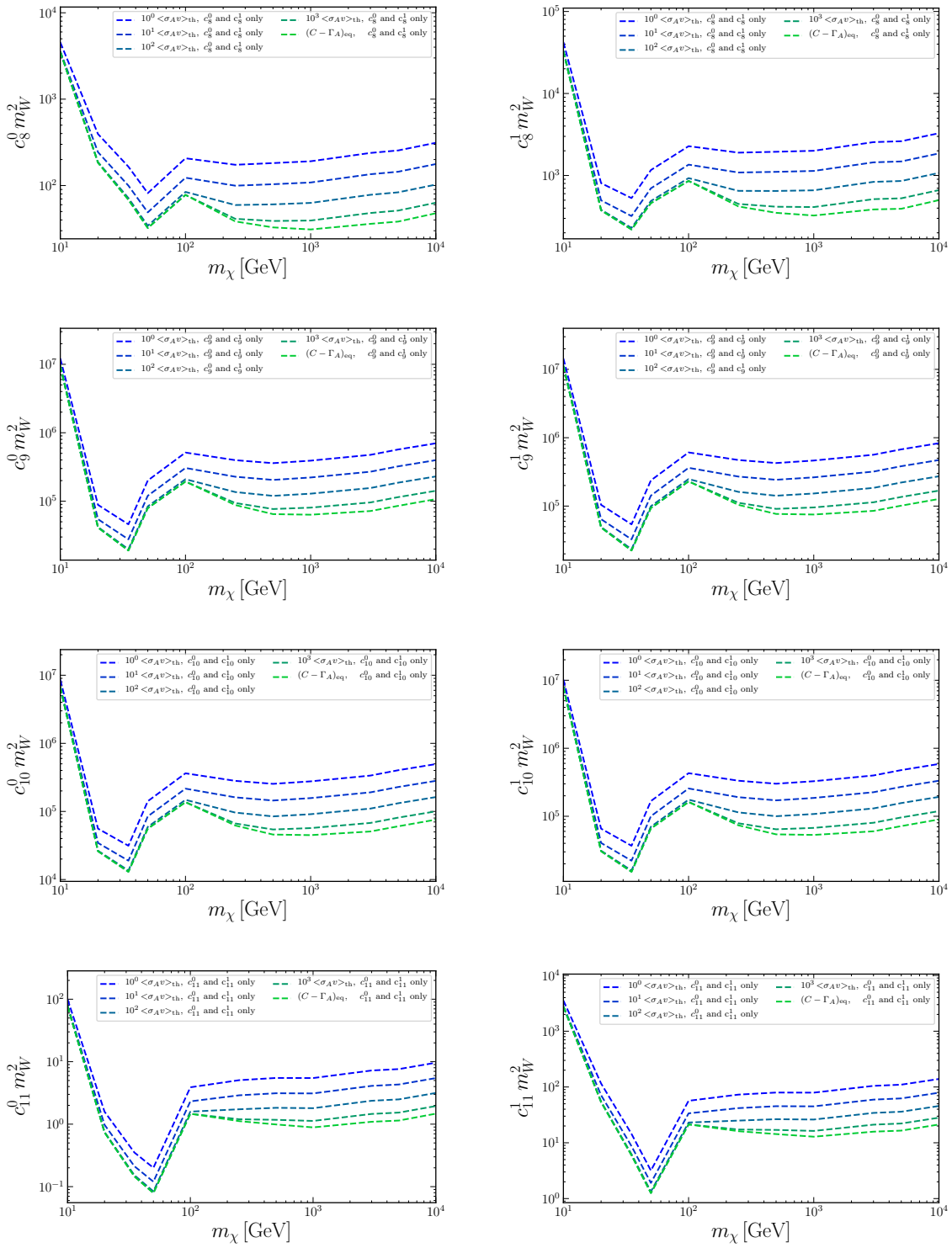

Figure D.3 Same as figure D.1 for coupling strengths c_i^τ, $i = 8, ..., 11$.

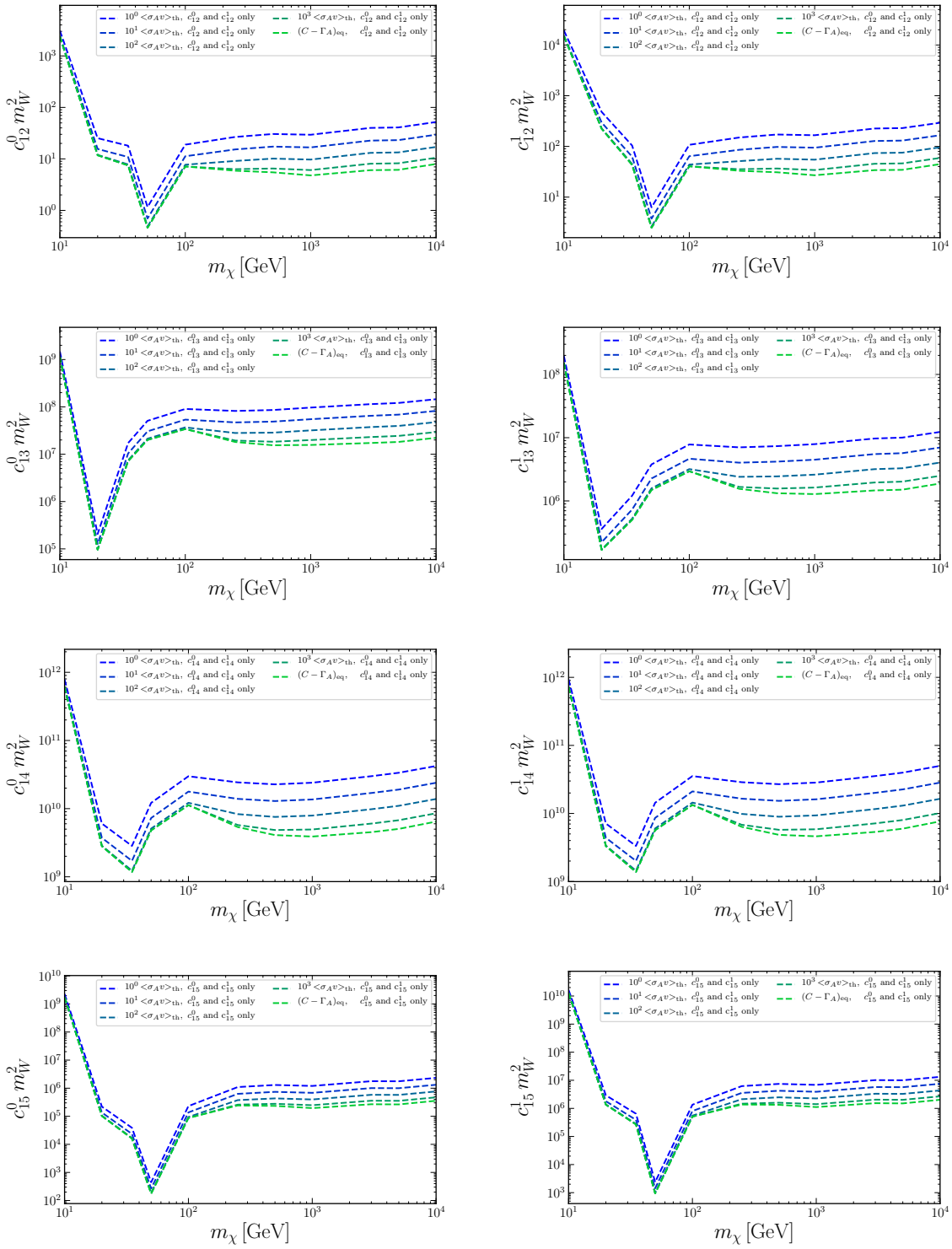

Figure D.4 Same as figure D.1 for coupling strengths c_i^τ, $i = 12, ..., 15$.

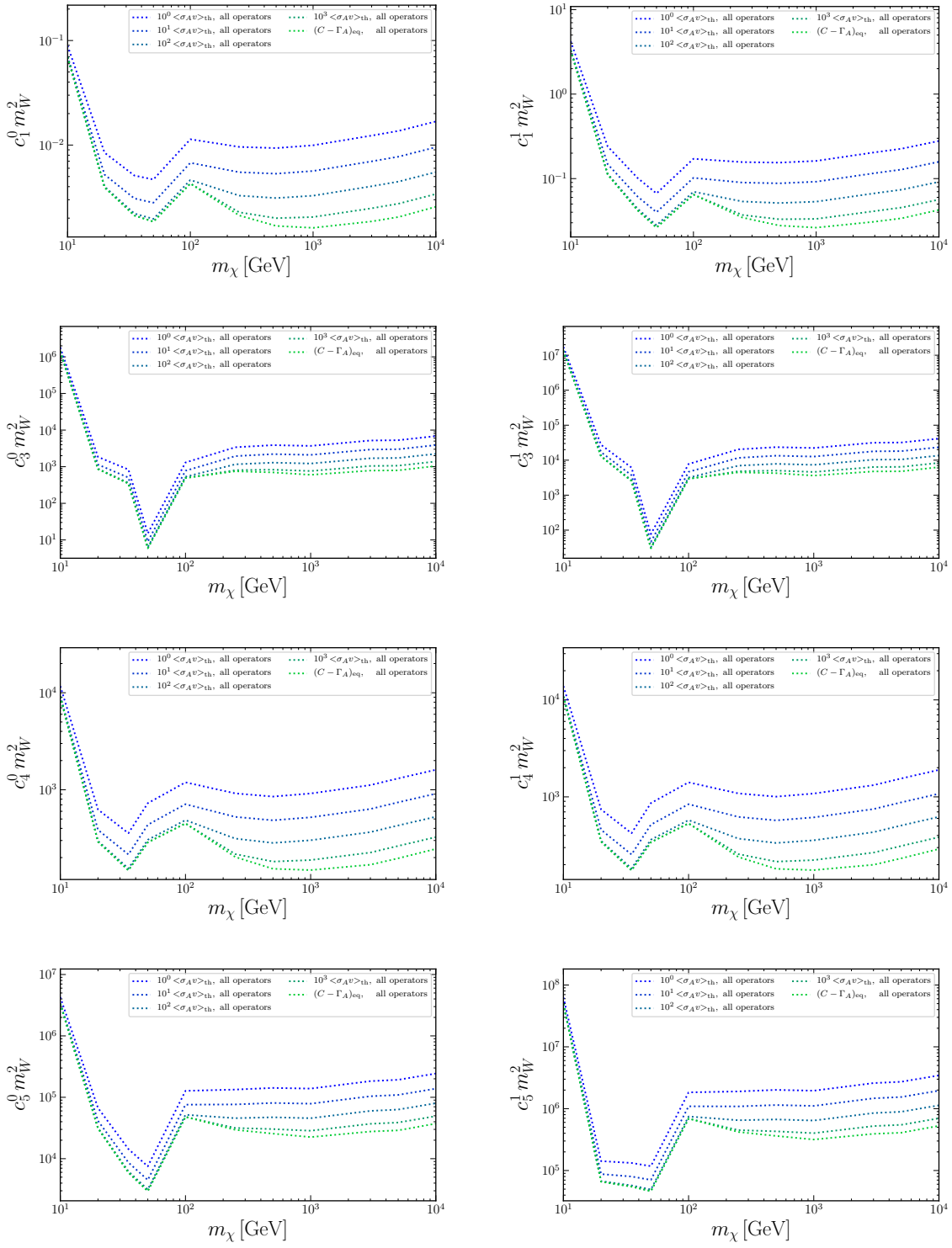

Figure D.5 Upper limits on the coupling strengths $c_i^\tau,\ i = 1, 3, 4, 5,\ \tau = 0, 1$ under the assumption of interference between all interactions for increasing values of the annihilation cross-section, given as multiples of the thermal relic annihilation cross section $< \sigma_A v >_{\rm th} = 3 \cdot 10^{-26} {\rm cm}^3 {\rm s}^{-1}$ in blue, up to the point, where the upper limits reach the value in case of DM capture - DM annihilation equilibrium $(C - \Gamma_A)eq$, in green. The isoscalar strengths c_i^0 are on the left side and the isovector strengths c_i^1 on the right sight for each interaction $i = 1, 3, 4, 5$.

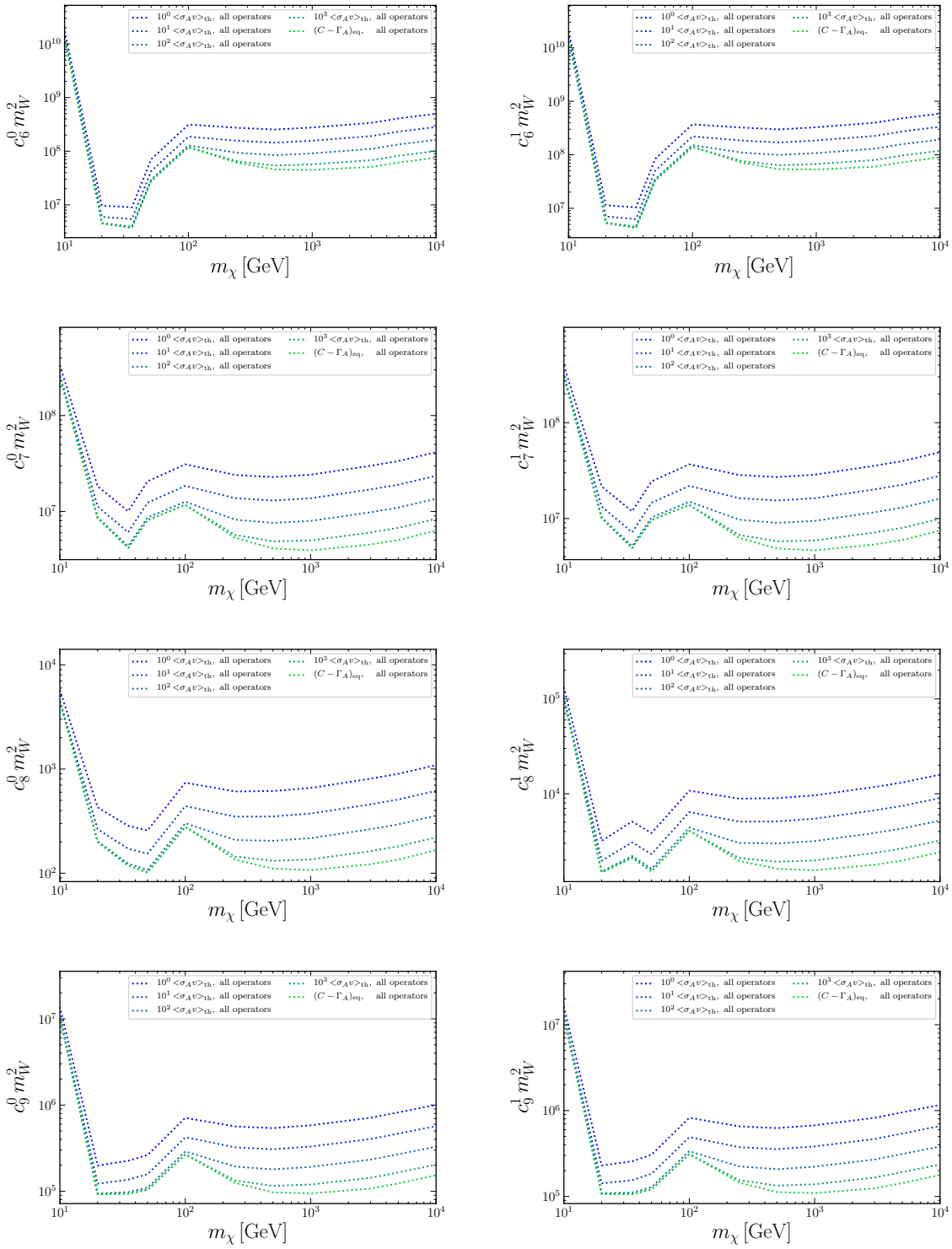

Figure D.6 Same as figure D.5 for coupling strengths $c_i^\tau,\ i = 6, ..., 9$.

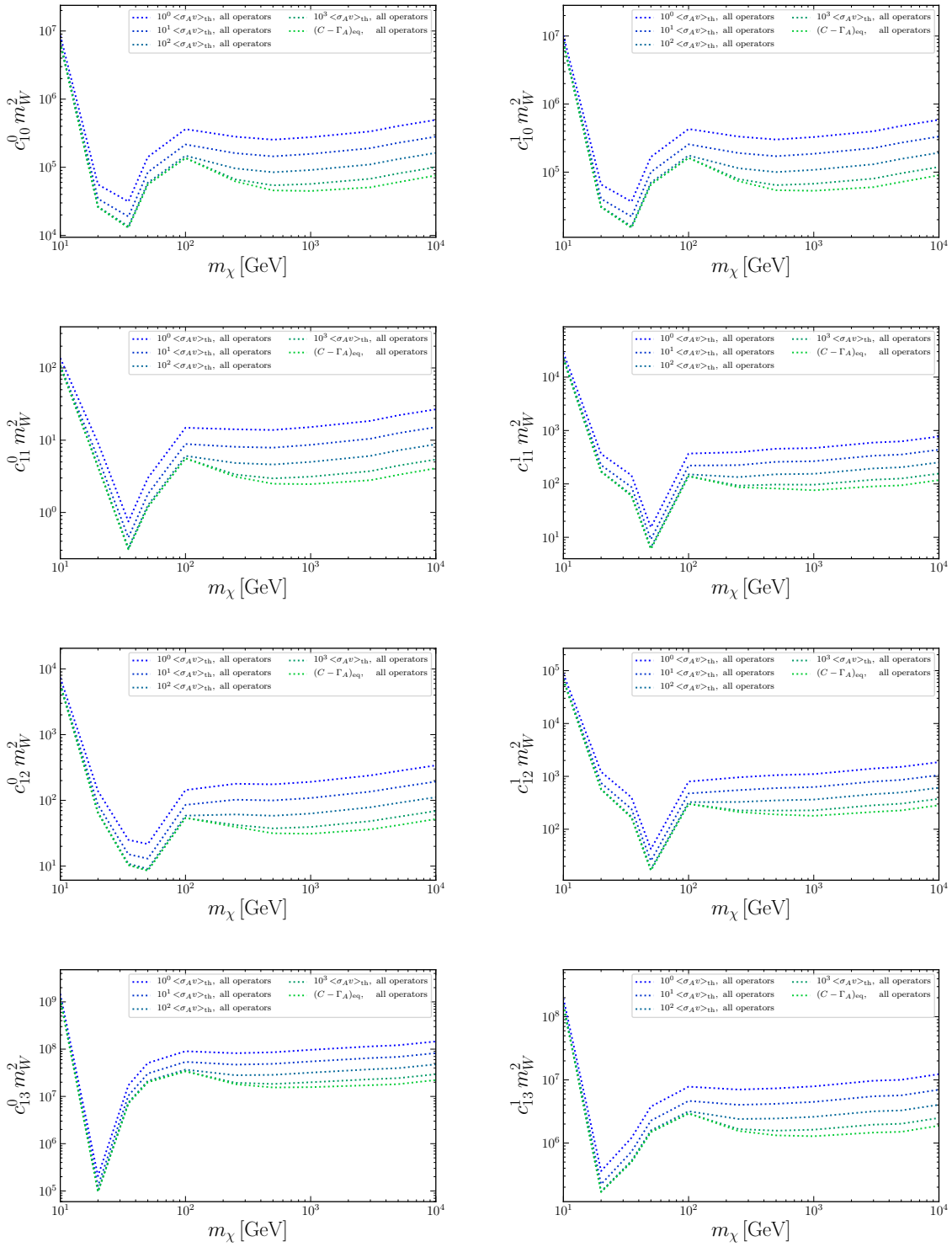

Figure D.7 Same as figure D.5 for coupling strengths c_i^τ, $i = 10, ..., 13$.

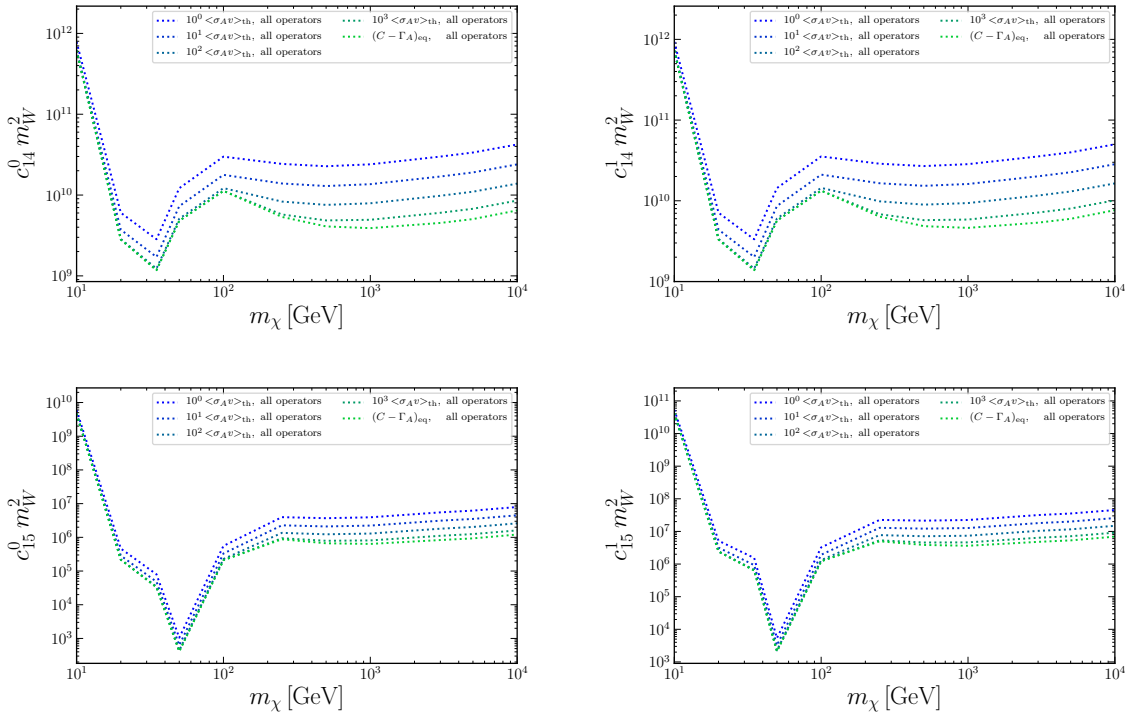

Figure D.8 Same as figure D.5 for coupling strengths $c_i^\tau,\ i = 14, 15$.

E Additional figures to section 6.3 for different annihilation cross sections under the assumption of interference

Additional figures to the comparison of the upper limits on the coupling strengths from IC Earth for different annihilation cross sections with the upper limits from other experiments of chapter 6.3 are presented here under the assumption of interference. The upper limits on the coupling strengths $c_i^\tau,\ i = 1, 3, ..., 15,\ \tau = 0, 1$ from IC Earth at the 90 % confidence level assuming isoscalar - isovector interference for increasing values of the annihilation cross-section, starting at the thermal relic annihilation cross section $< \sigma_A v >_{\text{th}} = 3 \cdot 10^{-26} \text{cm}^3\text{s}^{-1}$ in blue, up to the point, where DM capture - DM annihilation equilibrium $(C - \Gamma_A)_{\text{eq}}$ is attained, in green, are compared to the upper limits from the other experiments in figures E.1, E.2, E.3 and E.4, where XENON1T is depicted in brown, PICO-60 in magenta and IC Sun in yellow. For the assumption of interference between all interactions the constraints on the coupling strengths for different annihilation cross sections in comparison to the other experiments are shown in figures E.5, E.6, E.7 and E.8. As seen in figure E.5 the upper limits on c_1^0 under interference between all operators from IC Earth assuming DM capture - DM annihaltion equilibrium are comparable to the upper limits from XENON1T for a DM mass of 10000 GEV.

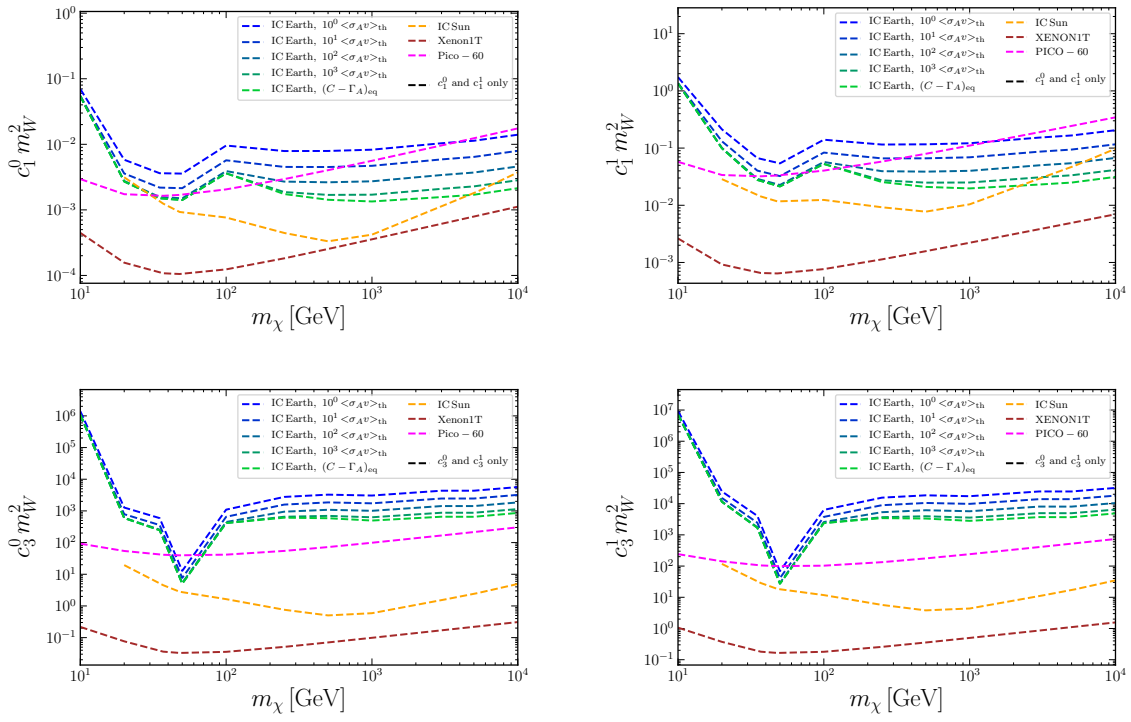

Figure E.1 Upper limits on the coupling strengths $c_i^\tau,\ i = 1, 3,\ \tau = 0, 1$ assuming isoscalar - isovector interference from IC Earth at the 90 % confidence level as function of the DM mass for increasing values of the annihilation cross-section, given as multiples of the thermal relic annihilation cross section $< \sigma_A v >_{\text{th}} = 3 \cdot 10^{-26} \text{cm}^3\text{s}^{-1}$ in blue, up to the point, where DM capture - DM annihilation equilibrium $(C - \Gamma_A)_{\text{eq}}$ is attained, in green, compared to the upper limits from XENON1T in brown, PICO-60 in magenta, and IC Sun in yellow.

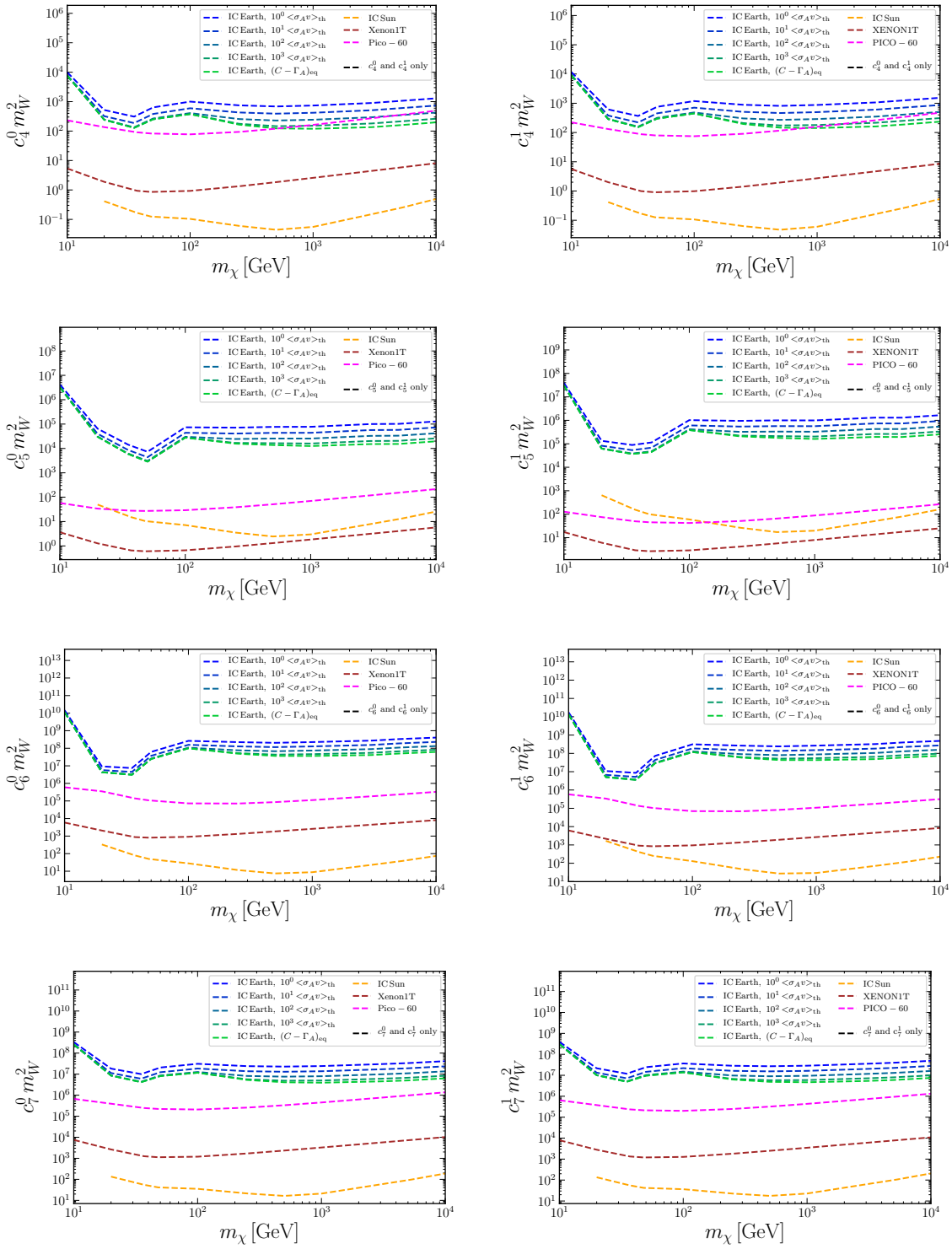

Figure E.2 Same as figure E.1 for coupling strengths $c_i^\tau,\ i = 4, ..., 7$.

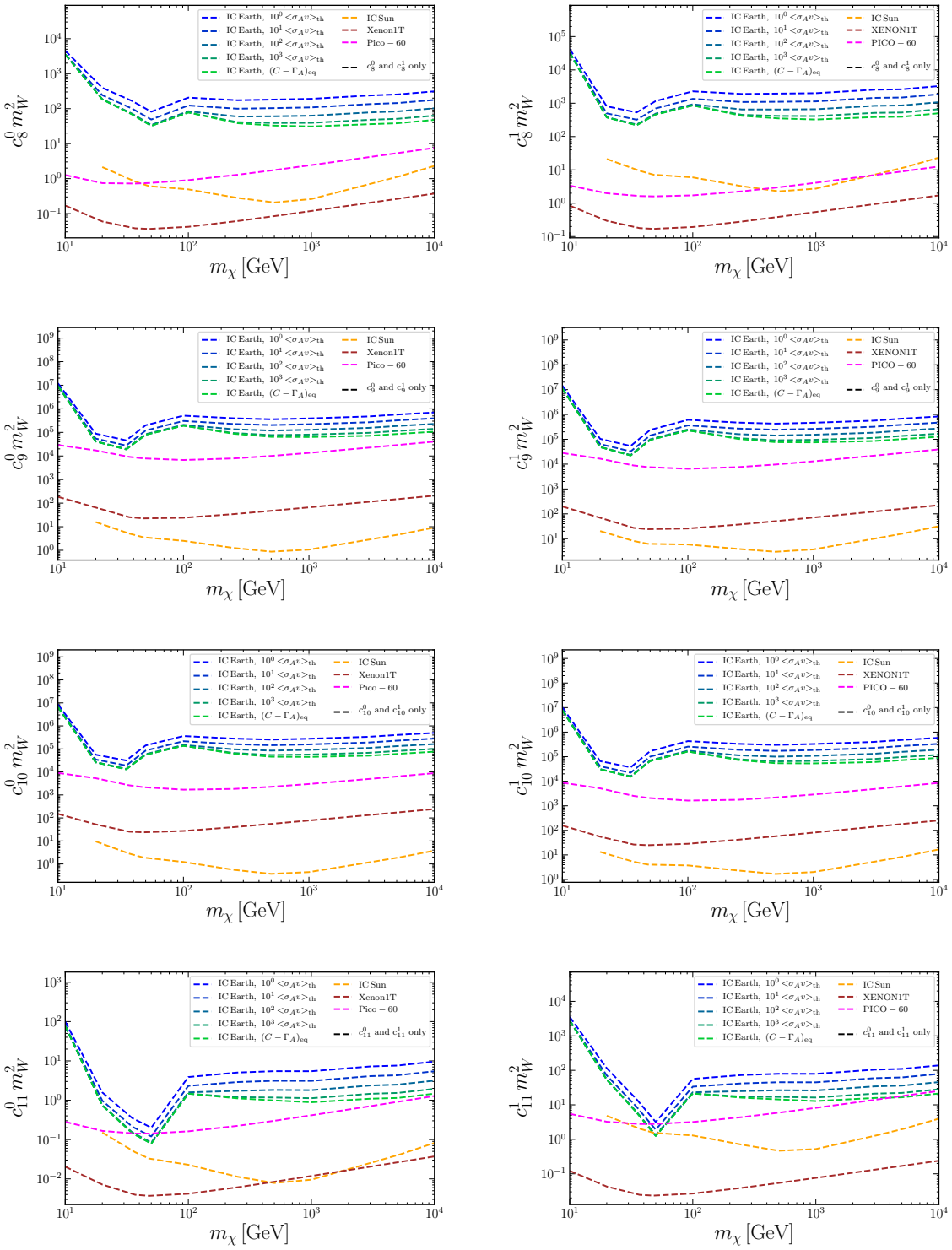

Figure E.3 Same as figure E.1 for coupling strengths $c_i^\tau,\ i = 8, ..., 11$.

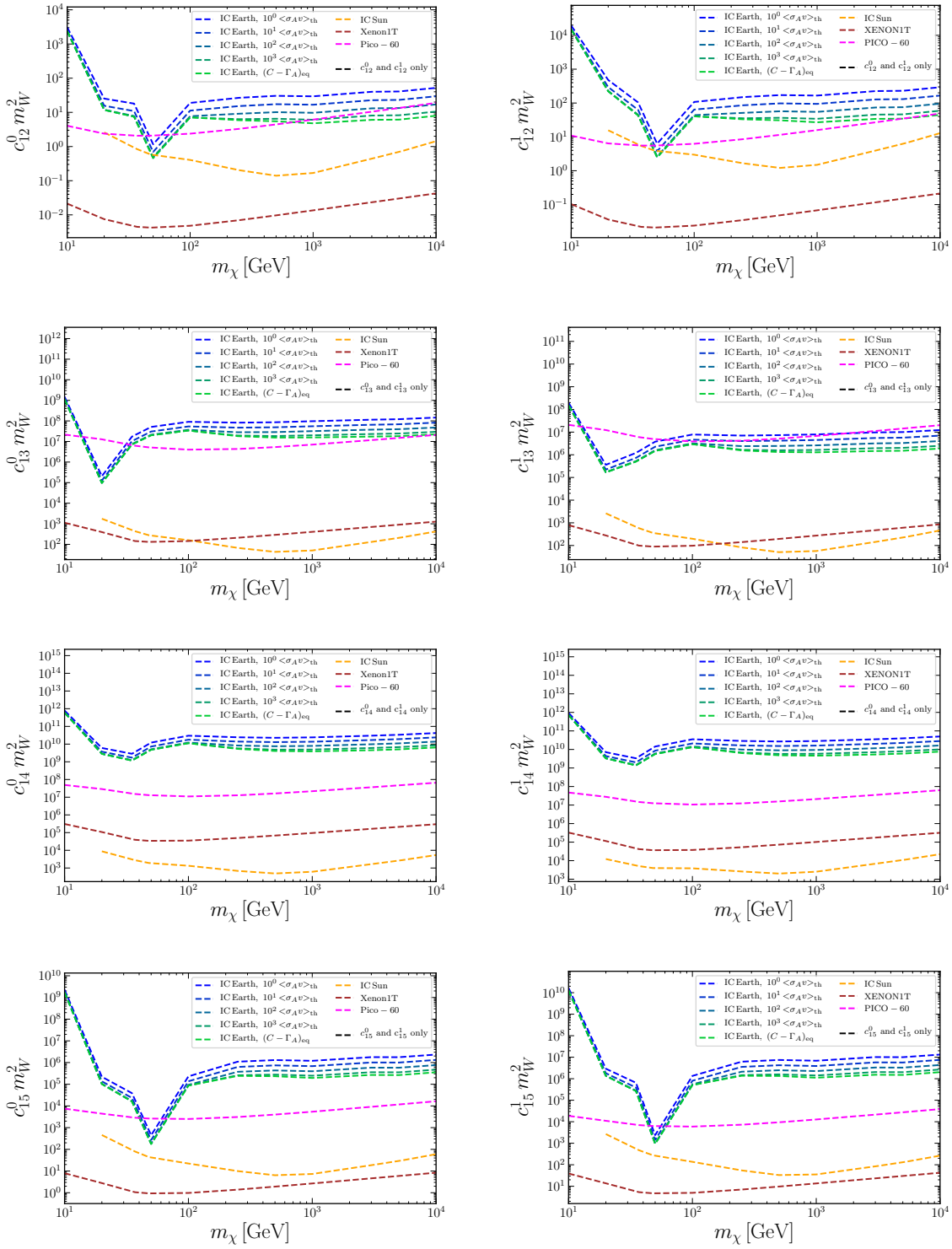

Figure E.4 Same as figure E.1 for coupling strengths c_i^τ, $i = 12, ..., 15$.

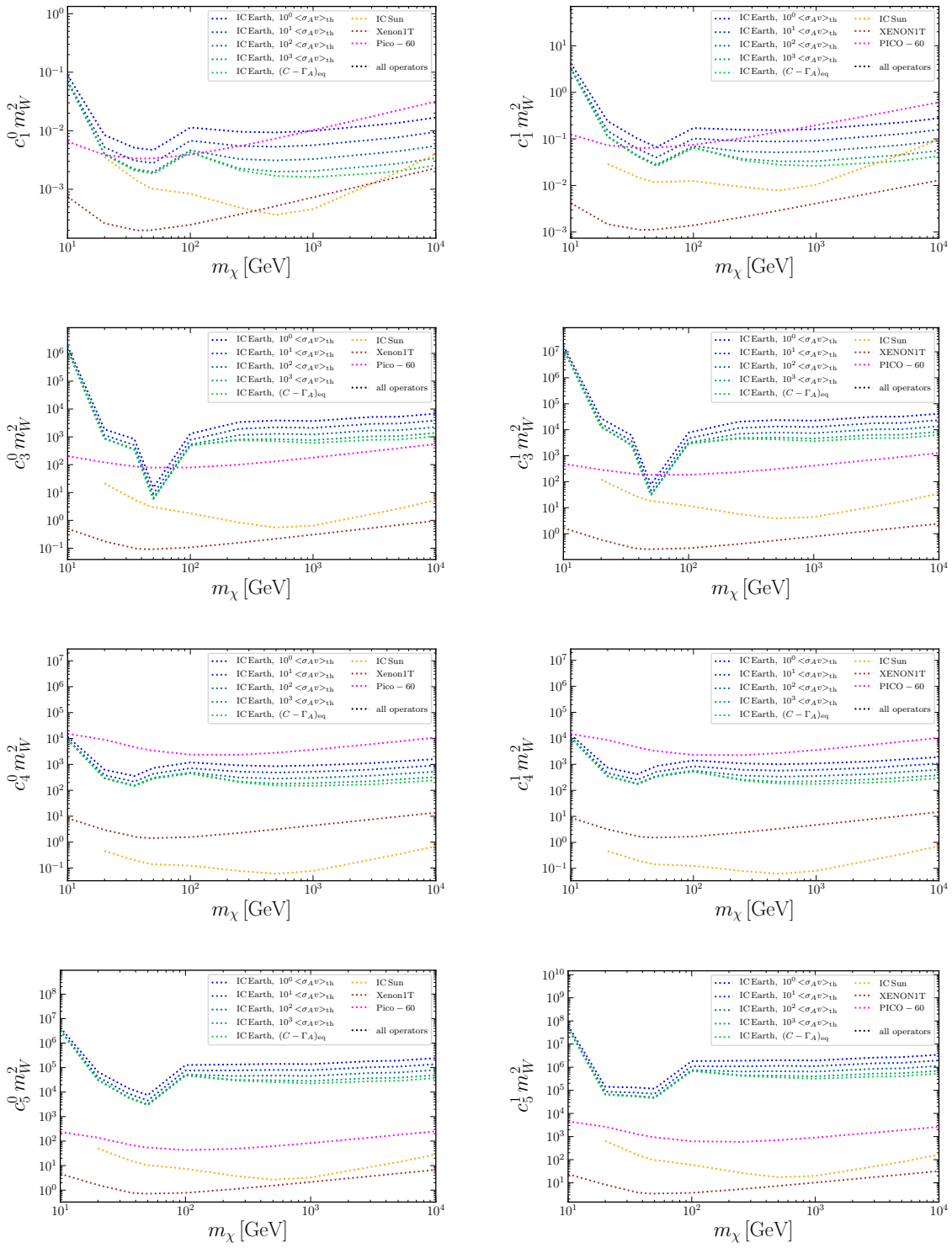

Figure E.5 Upper limits on the coupling strengths c_i^τ, $i = 1, 3, 4, 5$, $\tau = 0, 1$ assuming interference between all operators from IC Earth at the 90 % confidence level as function of the DM mass for increasing values of the annihilation cross-section, given as multiples of the thermal relic annihilation cross section $< \sigma_A v >_{\rm th} = 3 \cdot 10^{-26} {\rm cm}^3 {\rm s}^{-1}$ in blue, up to the point, where the upper limits reach the value in case of DM capture - DM annihilation equilibrium $(C - \Gamma_A)_{\rm eq}$, in green, compared to the upper limts from XENON1T in brown, PICO-60 in magenta, and IC Sun in yellow.

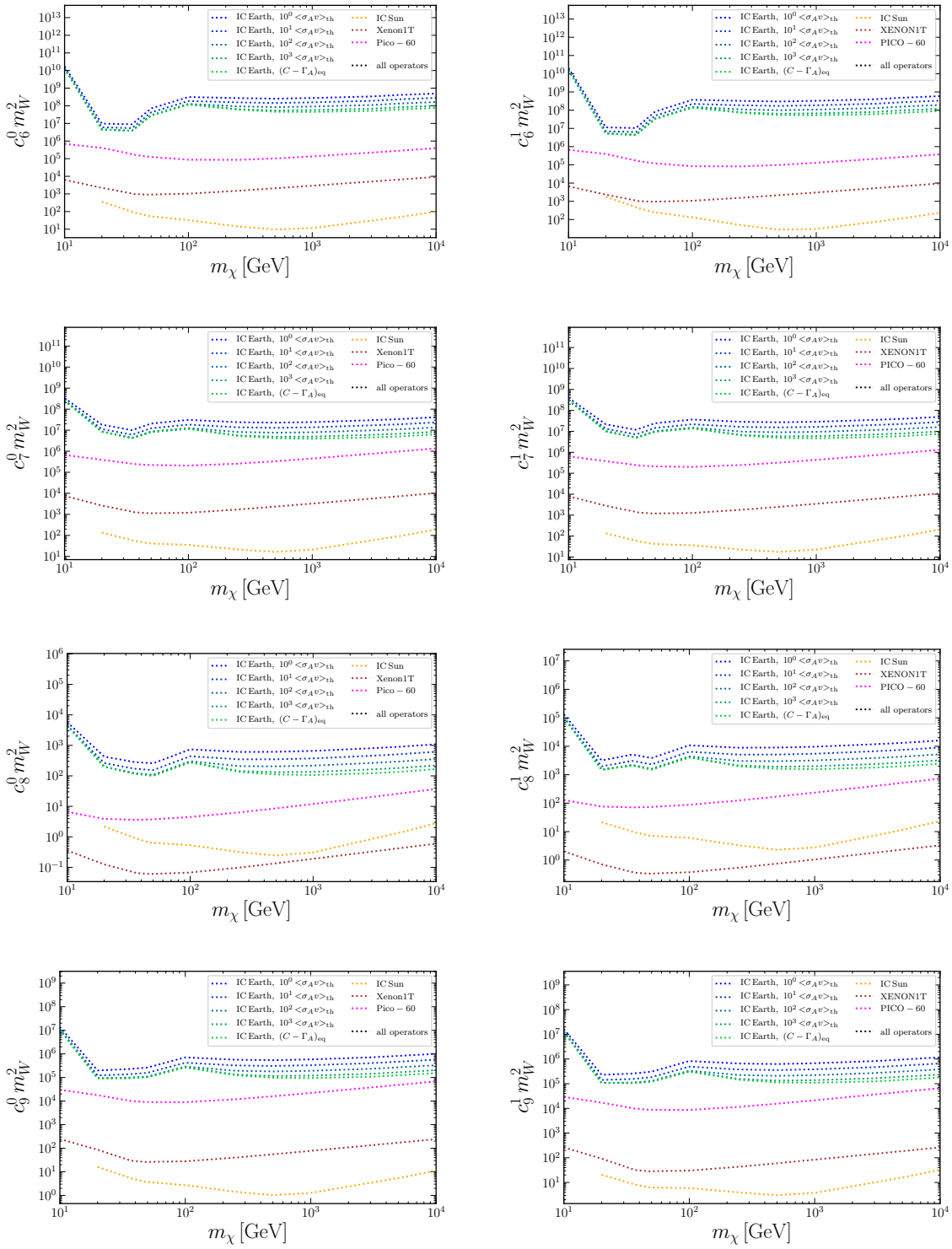

Figure E.6 Same as figure E.5 for coupling strengths $c_i^\tau,\ i = 6, ..., 9$.

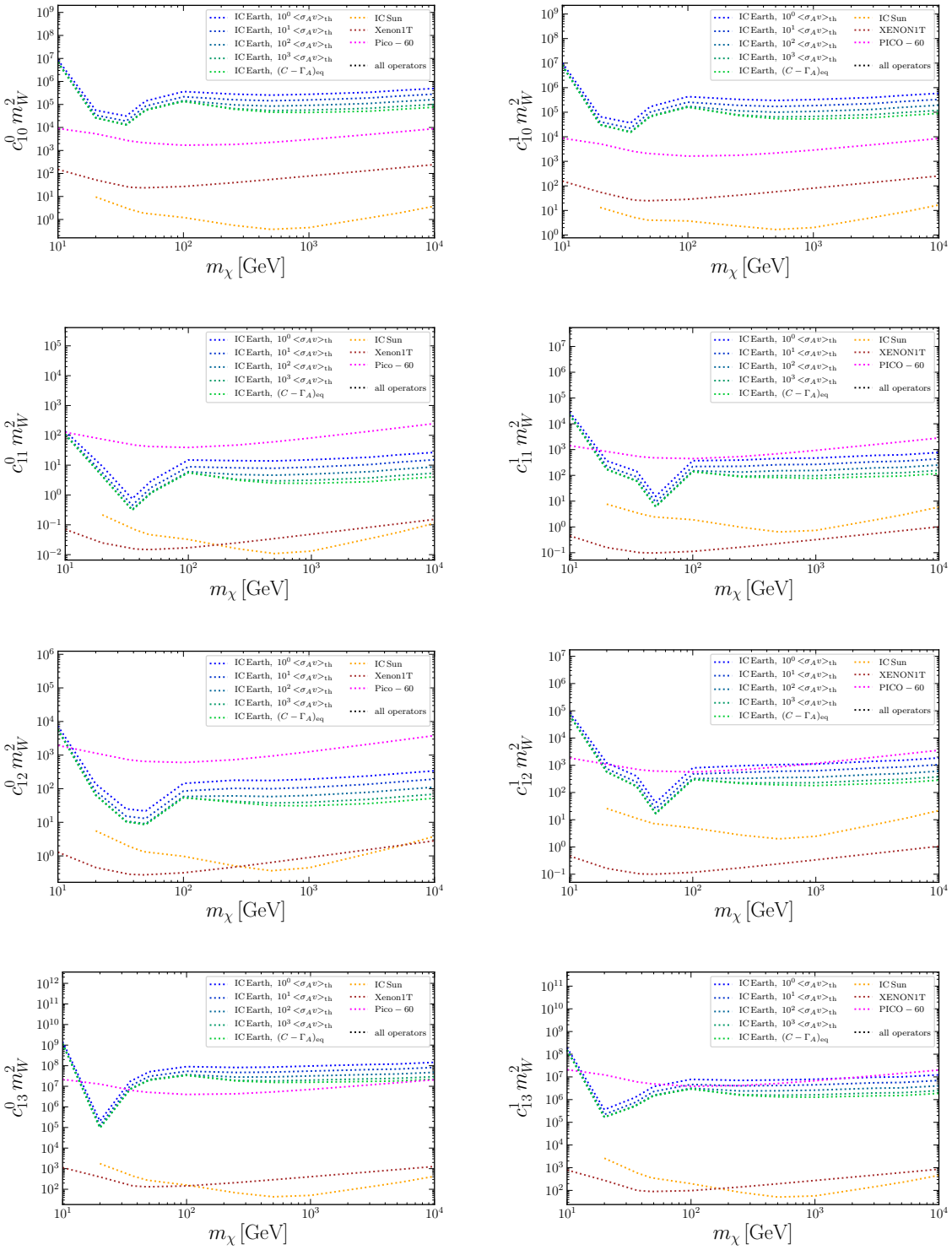

Figure E.7 Same as figure E.5 for coupling strengths $c_i^\tau,\ i = 10, ..., 13$.

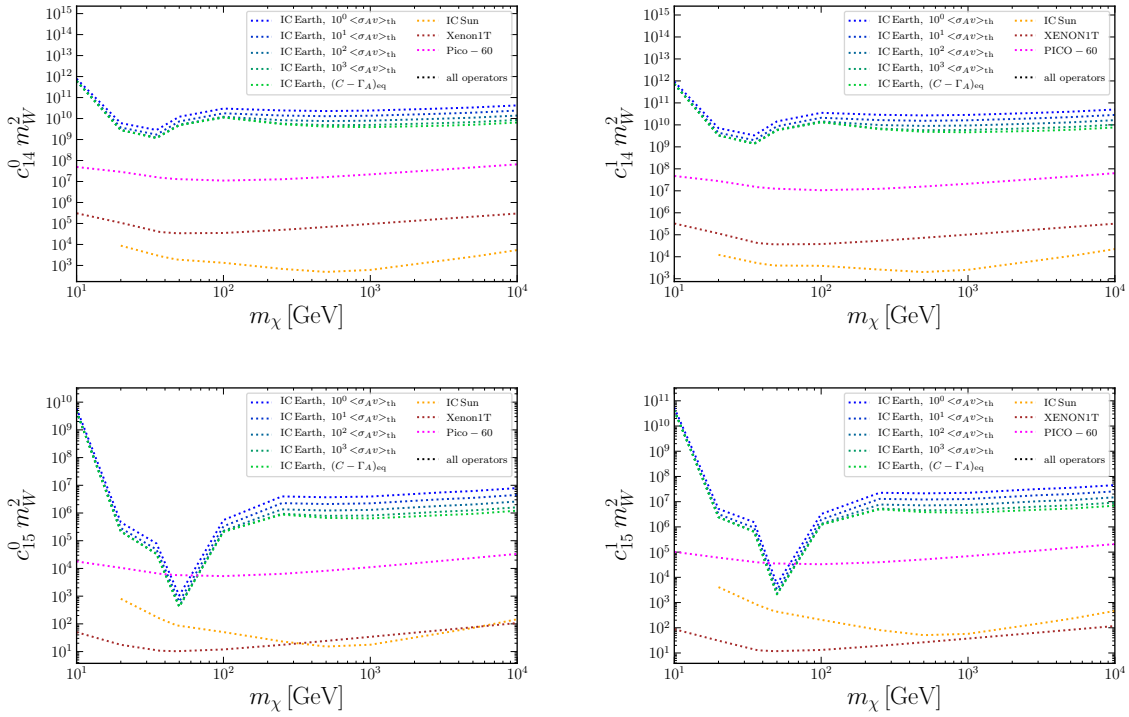

Figure E.8 Same as figure E.5 for coupling strengths $c_i^\tau,\ i = 14, 15$.

Bibliography

[1] F. Zwicky. Die Rotverschiebung von extragalaktischen Nebeln. *Helv. Phys. Acta*, 6:110–127, 1933. doi:10.1007/s10714-008-0707-4.

[2] F. Zwicky. On the Masses of Nebulae and of Clusters of Nebulae. *Astrophys. J.*, 86:217–246, 1937. doi:10.1086/143864.

[3] P. A. R. Ade et al. Planck 2013 results. I. Overview of products and scientific results. *Astron. Astrophys.*, 571:A1, 2014. arXiv:1303.5062.

[4] N. Aghanim et al. Planck 2018 results. V. CMB power spectra and likelihoods. *Astron. Astrophys.*, 641:A5, 2020. arXiv:1907.12875.

[5] Steven W. Allen, August E. Evrard, and Adam B. Mantz. Cosmological Parameters from Observations of Galaxy Clusters. *Ann. Rev. Astron. Astrophys.*, 49:409–470, 2011. arXiv:1103.4829.

[6] Douglas Clowe, Anthony Gonzalez, and Maxim Markevitch. Weak lensing mass reconstruction of the interacting cluster 1E0657-558: Direct evidence for the existence of dark matter. *Astrophys. J.*, 604:596–603, 2004. arXiv:astro-ph/0312273.

[7] Viktor Zacek. Dark Matter. In *22nd Lake Louise Winter Institute: Fundamental Interactions*, pages 170–206, 2007. arXiv:0707.0472.

[8] Gary Steigman, Basudeb Dasgupta, and John F. Beacom. Precise Relic WIMP Abundance and its Impact on Searches for Dark Matter Annihilation. *Phys. Rev. D*, 86:023506, 2012. arXiv:1204.3622.

[9] Gerard Jungman, Marc Kamionkowski, and Kim Griest. Supersymmetric dark matter. *Phys. Rept.*, 267:195–373, 1996. arXiv:hep-ph/9506380.

[10] William H. Press and David N. Spergel. Capture by the sun of a galactic population of weakly interacting massive particles. *Astrophys. J.*, 296:679–684, 1985. doi:10.1086/163485.

[11] Andrew Gould. Resonant Enhancements in WIMP Capture by the Earth. *Astrophys. J.*, 321:571, 1987. doi:10.1086/165653.

[12] Riccardo Catena. WIMP capture and annihilation in the Earth in effective theories. *JCAP*, 01:059, 2017. arXiv:1609.08967.

[13] M. G. Aartsen et al. First search for dark matter annihilations in the Earth with the IceCube Detector. *Eur. Phys. J. C*, 77(2):82, 2017. arXiv:1609.01492.

[14] Gregory D. Mack, John F. Beacom, and Gianfranco Bertone. Towards Closing the Window on Strongly Interacting Dark Matter: Far-Reaching Constraints from Earth's Heat Flow. *Phys. Rev. D*, 76:043523, 2007. arXiv:0705.4298.

[15] Anja Brenner, Gonzalo Herrera, Alejandro Ibarra, Sunghyun Kang, Stefano Scopel, and Gaurav Tomar. Complementarity of experiments in probing the non-relativistic effective theory of dark matter-nucleon interactions. *JCAP*, 06(06):026, 2022. arXiv:2203.04210.

[16] Anja Brenner, Alejandro Ibarra, and Andreas Rappelt. Conservative constraints on the effective theory of dark matter-nucleon interactions from IceCube: the impact of operator interference. *JCAP*, 07:012, 2021. arXiv:2011.02929.

[17] J. H. Oort. The force exerted by the stellar system in the direction perpendicular to the galactic plane and some related problems. *Bulletin of the Astronomical Institutes of the Netherlands*, 6:249–287, 1932.

[18] K. C. Freeman. On the disks of spiral and SO Galaxies. *Astrophys. J.*, 160:811, 1970. doi:10.1086/150474.

[19] Vera C. Rubin and W. Kent Ford, Jr. Rotation of the Andromeda Nebula from a Spectroscopic Survey of Emission Regions. *Astrophys. J.*, 159:379–403, 1970. doi:10.1086/150317.

[20] M. S. Roberts and R. N. Whitehurst. The rotation curve and geometry of M31 at large galactocentric distances. *Astrophys. J.*, 201:327–346, 1975. doi:10.1086/153889.

[21] NASA/CXC/M.Weiss. Chandra x-ray observatory: 1e 0657-56. 2006. URL: https://chandra.harvard.edu/photo/2006/1e0657/index.html.

[22] Eric Gawiser and Joseph Silk. The Cosmic microwave background radiation. *Phys. Rept.*, 333:245–267, 2000. arXiv:astro-ph/0002044.

[23] Wayne Hu and Martin J. White. Acoustic signatures in the cosmic microwave background. *Astrophys. J.*, 471:30–51, 1996. arXiv:astro-ph/9602019.

[24] Joel R. Primack and George R. Blumenthal. WHAT IS THE DARK MATTER? IMPLICATIONS FOR GALAXY FORMATION AND PARTICLE PHYSICS. In *3rd Moriond Astrophysics Meeting: Galaxies and the Early Universe*, pages 445–464, 1983.

[25] Volker Springel, Carlos S. Frenk, and Simon D. M. White. The large-scale structure of the Universe. *Nature*, 440:1137, 2006. arXiv:astro-ph/0604561.

[26] Teresa Marrodán Undagoitia and Ludwig Rauch. Dark matter direct-detection experiments. *J. Phys. G*, 43(1):013001, 2016. arXiv:1509.08767.

[27] C. Amole et al. Dark matter search results from the PICO-60 CF_3I bubble chamber. *Phys. Rev. D*, 93(5):052014, 2016. arXiv:1510.07754.

[28] C. Amole et al. Dark Matter Search Results from the Complete Exposure of the PICO-60 C_3F_8 Bubble Chamber. *Phys. Rev. D*, 100(2):022001, 2019. arXiv:1902.04031.

[29] E. Aprile et al. First Dark Matter Search Results from the XENON1T Experiment. *Phys. Rev. Lett.*, 119(18):181301, 2017. arXiv:1705.06655.

[30] D. S. Akerib et al. Calibration, event reconstruction, data analysis, and limit calculation for the LUX dark matter experiment. *Phys. Rev. D*, 97(10):102008, 2018. arXiv:1712.05696.

[31] Xiangyi Cui et al. Dark Matter Results From 54-Ton-Day Exposure of PandaX-II Experiment. *Phys. Rev. Lett.*, 119(18):181302, 2017. arXiv:1708.06917.

[32] J. Schieck et al. Direct Dark Matter Search with the CRESST II Experiment. *PoS*, ICHEP2016:217, 2016. arXiv:1611.02113.

[33] A. Albert et al. Search for Dark Matter Annihilation in the Earth using the ANTARES Neutrino Telescope. *Phys. Dark Univ.*, 16:41–48, 2017. arXiv:1612.06792.

[34] E. Richard et al. Measurements of the atmospheric neutrino flux by Super-Kamiokande: energy spectra, geomagnetic effects, and solar modulation. *Phys. Rev. D*, 94(5):052001, 2016. arXiv:1510.08127.

[35] A. D. Avrorin et al. Dark matter constraints from an observation of dSphs and the LMC with the Baikal NT200. *J. Exp. Theor. Phys.*, 125(1):80–90, 2017. arXiv:1612.03836.

[36] M. G. Aartsen et al. Search for annihilating dark matter in the Sun with 3 years of IceCube data. *Eur. Phys. J. C*, 77(3):146, 2017. [Erratum: Eur.Phys.J.C 79, 214 (2019)]. arXiv:1612.05949.

[37] M. G. Aartsen et al. Search for neutrinos from decaying dark matter with IceCube. *Eur. Phys. J. C*, 78(10):831, 2018. arXiv:1804.03848.

[38] Gordon Kane and Scott Watson. Dark Matter and LHC: What is the Connection? *Mod. Phys. Lett. A*, 23:2103–2123, 2008. arXiv:0807.2244.

[39] Patrick J. Fox, Roni Harnik, Joachim Kopp, and Yuhsin Tsai. LEP Shines Light on Dark Matter. *Phys. Rev. D*, 84:014028, 2011. arXiv:1103.0240.

[40] Andrew Gould. Direct and Indirect Capture of Wimps by the Earth. *Astrophys. J.*, 328:919–939, 1988. doi:10.1086/166347.

[41] Andrew Gould. Gravitational Diffusion of Solar System WIMPs. *Astrophys. J.*, 368:610, February 1991. doi:10.1086/169726.

[42] Johan Lundberg and Joakim Edsjo. WIMP diffusion in the solar system including solar depletion and its effect on earth capture rates. *Phys. Rev. D*, 69:123505, 2004. arXiv:astro-ph/0401113.

[43] Sofia Sivertsson and Joakim Edsjo. WIMP diffusion in the solar system including solar WIMP-nucleon scattering. *Phys. Rev. D*, 85:123514, 2012. arXiv:1201.1895.

[44] A. M. Dziewonski and D. L. Anderson. Preliminary reference earth model. *Phys. Earth Planet. Interiors*, 25:297–356, 1981. doi:10.1016/0031-9201(81)90046-7.

[45] Raghuveer Garani and Sergio Palomares-Ruiz. Evaporation of dark matter from celestial bodies. *JCAP*, 05(05):042, 2022. arXiv:2104.12757.

[46] Gérard Manhes, Claude J. Allègre, Bernard Dupré, and Bruno Hamelin. Lead isotope study of basic-ultrabasic layered complexes: Speculations about the age of the earth and primitive mantle characteristics. *Earth and Planetary Science Letters*, 47(3):370–382, 1980. doi:https://doi.org/10.1016/0012-821X(80)90024-2.

[47] K. Griest and D. Seckel. Cosmic Asymmetry, Neutrinos and the Sun. *Nucl. Phys. B*, 283:681–705, 1987. [Erratum: Nucl.Phys.B 296, 1034–1036 (1988)]. doi:10.1016/0550-3213(87)90293-8.

[48] JiJi Fan, Matthew Reece, and Lian-Tao Wang. Non-relativistic effective theory of dark matter direct detection. *JCAP*, 11:042, 2010. arXiv:1008.1591.

[49] A. Liam Fitzpatrick, Wick Haxton, Emanuel Katz, Nicholas Lubbers, and Yiming Xu. The Effective Field Theory of Dark Matter Direct Detection. *JCAP*, 02:004, 2013. arXiv:1203.3542.

[50] Riccardo Catena, Kåre Fridell, and Martin B. Krauss. Non-relativistic Effective Interactions of Spin 1 Dark Matter. *JHEP*, 08:030, 2019. arXiv:1907.02910.

[51] Paolo Gondolo, Sunghyun Kang, Stefano Scopel, and Gaurav Tomar. Effective theory of nuclear scattering for a WIMP of arbitrary spin. *Phys. Rev. D*, 104(6):063017, 2021. arXiv:2008.05120.

[52] Riccardo Catena and Bodo Schwabe. Form factors for dark matter capture by the Sun in effective theories. *JCAP*, 04:042, 2015. arXiv:1501.03729.

[53] Nikhil Anand, A. Liam Fitzpatrick, and W. C. Haxton. Weakly interacting massive particle-nucleus elastic scattering response. *Phys. Rev. C*, 89(6):065501, 2014. arXiv:1308.6288.

[54] Martin C. Smith et al. The RAVE Survey: Constraining the Local Galactic Escape Speed. *Mon. Not. Roy. Astron. Soc.*, 379:755–772, 2007. arXiv:astro-ph/0611671.

[55] Til Piffl et al. The RAVE survey: the Galactic escape speed and the mass of the Milky Way. *Astron. Astrophys.*, 562:A91, 2014. arXiv:1309.4293.

[56] X. X. Xue et al. The Milky Way's Circular Velocity Curve to 60 kpc and an Estimate of the Dark Matter Halo Mass from Kinematics of ~2400 SDSS Blue Horizontal Branch Stars. *Astrophys. J.*, 684:1143–1158, 2008. arXiv:0801.1232.

[57] Paul J. McMillan and James J. Binney. The uncertainty in Galactic parameters. *Mon. Not. Roy. Astron. Soc.*, 402:934, 2010. arXiv:0907.4685.

[58] J. I. Read. The Local Dark Matter Density. *J. Phys. G*, 41:063101, 2014. arXiv:1404.1938.

[59] Riccardo Catena, Alejandro Ibarra, and Sebastian Wild. DAMA confronts null searches in the effective theory of dark matter-nucleon interactions. *JCAP*, 05:039, 2016. arXiv:1602.04074.

[60] Riccardo Catena, Alejandro Ibarra, Andreas Rappelt, and Sebastian Wild. Halo-independent comparison of direct detection experiments in the effective theory of dark matter-nucleon interactions. *JCAP*, 07:028, 2018. arXiv:1801.08466.

[61] Cherenkov P.A. Visible emission of clean liquids by action of γ radiation. *Doklady Akademii Nauk SSSR*, 2(451), 1934.

[62] R. Abbasi et al. The Design and Performance of IceCube DeepCore. *Astropart. Phys.*, 35:615–624, 2012. arXiv:1109.6096.

[63] R. Abbasi et al. The IceCube Data Acquisition System: Signal Capture, Digitization, and Timestamping. *Nucl. Instrum. Meth. A*, 601:294–316, 2009. arXiv:0810.4930.

[64] A. Achterberg et al. First Year Performance of The IceCube Neutrino Telescope. *Astropart. Phys.*, 26:155–173, 2006. arXiv:astro-ph/0604450.

[65] M. G. Aartsen et al. The IceCube Neutrino Observatory: Instrumentation and Online Systems. *JINST*, 12(03):P03012, 2017. arXiv:1612.05093.

[66] Markus Ahlers and Francis Halzen. Opening a New Window onto the Universe with IceCube. *Prog. Part. Nucl. Phys.*, 102:73–88, 2018. arXiv:1805.11112.

[67] M. G. Aartsen et al. IceCube Search for Dark Matter Annihilation in nearby Galaxies and Galaxy Clusters. *Phys. Rev. D*, 88:122001, 2013. arXiv:1307.3473.

[68] A. Albert et al. Combined search for neutrinos from dark matter self-annihilation in the Galactic Center with ANTARES and IceCube. *Phys. Rev. D*, 102(8):082002, 2020. arXiv:2003.06614.

[69] M. G. Aartsen et al. Multipole analysis of IceCube data to search for dark matter accumulated in the Galactic halo. *Eur. Phys. J. C*, 75(99):20, 2015. arXiv:1406.6868.

[70] Mattias Blennow, Joakim Edsjo, and Tommy Ohlsson. Neutrinos from WIMP annihilations using a full three-flavor Monte Carlo. *JCAP*, 01:021, 2008. arXiv:0709.3898.

[71] R. Agnese et al. Search for Low-Mass Weakly Interacting Massive Particles Using Voltage-Assisted Calorimetric Ionization Detection in the SuperCDMS Experiment. *Phys. Rev. Lett.*, 112(4):041302, 2014. arXiv:1309.3259.

[72] D. S. Akerib et al. First results from the LUX dark matter experiment at the Sanford Underground Research Facility. *Phys. Rev. Lett.*, 112:091303, 2014. arXiv:1310.8214.

[73] S. Desai et al. Search for dark matter WIMPs using upward through-going muons in Super-Kamiokande. *Phys. Rev. D*, 70:083523, 2004. [Erratum: Phys.Rev.D 70, 109901 (2004)]. arXiv:hep-ex/0404025.

[74] M. G. Aartsen et al. Search for dark matter annihilations in the Sun with the 79-string IceCube detector. *Phys. Rev. Lett.*, 110(13):131302, 2013. arXiv:1212.4097.

[75] Marco Cirelli, Nicolao Fornengo, Teresa Montaruli, Igor A. Sokalski, Alessandro Strumia, and Francesco Vissani. Spectra of neutrinos from dark matter annihilations. *Nucl. Phys. B*, 727:99–138, 2005. [Erratum: Nucl.Phys.B 790, 338–344 (2008)]. arXiv:hep-ph/0506298.

[76] M. L. Ahnen et al. Limits to Dark Matter Annihilation Cross-Section from a Combined Analysis of MAGIC and Fermi-LAT Observations of Dwarf Satellite Galaxies. *JCAP*, 02:039, 2016. arXiv:1601.06590.

[77] Hassan Abdalla et al. Combined dark matter searches towards dwarf spheroidal galaxies with Fermi-LAT, HAWC, H.E.S.S., MAGIC, and VERITAS. *PoS*, ICRC2021:528, 2021. arXiv:2108.13646.

[78] M. G. Aartsen et al. Search for Neutrinos from Dark Matter Self-Annihilations in the center of the Milky Way with 3 years of IceCube/DeepCore. *Eur. Phys. J. C*, 77(9):627, 2017. arXiv:1705.08103.

[79] J. I. Read, L. Mayer, A. M. Brooks, F. Governato, and G. Lake. A dark matter disc in three cosmological simulations of Milky Way mass galaxies. *Mon. Not. Roy. Astron. Soc.*, 397:44, 2009. arXiv:0902.0009.

[80] Sofia Sivertsson and Joakim Edsjo. WIMP diffusion in the solar system including solar WIMP-nucleon scattering. *Phys. Rev. D*, 85:123514, 2012. arXiv:1201.1895.

[81] R. Abbasi et al. Search for GeV-scale dark matter annihilation in the Sun with IceCube DeepCore. *Phys. Rev. D*, 105(6):062004, 2022. arXiv:2111.09970.

[82] Giovanni Renzi. Search for dark matter from the center of the earth with 8 years of icecube data. *Conference: 37th International Cosmic Ray Conference*, 2021. arXiv:2107.11244.

[83] Jonathan L. Feng, Jason Kumar, Danny Marfatia, and David Sanford. Isospin-Violating Dark Matter. *Phys. Lett. B*, 703:124–127, 2011. arXiv:1102.4331.

[84] Koichi Hamaguchi, Seng Pei Liew, Takeo Moroi, and Yasuhiro Yamamoto. Isospin-Violating Dark Matter with Colored Mediators. *JHEP*, 05:086, 2014. arXiv:1403.0324.

[85] M. Zeilik and S.Gregory. Introductory astronomy and astrophysics, fourth edition. *Saunder College Publishing*, 1998.

[86] Henry N. Pollack, Suzanne J. Hurter, and Jeffrey R. Johnson. Heat flow from the earth's interior: Analysis of the global data set. *Reviews of Geophysics*, 31(3):267–280, 1993. doi:10.1029/93RG01249.

[87] S. Karato. The dynamic structure of the deep earth. *Princeton University Press*, 2003.

[88] G. R. Beardsmore and J. P. Cull. Crustal heat flow. a guide to measurement and modelling. *Cambridge University Press*, 2001. doi:10.1017/S0016756803348022.

[89] C. Jones et al. P. Olson. Earth's core and lower mantle. *Taylor and Francis*, 2003.

[90] Glenn D. Starkman, Andrew Gould, Rahim Esmailzadeh, and Savas Dimopoulos. Opening the Window on Strongly Interacting Dark Matter. *Phys. Rev. D*, 41:3594, 1990. doi:10.1103/PhysRevD.41.3594.

[91] Richard H. Cyburt, Brian D. Fields, Vasiliki Pavlidou, and Benjamin D. Wandelt. Constraining strong baryon dark matter interactions with primordial nucleosynthesis and cosmic rays. *Phys. Rev. D*, 65:123503, 2002. arXiv:astro-ph/0203240.

[92] Xue-lei Chen, Steen Hannestad, and Robert J. Scherrer. Cosmic microwave background and large scale structure limits on the interaction between dark matter and baryons. *Phys. Rev. D*, 65:123515, 2002. arXiv:astro-ph/0202496.

[93] B. A. Brown and W. D. M. Rae. Nushell@msu. *MSU-NSCL report*, 2007.

[94] B. A. Brown. The nuclear shell model towards the drip lines. *Prog. Part. Nucl. Phys.*, 47:517–599, 2001. doi:10.1016/S0146-6410(01)00159-4.